Fabrication and Characterization of Pulsed Laser Deposition of $La_{1-x}Ca_xMnO_3$ Based Heterostructures

Submitted by

Leung Yau-shing

for the degree of

Master of Philosophy

in Physics

The Hong Kong Polytechnic University

November 1997

Abstract

Excellent quality epitaxial giant magnetoresistive (GMR) perovskite-like manganates oxide of $La_{1-x}Ca_xMnO_3$ (LCMO) thin films have been fabricated by the Pulsed Laser Deposition (PLD) method. The LCMO films have been successfully grown on single crystal (100)$LaAlO_3$ (LAO) substrates and (100)Silicon (Si) substrates through buffers layers of Titanium Nitride (TiN) and Strontium Titanium Oxide, $SrTiO_3$ (STO). It has been found that the structural quality of the LCMO films improves at higher deposition temperatures and with post deposition annealing. The conductivity and the semiconductor-metal transition temperature (T_c), on the other hand, depend on the crystallinity and the oxygen content of the LCMO films. For deposition on (100)LAO single crystal substrates, a low threshold temperature of 650°C for growing epitaxial LCMO films is detected. A magnetoresistance ratio (MR) of -50% at 170K under a B-field of 1.2T is achieved. For LCMO films prepared directly on (100)Si substrates, multi-phase films with T_c less than 77K (liquid nitrogen temperature) are obtained. By introducing buffer layers of TiN and STO, epitaxial LCMO films have been successfully grown on Si substrates. A MR of -50% at 116K under a B-field of 1.2T has been realized in the LCMO/STO/TiN/Si heterostructure.

Acknowledgements

I would like to acknowledge my supervisor, Dr. K.H. Wong, a kind person, for his close supervision and guidance throughout this two years. I am greatly appreciated by his suggestions and assistance in this project. Special thanks should be given to Dr. W.B. Wu for his valuable suggestions and discussions.

I would like also to thanks my research companion, Mr. M.F. Li, for lending help in some experiments and suggestions. Extended thanks should be given to my dearest friends, Miss H.N. Yeung and Mr. L.T. Chen for their mental support in this period of years.

This work is supported by a Research Grant of the Hong Kong Polytechnic University under Code No. 0350.536.A3.110. It is grateful for the award of a research studentship by the Hong Kong Polytechnic University.

Table of Contents

Chapter 4 Experiments and Set-up

Chapter 5 Fabrication and Characterization of LCMO/LAO

Chapter 1

Introduction

In recent years the Pulsed Laser Deposition (PLD) method has been widely used in thin films fabrication. The PLD method has a distinct advantage of "congruent" evaporation of materials from target. The stoichiometry of multi-component materials can be preserved in the deposited films. This is especially useful for the fabrication of ceramic oxides films. Excellent quality epitaxial thin films such as high T_c superconductor $YBa_2Cu_3O_7$ [Joosse, 1994; Zhang,1995; Chrzanowski,1995], ferroelectric perovskite oxides [Ramesh et al., 1990; Horwitz et al., 1991], giant magnetoresistive manganates [Jin, 1994; Gu, 1995; Liu, 1995] and so on have been reported.

The family of perovskite manganates $R_{1-x}A_xMnO_3$ (where R is La, Nd or another rare earth element, and A is Sr, Ba, Ca or another divalent element) have been shown to possess giant magnetoresistance (GMR) properties. The magnetoresistance is the change in electrical resistance of a material in response to a magnetic field. The doping of the divalent elements in manganates produces a mixture of Mn^{3+} and Mn^{4+} ions which improve the conductivity of the oxides. The manganates have antiferromagnetic - ferromagnetic transition and also semiconductor-to-metal transition at Curie temperature (T_c). The occurrence of ferromagnetism and metallic conductivity can be explained by Zener's Double Exchange (DE) mechanism [Zener, 1951]. The external applied magnetic field can lower the resistance of the GMR materials at a wide range of temperatures because the magnetic field reduces the

magnetic disordering and hence the conduction of electrons is enhanced if the surrounding electron spins are aligned ferromagnetically.

Due to the importance and potential application of these GMR materials in magnetic recording and reading heads, considerable effort has been devoted to study their properties. Fabrication and characterization of manganate thin films by various film growth techniques have been actively researched. High quality $La_{1-x}Ca_xMnO_3$ (LCMO) films grown on single crystal substrates such as $LaAlO_3$ (LAO) [Jin, 1994] and MgO [Gu, 1995] by PLD method have been reported recently. For practical electronic device application, it will be very useful if the LCMO films can be prepared on Silicon (Si) wafer. However, LCMO and Si have large lattice mismatch (a=3.89Å for (100)LCMO and a=5.43Å for (100)Si). In addition Si is easily oxidized under ambient oxygen at elevated temperatures. Epitaxial LCMO films grown directly on Si is therefore expected to be very difficult.

In the present study, we aim to investigate the process of PLD of LCMO thin films. Parameters affecting the structural quality and electrical characteristics of the films and other LCMO based heterostructures have been examined carefully. Our main objective is to obtain heteroepitaxially grown LCMO films on Si substrate with good GMR properties.

To circumvent the problem of lattice mismatch and oxidation of Si substrate, a non-oxide buffer layer is introduced. Titanium Nitride (TiN) buffer layer is known to grow epitaxially on Si substrates [Zheleva, 1994; Lee, 1994]. Conductive TiN is a

good interdiffusion barrier too. It has been used previously as the bottom electrode layer for depositing dielectric films [Lee, 1995]. In buffering the LCMO films on Si, however, the TiN layer will effectively become a current shunt. For this reason an insulating Strontium Titanium Oxide [$SrTiO_3$ (STO)] layer is additionally introduced to buffer the TiN. The LCMO layer is then deposited on the STO/TiN/Si heterostructure. Our experimental investigation has led to the success of fabricating a heteroepitaxial LCMO/STO/TiN/Si with excellent GMR properties.

In Chapter 2 a brief history and the mechansims of PLD will be presented. The advantages and limitations of using PLD for film preparation will be discussed. Different modes of film growth will be also mentioned.

In Chapter 3 we will focus on the discussion of the properties and the possible origin of the GMR effect in perovskite-like manganates. Some current results on LCMO and PLD of LCMO films will be reviewed.

Experimental set-up and instrumentation for PLD will be presented in Chapter 4. Working principles for some major characterization equipment such as X-ray Diffractometer (XRD), four-point probe and electromagnet will be described. Procedures for fabrication of ceramic oxides targets and thin films will be given.

In Chapter 5 we will report the results of LCMO films grown on (100)LAO single crystal substrate. The processing parameters as well as the LCMO films' structural, electrical and magnetic properties will be discussed. X-ray diffraction

patterns, resistivity-temperature (R-T) curves and magnetoresistance ratio (MR) profiles will be shown for comparison.

Results of PLD of LCMO/Si, TiN/Si, LCMO/TiN/Si, STO/TiN/Si and LCMO/STO/TiN/Si heterostructures will be presented in Chapter 6. Discussions on the structural quality of the heteroepitaxial films will be given. Finally the magnetoresistance ratio (MR) of the heteroepitaxial LCMO/STO/TiN/Si will be presented.

Chapter 2

Pulsed Laser Deposition (PLD)

2.1 History of Pulsed Laser Deposition

The first laser was demonstrated by T. H. Maiman in 1960 at the Hughes Research Laboratories [Maiman, 1960]. Shortly afterwards, many theoretical and experimental studies on the interactions of intense laser beams with solid surfaces [Ready, 1963], liquids [Askar'yan et al., 1963], and gaseous materials [Meyerand, and Haugth, 1963] were reported. The ease with which material was vaporized suggested that the intense laser radiation could be used to deposit thin films. Indeed the first experiment on pulsed laser deposition (PLD) was performed by Smith and Turner in 1965 [Smith and Turner, 1965]. However, the development of laser deposition was very slow. The laser deposition technique at that time was immature and was not comparable with other concurrent techniques such sputtering to produce high quality thin films. The rapid progress of laser technology and the development of other types of laser such as the CO_2 lasers [Patel et. al., 1964] and the Nd: YAG [Geusic et. al., 1964] has made PLD more competitive. These lasers have a higher repetition rate than the ruby laser, making the growth of thin films possible. In the mid-1970s, the electronic Q-switch was developed for generating very short optical pulses to attain laser peak power exceeding 10^8 W/cm^2. In this very period of time, other significant technical advances were developed such as the high efficiency second harmonic generator to deliver shorter wavelength radiation and the UV excimer

lasers. Thus, the selection of the materials for pulsed laser deposition was much widened and the quality of the thin films was also improved.

Another breakthrough for PLD was the successful fabrication of high T_c superconducting thin films in 1987. In this period, the observation that laser ablation transfers the stoichiometry of a multicomponent system to the film and allows oxygenation and other chemistry to occur in plasma during transit from target to substrate was truly remarkable [Dijkkamp et al., 1987; Wu et al., 1990]. Virtually all materials - metals, semiconductors and insulators can be deposited by laser ablation. The total number of publications in PLD in 1987 alone was more than 10 times the combined publications in the previous 25 years. Since then PLD has been used very successfully to grow high quality thin films of superconductors, ferroelectrics, semiconductors, metal oxides, metallic multilayers and various superlattices.

One of the latest trends in PLD development is the heteroepitaxial growth of oxides on semiconductors such as YSZ/Si [Fork et al., 1990], MgO/GaAs [Chang et al., 1992; Fork et al., 1992; Prusseit et al., 1992]. This area has found success unmatched by any other film growth techniques and opens up possibilities of new devices based on the integration of semiconductors and oxides. The growth of ferroelectric perovskite oxide films is an area showing good potential promises [Ramesh et al., 1990; Horwitz et al., 1991]. The growth of perovskite ferroelectric films is a natural extension of the work on high T_c oxide superconductors because of the structural similarity between these two materials. Epitaxial multilayer structures can be grown by incorporating matching oxide electrodes to improve the performance

endurance of the devices subject to repetitive cycling. Nitrides are another material system that have been successfully grown by PLD. Epitaxial layers of TiN have been grown on (100) Si substrates [Narayan et al., 1992]. Yet, for other nitrides, such as AlN [Norton et al., 1991] and BN [Doll et al., 1991; Friedmann et al., 1992], results were far from satisfactory. PLD has also been applied to deposit diamond-like-carbon films from a graphite target [Rengen and Narayan, 1992]. As a sign of maturity and gaining recognition, production-related issues concerning reproducibility [Cheung et al., 1992] and large-area scale-up [Greer and Van Hook, 1990], have begun to be addressed. It is the dawn of a new age of PLD.

2.2 Advantages and Disadvantages of Pulsed Laser Deposition

There are, at present, many methods for deposition of thin films such as thermal evaporation (TE) [Bunshah, 1982], molecular beam epitaxy (MBE) [Parker, 1986], chemical vapor deposition (CVD) and metal-organic chemical vapor deposition (MOCVD) [Stringfellow, 1988], pulsed laser deposition (PLD), sputtering (S), ion clusters beam deposition (ICBD) [Brown et al., 1991] and so on. In choosing a particular technique for the deposition, two criteria should be considered, namely the fundamental and the practical criteria. The fundamental criterion concerns the physical parameters that can be externally controlled during film deposition; for example, the substrate temperature and the pressure in the chamber. The practical criterion deals with, for examples, the area of coverage of deposition, deposition efficiency and cost. Often a technique that fulfills the fundamental criterion might not be practically useful because it is very costly.

The technique of PLD offers many unique advantages. First of all, the "congruent" evaporation of multi-component targets in PLD leads to little difference in stochimetry between the target and the deposited films. This feature of PLD allows the selection of virtually any materials for the deposition. For example, thin films of ceramic oxides which are multi-component materials, can be grown easily by PLD. Another advantage of the PLD is the simplicity of the experimental set-up. The size of the target is very small and the vacuum condition requirement is less stringent than many other sputtering method.

There are, of course, disadvantages in using PLD method to deposite thin films. The non-uniformity of the film's thickness remains an acute problem. The film thickness is highest at the center of the plasma plume normal to the target surface and decreases rapidly with the distance away from this point [Venkatesan, 1988]. This limitation will restricts the fabrication of uniform thin films of large area. There are however, some methods to improve the thin films' uniformity. For example, by tilting and rotating the target result in a much larger scanning area of the plasma plume to the substrates and hence can much improve the uniformity of the thin films to form larger area size samples [Greer, 1989; Buhay et al.,1992]. The other intrinsic disadvantage of the PLD method is the formation of particulates. The size of particulates can be as large as a few of microns. This problem is more severe in the multi-layer systems because the particulates on the surface of the films will greatly affect the growth of the subsequent layers and the interface quality. The insertion of an opaque mask between the target and the substrate forming a shadow mask to block the large particulates emitted from the target in the forward direction has been suggested by [Iwabuchi et. al., 1994]. Particulate free thin films with very smooth surface have been obtained.

2.3 Mechanisms of Pulsed Laser Deposition

When the laser radiation is absorbed by a solid surface, electromagnetic energy is converted first into electronic excitation and then into thermal, chemical and even mechanical energy to cause evaporation, ablation, excitation and plasma formation. Figure 2.1 shows the schematic diagram of PLD. The evaporants form a "plume" consisting of a mixture of energetic species including atoms, molecules, electrons, ions, clusters, micron-sized solid particulates, and molten golbules. The collisional mean free path inside the dense plume is very short. As a result, immediately after the laser irradiation, the plume rapidly expands into the vacuum from the target surface to form a nozzle jet with hydrodynamic flow characteristics. The ablated energetic species then travel through the vacuum from the target surface to the heated substrate. In between, gas phase reaction of the ejected materials and the ambient gas molecules occurs. The ambient gas used depends on the type of thin films to be deposited. Oxygen gas is usually added for the oxides films. Once the ablated species reach the heated substrate surface, condensation and crystal growth begin.

There are three common modes of film growth in the initial stages. They are Frank-Van der Merwe, Volmer-Weber and Stranski-Krastanov [Lewis and Anderson, 1978; Venables et al., 1984]. Figure 2.2 shows the common modes of film growth. Frank-Van der Merwe mode is the growth of films layer-by-layer. It occurs when the cohesive energy between the films and the substrate atoms is greater than the cohesive energy of the film. Volmer-Weber is the island growth mode provided that

the cohesive energy of the film is greater than the cohesive energy between the films and the substrate, but monotonically decreases as each new film layer is added. Stranski-Krastanov mode consists of island growth after the first monolayer forms successfully. It occurs when the monotonic decrease in binding energy with each successive layer is energetically overridden by some factor such as strain energy due to lattice mismatch and island formation becomes more favorable. Naturally for high quality films and epitaxial single crystal films, Frank-Van Der Merwe mode of films growth is required. The Volmer-Weber mode, on the otherhand, is less desirable. However the different modes growth is perhaps only important for ultra-thin films (~nm) and not a matter of concern for films of $\geq$ 100nm thick. The present study involves PLD of films > 100nm thick and thus the type of modes of film growth is not the subject of our investigation.

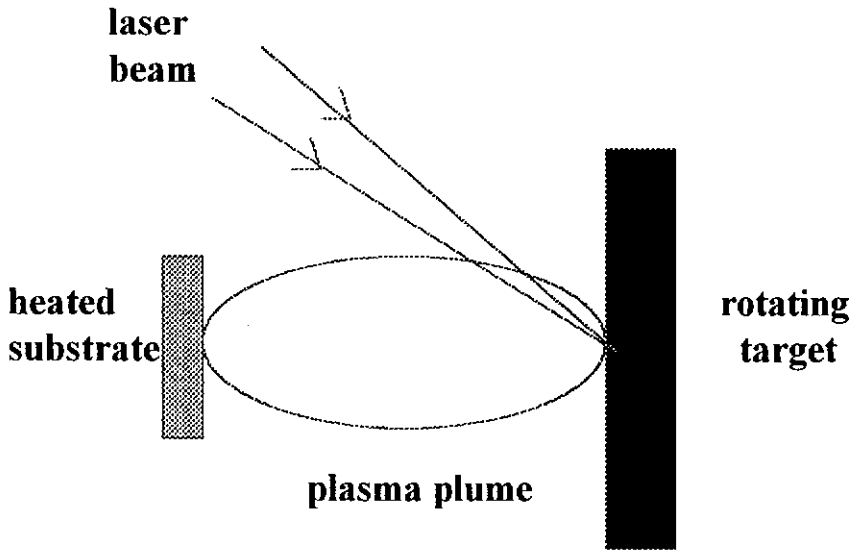

Figure 2.1 The schematic diagram of pulsed laser deposition.

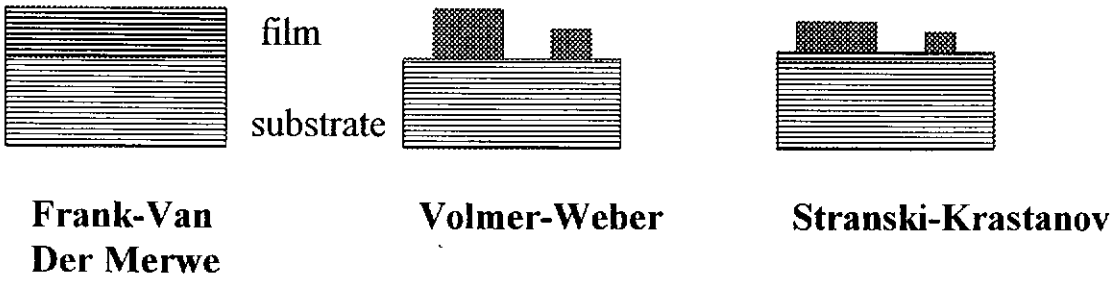

Figure 2.2 Three common modes of film growth.

Chapter 3

Giant Magnetoresistance (GMR) of Manganates

3.1 Introduction

Magnetoresistance is the change in electrical resistance of a material in response to a magnetic field. All metals have an inherent, albeit small, magnetoresistance owing to the Lorentz force exerts on moving electrons. Usually the change in resistance of metal films with application of a magnetic field is small [McGuire and Potter, 1975]. It was discovered in 1988 that the application of magnetic fields to atomically engineered materials known as magnetic superlattices greatly reduced their electrical resistance [Baibich et al., 1988]; that is, superlattices had a giant magnetoresistance. Superlattices are a special form of multilayered structures, artificially grown under ultra high vacuum conditions by alternately depositing on a substrate several atomic layers of one element, say iron, followed by layers of another, such as chromium. By stacking magnetic atoms into layers and alternating them with non-magnetic layers it has been possible to form magnetic superlattices whose electrical resistance are readily controlled by magnetic fields which align the moments of the magnetic layers relative to one another. The detail theory will not to be discssed in this thesis. Apart from the metallic multilayer structures, granular alloys also exhibit GMR effect. Granular alloys containing magnetic particles in a metallic host bare a strong resemblance to magnetic multilayers and GMR has been observed in a variety of magnetic granular systems,

predominantly comprised of Fe, Co, Ni and their various alloys in Cu, Ag and Au matrices.

In recent years, there are other materials system showing excellent GMR effect. They are the family of maganese oxides of perovskite-type structures. The magnetoresistance of the maganese oxides can be far greater than those obtained in the metallic superlattice, although a high field is needed to obtain saturation [Helmolt et al., 1993; Jin et al., 1994[a]; Manoharan et al., 1994; Ju et al., 1994[b]]. They are sometimes referred as colossal magnetoresistance (CMR) materials. The detail mechanism and the possible explanation of CMR will be briefly described in the following section.

3.2 Magnetic Properties and Giant Magnetoresistance in the Perovskite-like Manganates

3.2.1 Perovskite Oxides

Some oxides form a family of compounds with a crystal structure which is similar to the mineral perovskite, $CaTiO_3$. These materials have a general chemical formula of ABO_3 (A is a larger cation, B is a smaller cation). Figure 3.1 shows the perovskite structure of ABO_3. The ABO_3 perovskites exhibit very interesting physical properties such as dielectric ($BaTiO_3$) and ferromagnetic ($SrRuO_3$) effects [Goodenough and Lango, 1970]. The $LaMO_3$ (M is 3d transition element), on the other hand, shows different properties when M changes. $LaTiO_3$ and $LaNiO_3$ have metallic behavior [Crandles et al., 1991], $LaMO_3$ compounds are insulators when the M is V, Cr, Mn or Fe [Thornton et al., 1982]. When La is partially substituted by divalent elements, the complex perovskite compounds $La_{1-x}A_xMnO_3$ can be formed where A represents Ca, Sr, Ba or Pb. These compounds have several interesting physical properties. For example, $La_{0.79}Pb_{0.21}MnO_3$ has ferromagnetism and metal-semiconductor transition [Belov et al., 1978]. The compounds $La_{1-x}A_xMnO_3$ with $x > 0.2$ and A=Ca [Troyanchuk, 1992], Sr [Helmolt et al., 1992] and Ba [Bokov et al., 1968] have antiferromagnetic-ferromagnetic transition and also metal-semiconductor transition near the Curie temperature. The spontaneous magnetization from the existence of Mn^{4+} ions also occurs [Zener, 1951; Gennes, 1960]. Recently, the giant magnetoresistance (GMR) has been found for the La-Ba-Mn-O [Helmolt, 1993], La-Ca-Mn-O [Chahara et al., 1993; McCormack, 1994], La-Sr-Mn-O [Trajanovic, 1996]

and $Nd_{0.7}Sr_{0.3}MnO_3$ [Xiong et al., 1995] thin films and also polycrystal $Nd_{2/3}Sr_{1/3}MnO_3$ and $Sm_{2/3}Sr_{1/3}MnO_3$ [Caignaert et al., 1995] bulk samples.

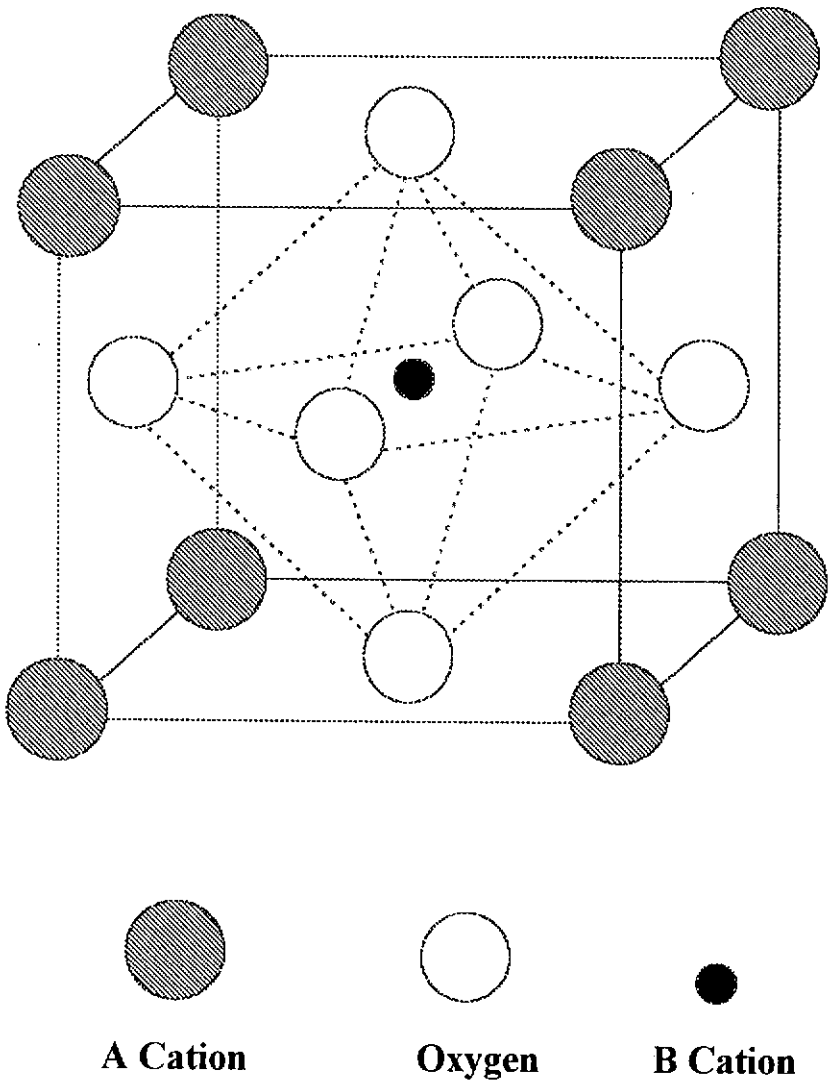

Figure 3.1 Perovskite structure of ABO_3.

3.2.2 Magnetic Properties

The neutron diffraction results show that there is an antiferromagnetic coupling between the Mn^{3+} cations in the undoped parent compound $LaMnO_3$ and the coupling is believed to be transferred by superexchange via the intermediate oxygen [Zener, 1951]. For the antiferromagnetic materials, they have a self antiferromagnetic coupling of the magnetic ions below the Neel temperature θ_N. When the temperature is higher than the Neel temperature, they are in paramagnetic. The spin structure of the undoped or slightly doped ($x < 0.1$) $LaMnO_3$ compounds has the ferromagnetic ordering in the a-b plane and antiferromagnetic ordering in the c-axis. Weak (or parasitic) ferromagnetism is observed even in the undoped compound and is interpreted as an intrinsic property. Figure 3.2 shows the magnetic structure of La-Ca-Mn-O system under the Neel temperature [Wollan and Koehler, 1955].

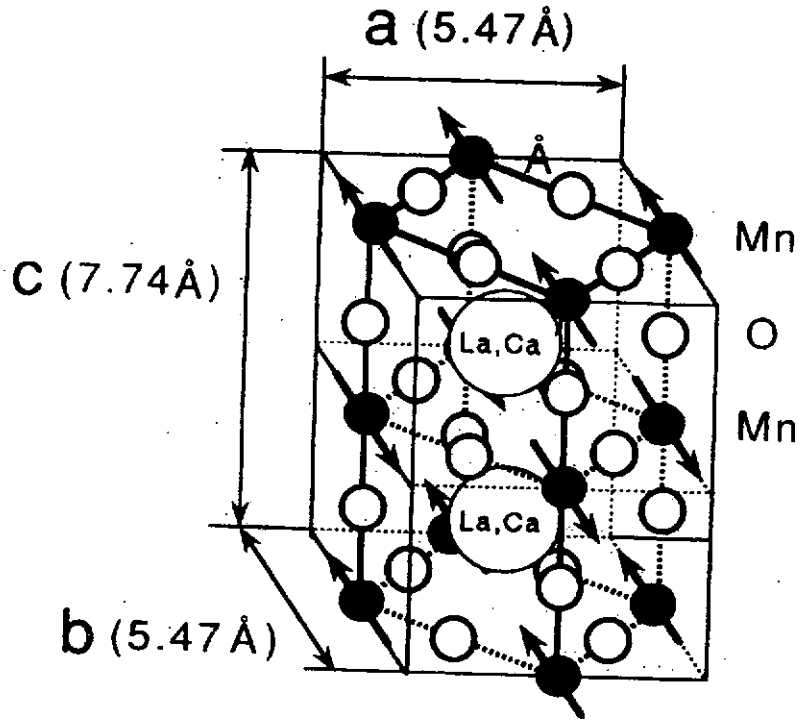

Figure 3.2 The spin structure of LCMO under the Neel temperature. [Wollan and Koehler, 1955]

When the La cations in the $LaMnO_3$ compound were partially substituted by the divalent Ca, Sr or Ba cations, part of the Mn^{3+} cations changes to Mn^{4+} cations and the formula will be presented as $La_{1-x}A_xMnO_3$ where A = Ca, Sr, Ba, or Pb. The perovskite-like oxide orders ferromagnetically instead of antiferromagnetically near room temperature for $0.2 < x < 0.5$ [Jonker and Santen, 1950]. The substitution of A^{2+} into the La^{3+} sites results in a mixed Mn^{3+}/Mn^{4+} valence. This leads to the occurrence of ferromagnetism and metallic conductivity. Zener was the first to develop the mechanism of Double Exchange (DE) to understand the occurrence of ferromagnetism together with metallic conductivity [Zener, 1951]. Figure 3.3 is an simple diagram to explain the mechanism of Double Exchange interaction.

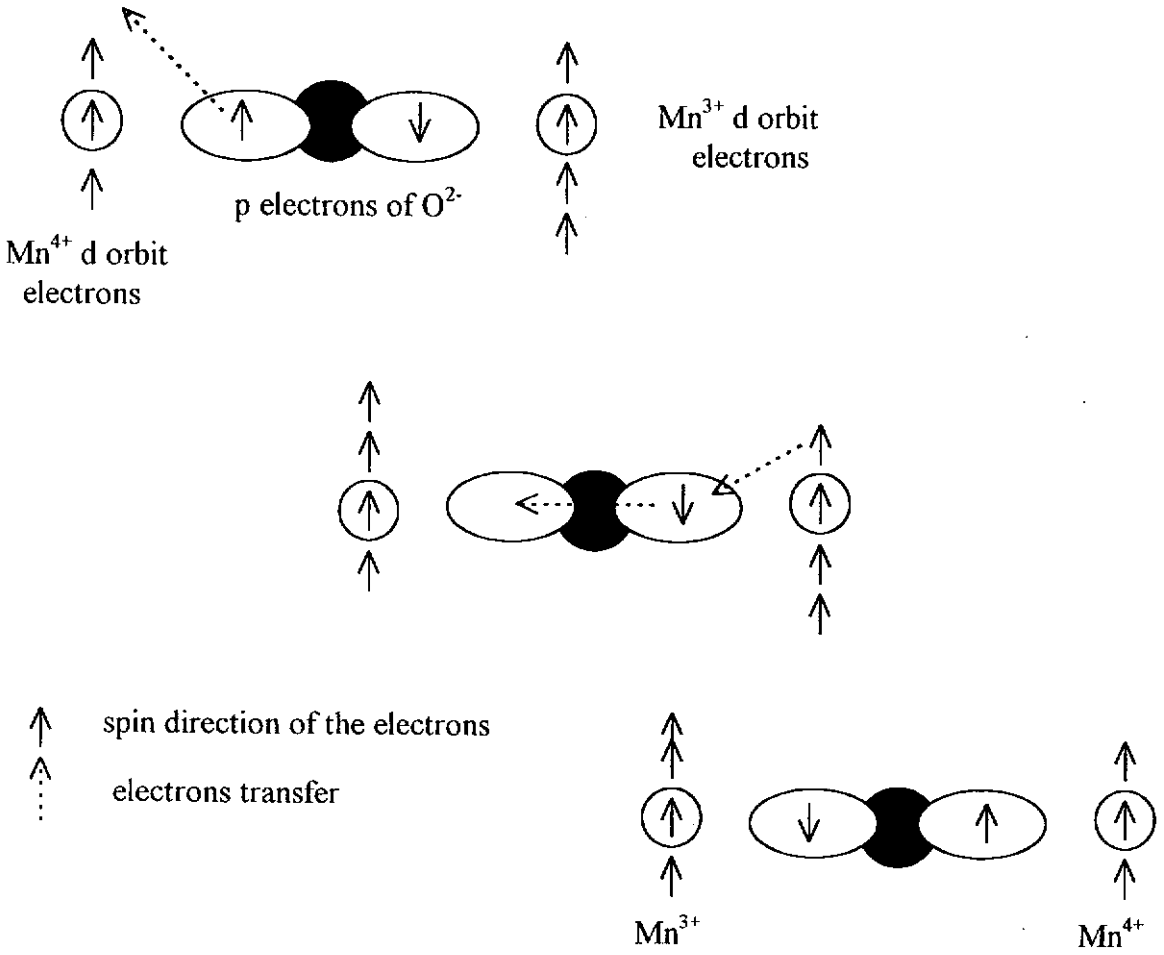

Figure 3.3 The mechanism of Zener's Double Exchange (DE) interaction.

Here the combination of the transfer of a p electron of O^{2-} to d orbit of Mn^{4+} on one side of O^{2-} and the transfer of d electron from the Mn^{3+} on the other side to p orbit of O^{2-} leads to electron conduction and an interchange of the positions of Mn^{3+} and Mn^{4+} ions without changing the energy. The process requires the parallelism of the spins of the related Mn^{3+} and Mn^{4+} ions and leads to ferromagnetism. It is interesting to note that the flowing electrons posses same spin direction. Thus it is actually a magnetization flow. The Double Exchange interaction strongly depends on the value of x, oxygen content and the type of dopants.

3.2.3 Electric Properties

For the ferromagnetic materials, the magnetic dipoles align ferromagnetically by itself and have a net magnetization under the Curie temperature, T_c. Above the T_c, the compounds are paramagnetic and will have a weak magnetization under an applied B-field. For the giant magnetoresistive materials, they exhibit metal-semiconductor transition. They are semiconducting at high temperature and metallic at low temperature. Upon warming from low temperature, the resistivity (ρ) increases with increasing temperature. In this region $\partial\rho/\partial T > 0$ and it is metallic like. The resistivity increases rapidly near T_c, and then decreases when $T > T_c$. Figure 3.4 shows the resistivities of a series of $R_{0.7}A_{0.3}MnO_3$ compounds in different temperatures [Coey, 1995]. For different compounds, they show a large variety of the absolute resistivities and metal-semiconductor transition temperatures.

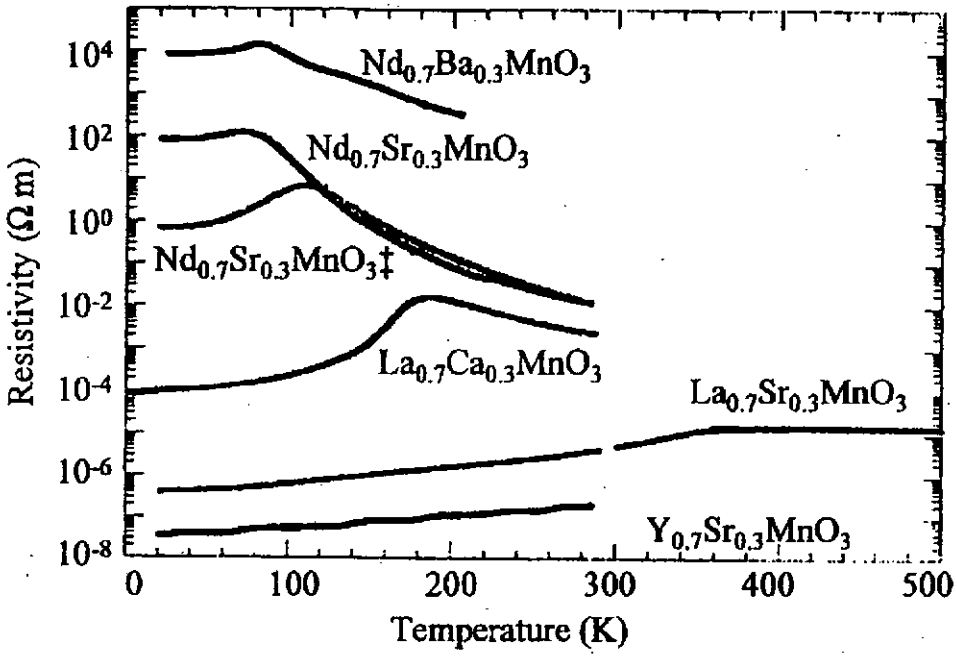

Figure 3.4 Resistivities of a series of $R_{0.7}M_{0.3}MnO_3$ compounds under different temperatures [Coey, 1995]

3.2.4 GMR in Doped Manganates

Manganates of the composition $La_{1-x}A_xMnO_3$ (M = Ca, Sr, Ba or Pb) are ferromagnetic for dopant concentrations in the range of about $0.2 < x < 0.5$. Metallic conductivity is observed in the ferromagnetic region. If the temperature is raised, a steep increase in resistance occurs near the Curie temperature. The resistance originates from the spin scattering of conducting electrons which is related to magnetic disorder. The higher degree of magnetic disorder, the more severe of the conducting electrons being scattered and hence larger resistance resulted. In the temperature range of magnetic ordering the resistance of the sample can be lowered by applying a magnetic field, which is supposed to reduce the effect of spin scattering. In Figure 3.5, the electrical resistivities of a $La_{0.67}Ca_{0.33}MnO_3$ thin film as a function of temperature under the B-field of 0T and 7T are shown [Bae, 1996]. The magnetoresistance in percentage was also plotted. There are two ways to present the magnetoresistance of a sample. The magnetoresistance ratio (MR) can be calculated by the following two different ways : $MR = (R_H - R_0)/R_0$ and $MR = (R_H - R_0)/R_H$ where R_H and R_0 are the resistance of the sample with and without an applied B-field. For the first one the MR% can not be bigger than 100% while the latter one can give a much bigger percentage value due to the fact that $R_H << R_0$. The MR is in negative sign as the resistance is lowered under an applied B-field.

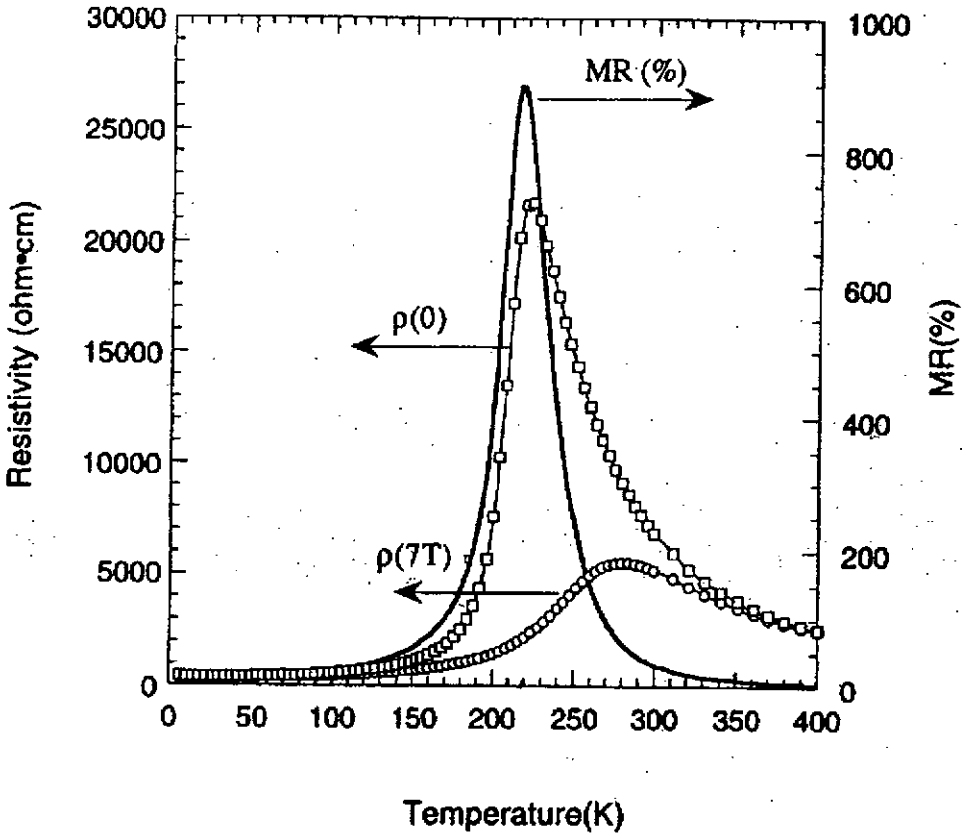

Figure 3.5 The electrical resistivities of a $La_{0.67}Ca_{0.33}MnO_3$ thin film as a function of temperature under different magnetic fields [Bae, 1996].

From the above figure, it is clear that the electrical resistance of a GMR sample can be reduced significantly by an external applied B-field. The resistance change can be well explained by the Zener's Double Exchange (DE) interaction discussed before. The conduction process of the electrons can be greatly enhanced if the surrounding magnetic ions were aligned ferromagnetically. The highest values of MR is obtained near the T_c, where an applied magnetic field induces the highest change of the magnetization, that is where the effect of the magnetic field on the disordered electrons spins is highest. At low temperature, $T << T_c$, the MR decreases, because the conductivity can not be changed by an applied field if the spin lattice is already ordered at zero field. One more interesting thing is the shifting of the peak resistivity to the higher temperature under an external B-field. This together with the DE effect result a large magnetoresistance effect.

3.3 Review on PLD of GMR Perovskite Manganates Oxide

Perovskite-like $La_{1-x}A_xMnO_3$ (A=Ba, Ca, Sr, and Pb) has recently attracted a lot of attention due to its unusual giant magnetoresistance (GMR), in which the electrical resistance of the materials changes by more than an order of magnitude under the effect of a magnetic field [Jin et. al., 1994[a]; McCormack et. al., 1994; Gu et. al., 1995; Treece et. al., 1995; Gong et. al., 1996]. Considerable effort has been focused on studies of expitaxial growth of LCMO thin films for potential device applications [Helmolt et. al., 1993; Gu et. al., 1995;]. Pulsed laser deposition (PLD) is known to be an excellent method for growing perovskite films such as superconducting $YBa_2Cu_3O_7$ and piezoelectric $PbZr_xTi_{1-x}O_3$ films [Huang et. al., 1994; Prouteau et. al., 1995; Yeh and Liu, 1995; Hau et. al., 1995, Chan et. al., 1996]. It has been demonstrated that good quality LCMO films on single crystal substrate can be obtained by the PLD method [Jin et. al., 1994[a]]. Usually the films were either grown at a relatively high substrate temperature of above 750°C or the as-deposited films annealed under ambient oxygen at high temperature (900°C) for a prolonged period (> three hours) [Jin et. al., 1994[b]]. Magnetoresistance ratio (MR = $(R_0 - R_H)/R_0$) of > 80% under the influence of a high magnetic field (≥ 6T) has been reported [McCormack et. al., 1994; Gu et. al., 1995; Bae and Wang, 1996]. In industry, several criteria should be satisfied in order to make use of them. Magnetoresistance effect should be observed at room temperature and under an applied B-field of as low as tens or hundreds of Oe, and high quality thin films should be prepared on semiconducting substrates such as Si wafer. Unfortunately, usually, the magnetoresistance effect observed at temperature lowerer than room temperature.

Actually, the value of T_c can be changed by varying the deposition and processing parameters, and doping with different type of dopants. Lots of attention have been paid on raising up the Curie temperature, T_c, by using different types and level of dopants. The B-field employed is also high in the order of Tesla. Indeed, the sensitivity of the resistance change response to the magnetic B-field is much more to be concerned than the absolute MR% value. For example, industrially useful GMR metallic multilayer has the sensitivity of fraction of percent per Oe while in literature the GMR manganates perovskites has the sensitivity of few percents per kOe. Hence, it need further work to improves the sensitivity for those manganates perovskite oxides so as to use them in industry. In this project, we emphases the preparation of high quality giant magnetoresistive LCMO films on Si substrate to obtain MR% comparable with the LCMO films grown on single crystal LAO substrate.

More recently, attemps have been made to prepare the giant magnetoresistive perovskite manganates oxides on Si substrates. Zhang and Boyd in 1996 presented the magnetoresistive behavior in LCMO films grown on Si without any buffer layer [Zhang and Boyd, 1996]. Mixed orientation of (100), (110) and (111) LCMO films were obtained. They showed that the deposition at a high temperature shifts the resistivity peak to lower temperatures and simultaneously increases the maximum resistivity value. Annealing at a high temperature, however, produces the opposite effect on the resistivity behavior. They suggested that the poor electrical transport properties for LCMO films deposited at high substrate temperature was due to oxygen deficiency in films. Post annealing , on the other hand, helped to improve the oxygen incorporation. The maximum MR value ($MR = (R_H - R_0)/R_0$) of the LCMO

films were 32% at 5.7K and 20% near room temperature under a magnetic field of 4.7T.

At the same year, Kung and Fenner showed that LCMO films with (100) and (110) mixed orientations were obtained on Yittrium-stablised Zironium (YSZ) - buffered Si(100) and Si(111) substrates [Kung and Fenner, 1996]. The best magnetoresistance was observed in the single-phase, epitaxial (110), and this structure was grown with the best quality on the YSZ(111)-buffered Si(111) substrates. These films showed higher transition temperatures and peak ressitivity than those in the (100) films. Under a magnetic field of 5T, the maximum MR% (MR = $(R_H - R_0)/R_H$) in the as-deposited (110) and (100) films were 250% at 195K and 164% at 140K respectively.

Chapter 4

Experimens and Set-up

4.1 Instruments

4.1.1 PLD System

4.1.1.1 Excimer Lasers

Excimer laser is a type of pulsed laser which can emit high flux of UV photons. In our case, we used a XeCl excimer laser (Lumonics TE-860-4) and a KrF excimer laser (Lamda Physik Compex 205) for the deposition of thin films. For the XeCl excimer laser, the excimer molecules were formed in a gaseous mixture of their component gases, such as Xe, HCl and Ne. The total gas pressure of the laser chamber was 60 psi (1 psi = 51.7151 Torr) where the partial pressure of Xe was 40 Torr, HCl was 60 Torr and the remaining gas pressure was balanced by Ne gas which act as the buffer gas. For the KrF excimer laser, the gases used were F_2, Kr, He and Ne. The total gas pressure of the laser chamber was 3400 mBar (1 Bar = 750.06 Torr) where the partial pressure of F_2 was 4 mBar, Kr was 130 mBar, He was 56 mBar and Ne was 3210 mBar. The ionic and electronically excited species were created by the avalanche electric discharge excitation (about 40kV). Then the excited species react chemically to produce the excimer molecules. At the same time, laser transition take place during the dissociation of the excimer molecules as the ground state is repulsive and they rapidly dissociate. The wavelength of the light emitted is 308nm for XeCl and 248nm for KrF. The XeCl laser in our laboratory can produce a

maximum energy of about 100mJ per pulse whereas the KrF laser can provide up to 600mJ per pulse.

4.1.1.2 Optics

The whole deposition system consists of a number of optics components such as mirror, lenses and attenuators. A mirror was used to redirect the laser beam from the laser to the deposition chamber and lenses were used for focusing the laser beam onto the target surface inside the vacuum chamber. The focal length of the lenses were 25cm and 50cm for the XeCl and KrF lasers respectively. Between the mirror and the lens, attenuators made of tilted fused silica plates were placed in order to adjust the energy of the laser beam. Hence, the laser fluence falling onto the target surface can be varied without changing the focusing conditions.

4.1.1.3 Vacuum Chamber

Once the laser beam has passed through the optics, it enters the vacuum chamber through a fused silica window. Figure 4.1 shows the schematic diagram of the deposition system. The vacuum chamber, has several ports and they were used for heater, pressure gauge, gas inlet, target holder, laser window and viewing window.

The heater was made of stainless steel and it was heat-shielded by a few thin plates of stainless steel wrapped around the side of the heater. We used Kanthal wire (25% chromium, 5% aluminium, 3% cobalt and 67% iron) as the filament inside the heater for heating purpose. The diameter of the Kanthal wire is 0.559 mm and the resistance per unit length is 5.1 Ωm^{-1}. A total resistance of the Kanthal wire used was

15 Ω. A K-type (Nickel-Chromium, Nickel-Aluminium) thermocouple was inserted into the heating block for the measurement of the substrate temperature. The temperature was controlled by a temperature controller (PAC25-0321) capable of operating temperature range of 0°C - 1400^{0}C. The substrates were pasted onto the top of the heating-block with silver paste (G3691) as it has good heat conduction and can provide good adhesion between the heating block and the substrates.

The base pressure of the vacuum chamber was monitored by an ionization gauge (Type WI-T). The ambient gas pressure during deposition and post-annealing was measured by a Baratron pressure gauge (MKS Baratron® Type 122A) which was mounted on one of the chamber port. A digital meter (MKS Type PDR-D-1 Power Supply Digital Readout) was connected to the pressure gauge to display the value. The pressure range that can be measured was 1 mTorr - 12 Torr with the accuracy of ± 0.01% of F.S.

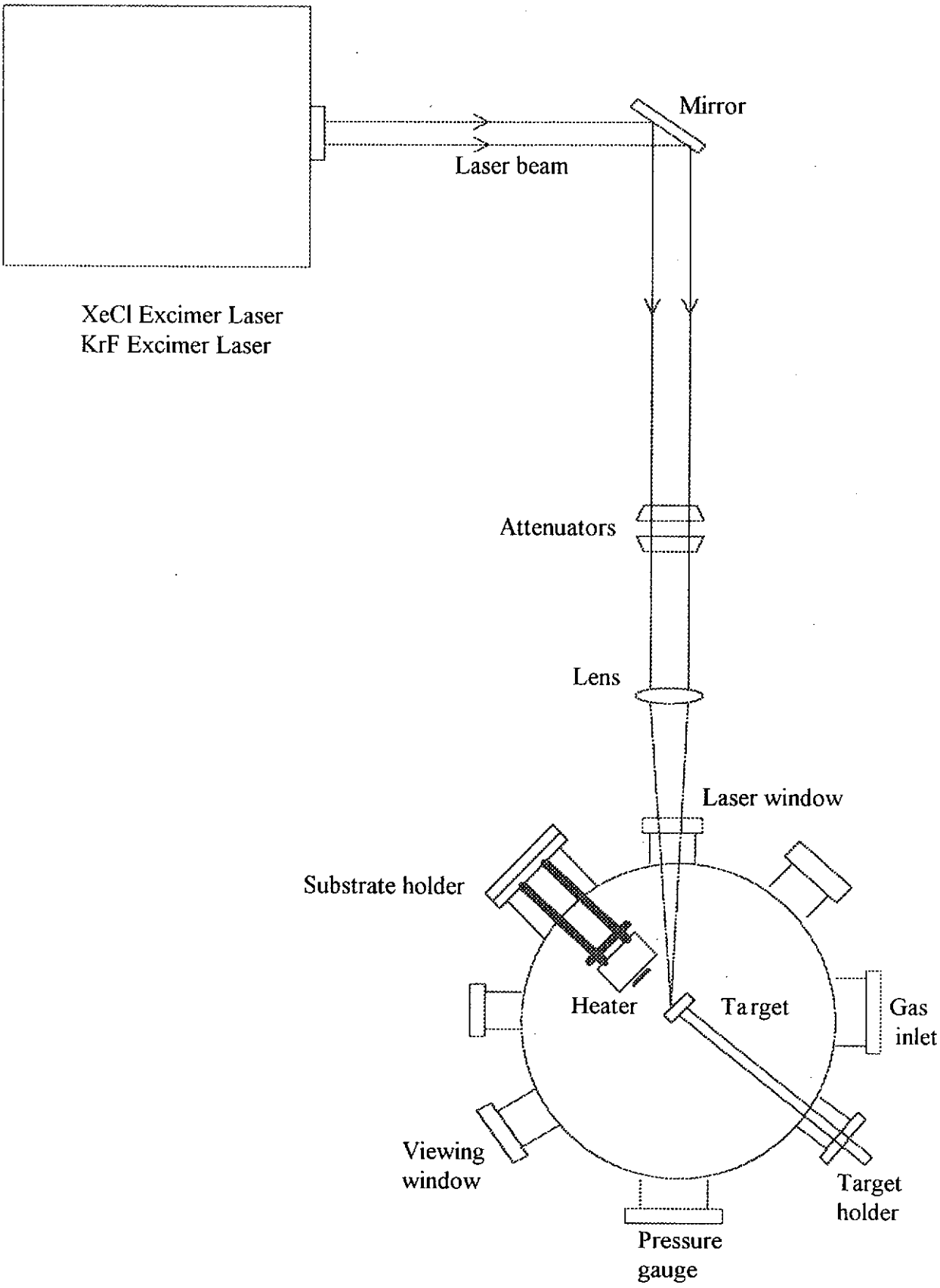

Figure 4.1 The Schematic diagram of the pulsed laser deposition system.

The gas-inlet lets in the required gas from outside into the chamber during the deposition. The type of gas used depends on the kinds of deposition materials. For example, to deposit ceramics oxide thin films, oxygen gas should be filled in order to provide a ambient oxygen environment for the thin films deposition. The gas flow rate was controlled by a gas regulator and valves.

The ceramic targets were mounted on a target holder. During the deposition, the target was rotated by a d.c. magnet motor (24V, 4W, part no.: 2511G-244). The rotation of the target was to ensure that the materials of the target was evenly ablated by the laser beam and to avoid pitting on the target surface.

The laser window was used for allowing the laser beam to enter the chamber to ablate the target surface. The viewing window allow us to observe the situation inside the vacuum chamber during the deposition as well as for in situ alignment. Both windows were made of fused silica without AR coatings. Laser beam attenuation through the window is typically less than 10%.

4.1.2 X-ray Diffractometer (XRD)

The crystal structures of the thin films were characterized by using an X-ray diffractometer (Philip mode X'pert system) in four-circle mode. The K_α radiation of Cu (λ=1.54 Å) was used and the K_β line was filtered by Ni filter. Figure 4.2 showed the X-ray diffraction of a crystal. When X-rays fall on atoms in a crystal, each atom scatters a small fraction of the incident beam. Thus the reflected beams from all atoms in the crystal planes involved may interfere and the resultant reflected beam is only

strong if the path difference between successive planes is a whole number of wavelength of the incident X-ray radiation. Thus reinforcement only occurs for planes p and q when AB+BC=nλ where n is an integer and λ is the wavelength of the X-rays. If d is the distance between planes of atoms and θ is the angle between the X-rays beam and the crystal plane, then AB+BC=2d sinθ and the reflected beam has maximum intensity when

$$2d \sin\theta = n\lambda \quad \text{(Bragg's Law)} \qquad \text{.....(4.1)}$$

and the d value was calculated as:

$$d = a/(h^2+k^2+l^2)^{1/2} \qquad \text{.....(4.2)}$$

where a is the lattice constant of the crystal structure and *h*, *k* and *l* are the reciprocal lattice indices for a-axis, b-axis and c-axis respectively.

For example, to calculate the 2θ angle of (400)Si:

a = 5.43Å for (100)Si, λ = 1.54Å for K_α radiation of Cu in X-ray,

then $d = 5.43/(4^2+0+0)^{1/2}Å = 1.3575Å$,

hence, $2\theta = 69.11°$

Several modes of scanning of the X-rays were used for characterization of the crystal structure of the thin films. 2θ-θ scan, θ scan and ϕ scan were involved for the characterization of the epitaxy of the thin films prepared. Figure 4.3 shown the three axes rotation of the sample, i.e. θ axis, φ axis and ϕ axis. For the normal 2θ-θ scanning, it is commonly used to determine the crystal phase formed with the orientation normal to the substrate surface. The degree of orientation of a certain

peak or phase is reflected by the Full Width Half Maximum (FWHM) of the rocking curve in performing the θ scan. The rocking curve is done by fixing the 2θ value at the peak of interest and varying the angle θ. The smaller the value of FWHM of the rocking curve, the better are the crystallinity and orientation of the films. To confirm the epitaxy of the thin films, a 360° ϕ scan should be additionally made. It is done by fixing 2θ and θ angles corresponding to the (220) substrates or films and setting the angle φ to 45°. Four ϕ-scan reflections of the substrates or films which corresponding to (220), $(2\bar{2}0)$, (202) and $(20\bar{2})$, respectively would be obtained. The ϕ scan is used to characterize the in-plane epitaxy of the films deposited on the substrate. For good epitaxial cubic structured films, four characteristic peaks separated by 90° are observed and coincided with those of the substrate.

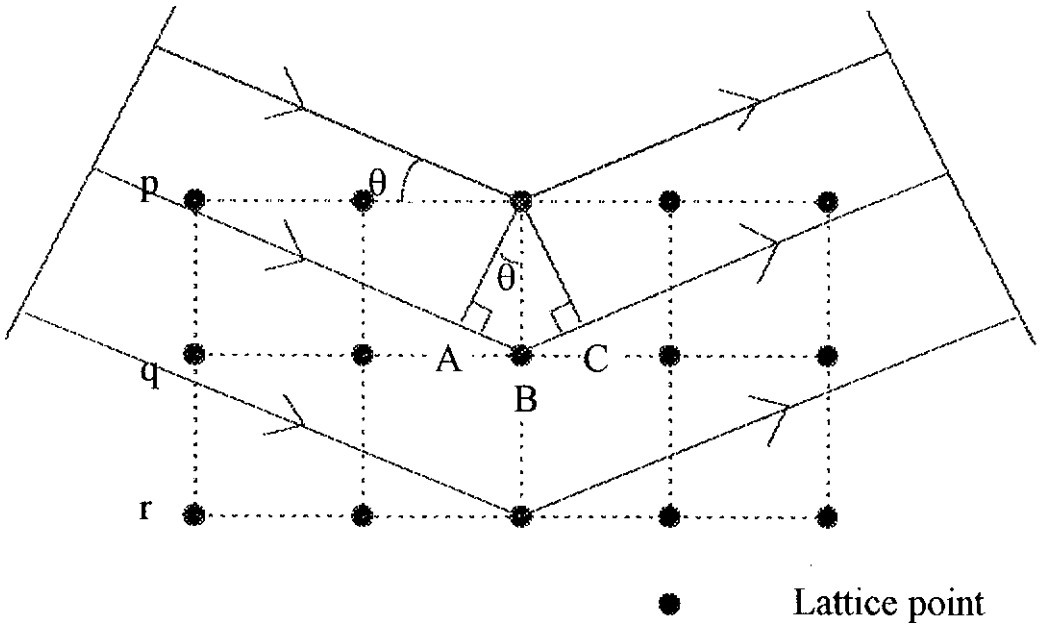

Figure 4.2 The schematic diagram of X-ray diffraction of a crystal.

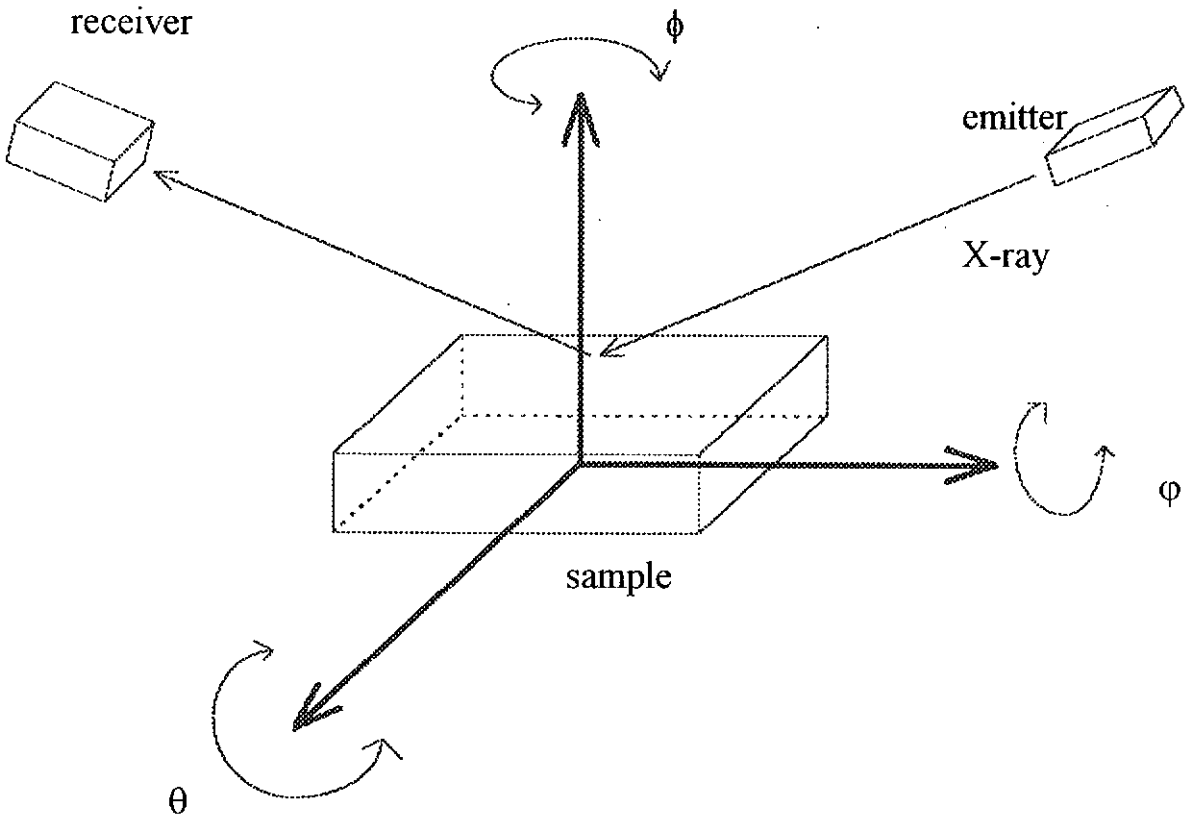

Figure 4.3 The rotation axis of the sample relative to the X-ray emitter and receiver.

4.1.3 Four-Point Probe

The resistivity (ρ) of a sample is defined as $\rho = R\ A/l$. Figure 4.4 shows how the ρ relates to the geometry of the sample in the measurement of resistivity. The current I flows through the sample with cross sectional area A and sample length *l*. A four-point probe is an instrument used for measuring the resistivity (ρ) of the samples. Figure 4.5 shows the four-point probe set up for the measurement of ρ of the prepared sample. The outer two electrodes provide constant current flowing through the sample whereas the inner two electrodes measure the potential difference between the two points. The calculation of ρ is not straightly using the above equation, Uhlir in 1955 showed that a correction factor should be added in order to eliminate the geometry factor effect [Uhlir, 1955].

$$\rho = \frac{\Delta V \pi t}{I \ln 2} \qquad (4.1)$$

where I is the constant current applied, ΔV is the measured potential difference and t is the thickness of the sample. Unlike the two point probe where the measured potential difference includes the contact resistances between the wires and the electrodes, the use of four-point probe can eliminate the potential difference due to the contact resistances as there is little current passing through to the inner electrodes when the sample is a good conductor.

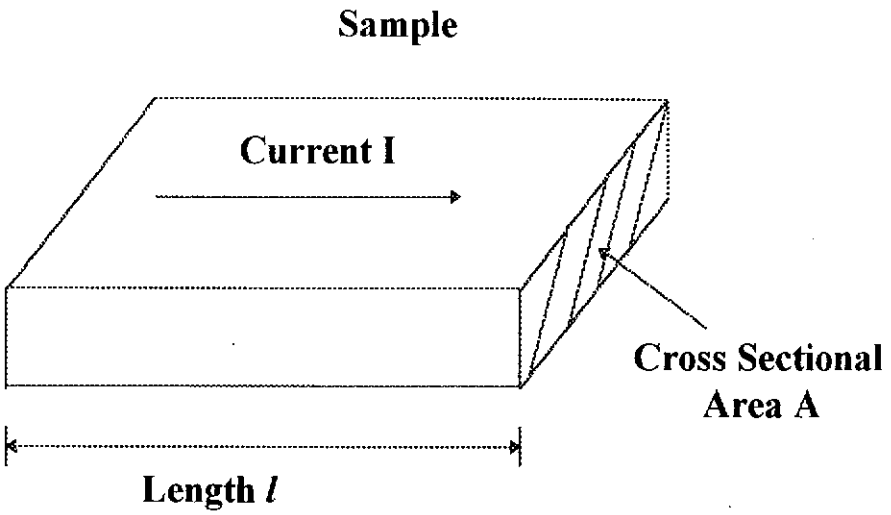

Figure 4.4 The geometry of the sample in the measurement of resistivity ρ.

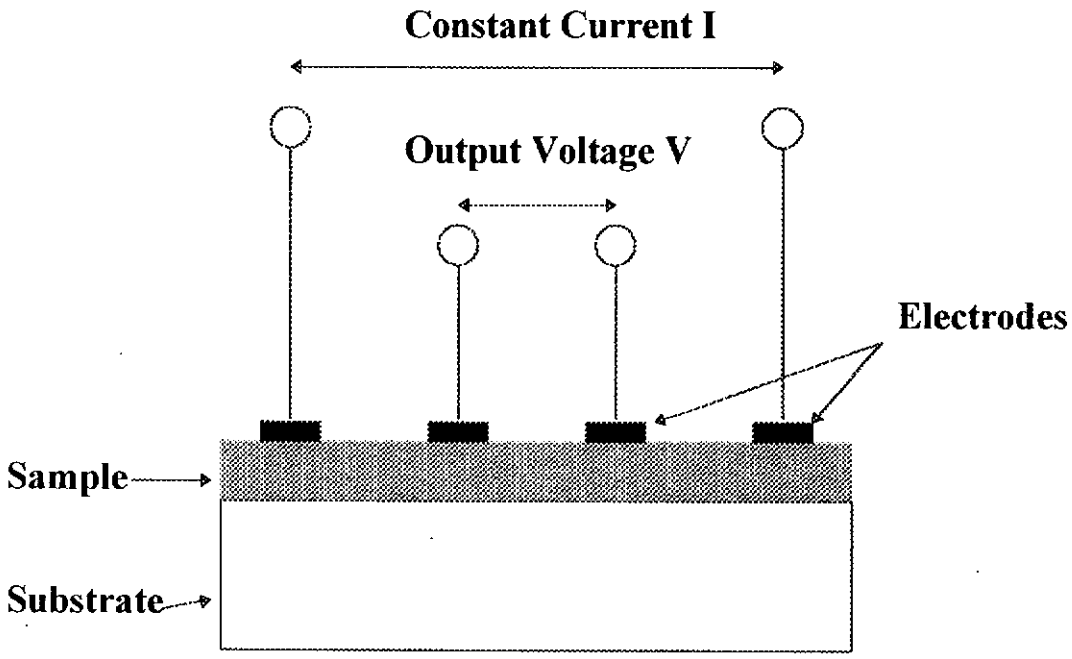

Figure 4.5 The schematic diagram of the four-point probe set-up.

The constant current source circuit for our four-point probe measurement is shown in Figure 4.6(a). A standard 747 Operational Amplifier configured in a negative feedback inverting amplifier mode was used to maintain a constant current flowing through the feedback loop even if the resistance of the sample changes widely. The value of the voltage supply and the resistance of the resistors were selected so that the circuit can produce a constant current of 0.1 mA. The value of the constant current can be adjusted either by varying the supply voltage or the value of the resistors. For the samples with different resisitivity, different value of constant current should be used in order to get measurable signal as the output of the Operational Amplifier is limited to about 14V. Similarly, Figure 4.6(b) shows the constant current circuit for the Pt thermometer which was used to monitor temperatures down to liquid nitrogen temperature of 77K. A constant current of 1 mA was maintained in this circuit. Hence, the measurement of sample resistivity under different temperatures can be made using these two constant current circuits.

4.1.4 Electromagnet

For the measurement of the magnetoresistance ratio (MR) of the magnetoresistive films, a constant B-field should be applied parallel to the plane of the sample. In this study, a maximum constant B-field of 1.2 Tesla was employed. The constant B-field was obtained through the electromagnet of a LDJ Model 9500 Vibrating Sample Magnetometer (VSM). The system was computer controlled and provided a uniform B-field in the range of 0T - 1.2T.

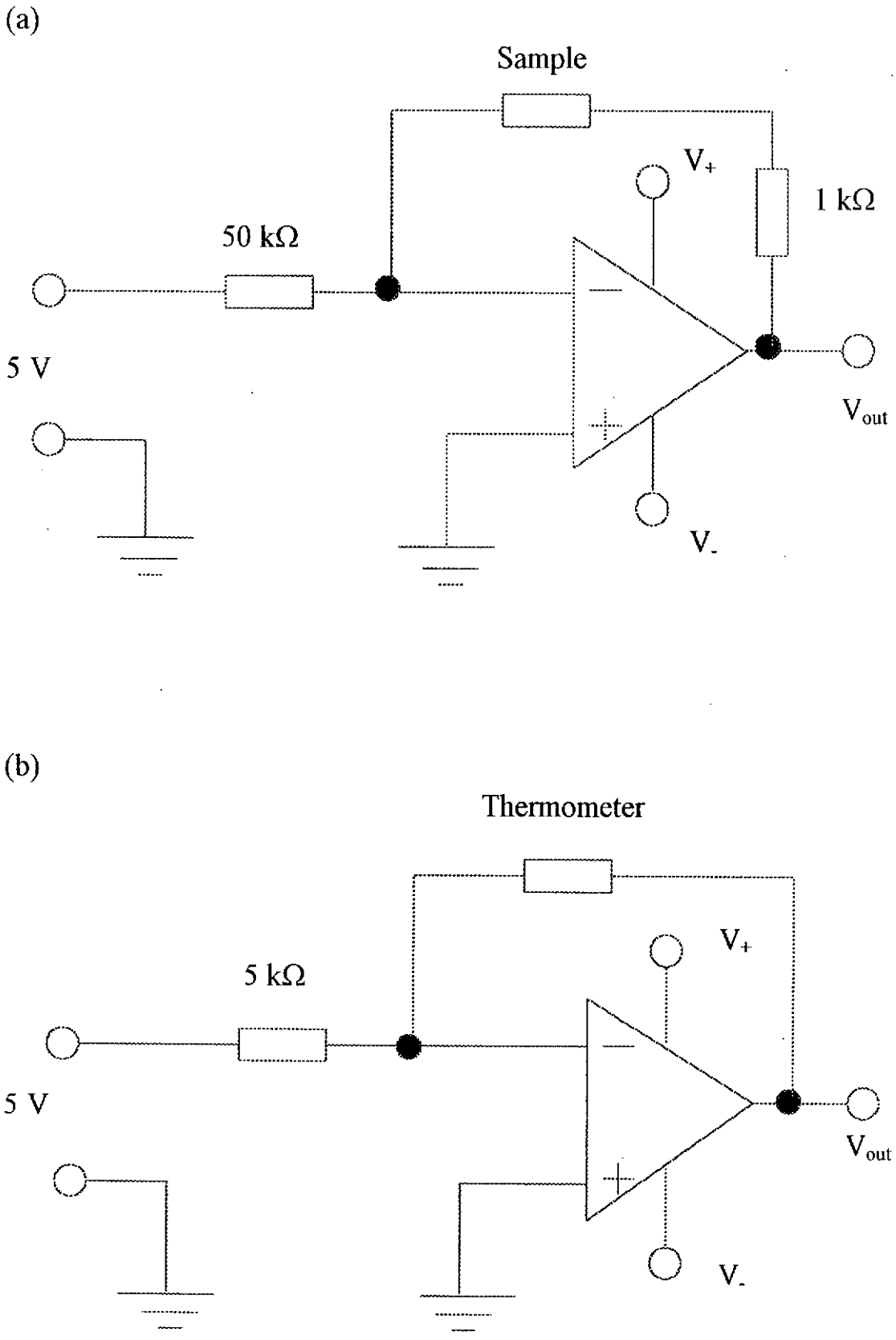

Figure 4.6 The constant current circuits of (a) the sample and (b) the thermometer.

4.2 Experimental Procedures

4.2.1 Ceramic Oxides Targets Fabrication

4.2.1.1 LCMO Targets Fabrication

The $La_{1-x}Ca_xMnO_3$ (LCMO) target was fabricated by using the standard solid state reaction method. We used chemicals of high purity AR grade Manganese dioxide (MnO_2), Calcium carbonate ($CaCO_3$) and Lanthanum oxide (La_2O_3) for the reaction to form the required LCMO compound. The value of x can be varied by using different proportion of the oxides. In this study, chemical composition of the LCMO target was $La_{0.67}Ca_{0.33}MnO_3$. The following shows an example of how to obtain the required mass of different oxides.

Molar mass of:

$La_2CaMn_3O_9$	= 626.61g	(for simplicity)
La_2O_3	= 325.8g	
$CaCO_3$	= 100.09g	
MnO_2	= 86.93g	

If 0.01 moles of $La_2CaMn_3O_9$ is to be fabricated, the masses of the oxides required are:

La_2O_3	= 0.01×325.8g	= 3.26g	(two decimal places)
$CaCO_3$	= 0.01×100.09g	= 1.00g	
MnO_2	= 3×0.01×86.93	= 2.61g	

After the desired proportion of oxides were weighed, they were all put into a bottle with steel balls. The bottle was then rolled by a rolling machine for two to three hours to make sure that the oxides powder was evenly mixed. The powder was then compressed by a oil-compressor at pressure of 500Kg/cm^2 into a disc-pellet with the

required dimension. The compressed pellets were sintered at a temperature range of 1100 °C-1400 °C for 8 hours. The samples thus formed after sintering were crushed and ground by mortar and pestle. They were again compressed into pellets. The whole processing procedure were repeated for three times included the sintering process. The composition of the final $La_2CaMn_3O_9$ targets were verified by EDX (Link Analytical AN10000).

4.2.1.2 STO Targets Fabrication

The $SrTiO_3$ (STO) target fabrication process was very similar to that of LCMO target. High purity AR grade of Titanium Dioxide (TiO_2) and Strontium Carbonates ($SrCO_3$) were used to fabricate STO target. The molar mass of the chemicals and the amount of them used are listed below:

Molar mass of:

TiO_2 = 79.9g
$SrCO_3$ = 147.63g

For 0.02 moles of STO is to be fabricated, the masses of the chemicals required are:

TiO_2 = 0.02×79.9g = 1.60g (two decimal places)
$SrCO_3$ = 0.02×147.6g=2.95g

The grinding and sintering processes were the same as in the fabrication of LCMO targets.

4.2.2 Thin Films Fabrication

In the present study, LCMO, TiN and STO thin films were deposited using the PLD system which has been described previously in section 4.1.1. The targets (LCMO, TiN and STO) were mounted on the rotating target holder. For the deposition of multilayer thin films, the films were in-situ deposited by means of a multi-target holder as shown in figure 4.7. The targets were mounted on the same rotating stainless steel rod. The laser beam was focused onto the round surface of the pellet targets. The selection of the target to be ablated can be achieved by adjusting the height of the rod. The target was translated vertically as to avoid digging a ring on the cylindrical surface of the target. The substrates were pasted to the heater by silver paste, which can act as a heat conducting medium. The substrates used were mainly single crystal of (100) Lanthanum Aluminium Oxide ($LaAlO_3$ (LAO)) and (100) Silicon (Si). The substrate temperature employed in this study was in the range of 500 °C-800 °C and the target-substrate distance was 4cm. Heating was provided from the power rated filament and the temperature was controlled by a temperature controller. Before the deposition, the chamber was evacuated by rotary pump and cryo pump. The rotary pump can produce a vacuum of 10^{-3} torr while the cryo pump can produce a vacuum of $\leq 10^{-6}$ torr. The type of pump used depended on the kinds of films to be deposited. For the deposition of LCMO thin films, rotary pump alone was used because additional oxygen gas (about 200 mtorr) would be introduced into the chamber during the deposition. While for the deposition of TiN and STO thin films, both the rotary pump and cryo pump were operated as high vacuum was needed. After the substrate temperature and the vacuum had reached the desired values and was stable, the laser was switched on and pulsed at a repetition rate of 10 Hz. The

laser pulses were allowed to focused onto the rotating target surface. The materials ablated from the target were deposited to the heated substrate. The choice of deposition time can conviently control the thickness of the thin films. Two types of films, namely the as-deposited films and the post-annealed films, were fabricated. The as-deposited films were obtained when the film was cooled down slowly after the deposition was completed. For post annealing, the films were kept at the same temperature as the deposition temperature for a prolonged period of time under a high ambient gas pressure (for example, 1 atm O_2 for LCMO films for 1 to 3 hours). The post-annealing process was mainly used to improve the crystallinity and to reduce the oxygen deficiency of the films.

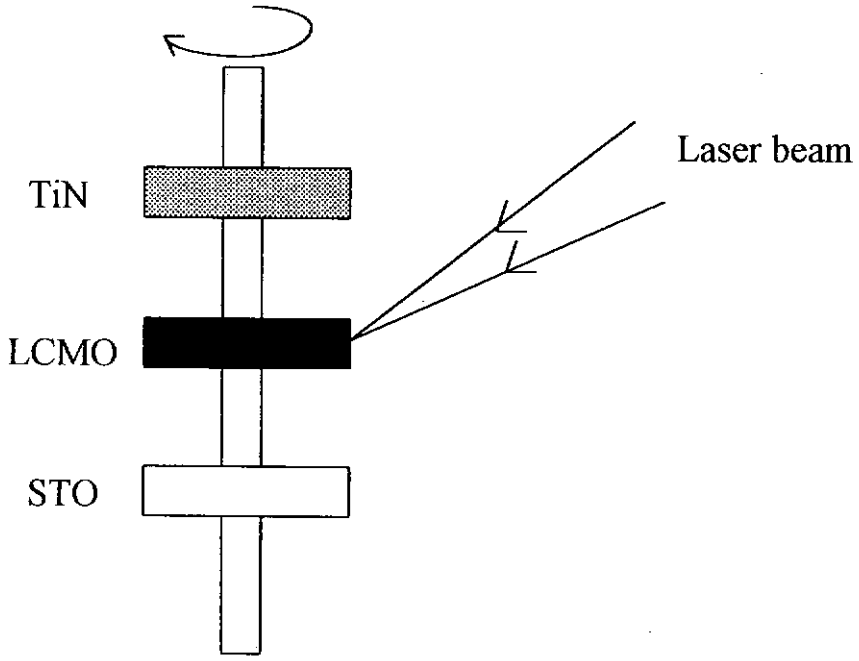

Figure 4.7 The schematic diagram of the multi-targets holder for in-situ deposition of multilayers thin films.

4.2.3 Structural Analysis of Thin Films

The structure of the thin films was characterized by X-ray diffractometry (XRD) which was discussed previously in section 4.1.2. For the characterization of the epitaxy of the thin films, 2θ-θ scan, θ scan (rocking curve) and ϕ-scan were performed.

By performing the 2θ-θ scanning, the lattice planes of the thin films grown with the direction parallel to the normal direction of the substrate surface can be observed. For the epitaxial growth of thin films, only one set of planes of a family (e.g. (h00)) should be seen and it needs to be the same as the substrate (i.e. (h00)). If two or more sets of planes from different families were observed in the 2θ-θ scan, the films were multi-phased and were not epitaxially grown on the substrates. But, even if we obtain just one set planes from a single family of peaks in the 2θ-θ scan, there is no guarantee that the films are epitaxially grown on the substrates. All we can conclude is that the films are highly oriented in this direction. There is a possibility for the poor plane-to-plane alignment such as twisting between planes.

The degree of orientation can be characterized by the rocking curve. The rocking curve was done by fixing the 2θ value of the selected peak, the angle θ was then scanned for a few degree. The value of the Full Width Half Maximum (FWHM) reflected the degree of the orientation of the films. The smaller the value of the FWHM, the higher the degree of the orientation. Typically a FWHM of a few degree

is considered to be an oriented films, FWHM of ~ 1° is good oriented films and FWHM ≤ 1° is classified as highly oriented films.

To confirm that the films were epitaxially grown on the substrates, an addition ϕ-scanning was performed. As all of the films (TiN, STO and LCMO) and substrates (Si and LAO) employed in this study were in cubic structures, this scan was used to determined whether the grown films were lattice matched and "cube-on-cube" growth on substrates. For the normal 360° ϕ-scan of a cubic structural film, four peaks were observed. Each peak was separated by 90°. If the four peaks of the film were on the same phi angles as that of the substrate, we can say that the film was epitaxially grown on the substrate. In performing the ϕ-scan of the films, the angle φ should be tilted to 45° otherwise we cannot locate the cubic orientation i.e. cannot obtain the four peaks in the ϕ-scan. Usually higher order plane diffractions were used for good lattice matched substrate in order to obtain resolved peaks from the film and the substrate. In this study, (220) plane of the crystal was selected for performing the ϕ-scan. The θ and the 2θ values implied in the ϕ-scan were calculated from equations (4.1) and (4.2).

4.2.4 Electric Properties Measurements of the Thin Films

The electric properties of the fabricated thin films (LCMO and TiN) were measured by a standard four-point probe as shown in figure 4.5. After the thin films were deposited on the substrate, four electrodes were coated onto the film surface. The electrodes were prepared by the showdow pattern sputtering of gold target using Ar^+ ions. Indium was then welded onto the gold-electrodes for connection to the conducting wires. Afterwards, a constant current I was flown through the sample from the two outer electrodes. A voltage V between the two inner electrodes was measured and output to the y-axis of a plotter. The x-axis of the plot was the voltage measured from the Platinum thermometer under different temperatures. Using a constant current supplied to the four-point probe, the change in the voltage V was directly proportional to the change in the resistivity of the films. The resistivity of the sample was calculated by the equation of $\rho = \frac{\Delta V \pi t}{I \ln 2}$, where I is the constant current applied, ΔV is the measured potential difference between the inner electrodes and t is the thickness of the sample. Hence, the resistivity changes under the temperature from 300K (room temperature) to 77K (liquid nitrogen) of the sample were obtained. The plots obtained were finally digitized by a digitizer to an ASCII data file and then imported to the computer for further processings.

For the LCMO films, semiconductor-to-metal transitions were observed in the scanning of temperature range of 77K to 300K. Two important data should be noted from the resistivity vs temperature (R-T) plots; they were the value of peak resistivity and the temperature at peak resistivity. These two figures reflect directly the quality

of the fabricated LCMO films. For the TiN films, however, only a straight line with a positive slope was obtained in the R-T plots indicating a metallic characteristic. The absolute values of the resistivity at different temperatures can be measured from the plot and provide indications of the quality of the films.

4.2.5 Magnetic Properties Measurements of the LCMO Thin Films

The primary objective of measuring the magnetic properties of the fabricated LCMO thin films is to obtained the magnetoresistance ratio (MR) profile. In these measurements, a constant B-field was set up in the gap between the poles of the electromagnet of the VSM. The procedures for measuring the MR were similar to that of the measurement of the electric properties of the thin films except that an addition constant B-field was applied to the samples parallel to the current direction and the sample surface. When the sample was cooled down close to the liquid nitrogen temperature, the probe which contained the sample and was well insulated from outside was inserted into the region of constant B-field. The maximum B-field employed in this study was 1.2T. The resulting resistivity change with the temperature was presented by the R-T plots. As a result, there were two curves obtained for sample; one was the R-T curve without B-field and the other was the R-T curve under an applied constant B-field. The MR profile as function of temperature was obtained by taking the y-axis differences of the two R-T curves. As the films were in cubic structure, they were isotropic material. The applied B-field parallel or perpendicular to the sample current produced the same value of the MR %.

Chapter 5

Fabrication and Characterization of LCMO/LAO

5.1 LCMO Target Characterization

The LCMO target was fabricated by using the standard solid state reaction method. The target composition was initially intended to be $La_{0.67}Ca_{0.33}MnO_3$. The prepared targets were examined by EDX and the composition was determined to be $La_{0.7}Ca_{0.3}MnO_3$ which was very close to the desired value. The reason for this small change is properly due to the difference in boiling point temperatures of the elements. The boiling point of elements of La, Ca and Mn are 3455°C, 1484°C and 2061°C, respectively. La has the highest boiling point and hence very difficult to be vapourized, whereas Ca has the lowest boiling point making it more easy to be vapourized. The boiling point of Mn lies between that of the La and Ca. Thus, it is reasonable to believe that the composition of the LCMO targets change from the intended composition of $La_{0.67}Ca_{0.33}MnO_3$ to $La_{0.7}Ca_{0.3}MnO_3$ is purely due to differential thermal evapouration. Although this small variation of the composition does not affect our present work on LCMO films, any further LCMO target preparation should take this compositional change into consideration and make appropriate corrective measures. The crystalline structure of our LCMO targets was then characterized by XRD. Figure 5.1 shows the XRD pattern of the targets showing prominant and sharpe diffraction lines which are well matched by the XRD peaks of LCMO fine particles [Sanchez and Rivas, 1996] and XRD data of typical perovskites

oxides [Galasso, 1990]. Hence, the LCMO targets prepared were well crystallized and perovskite like oxides.

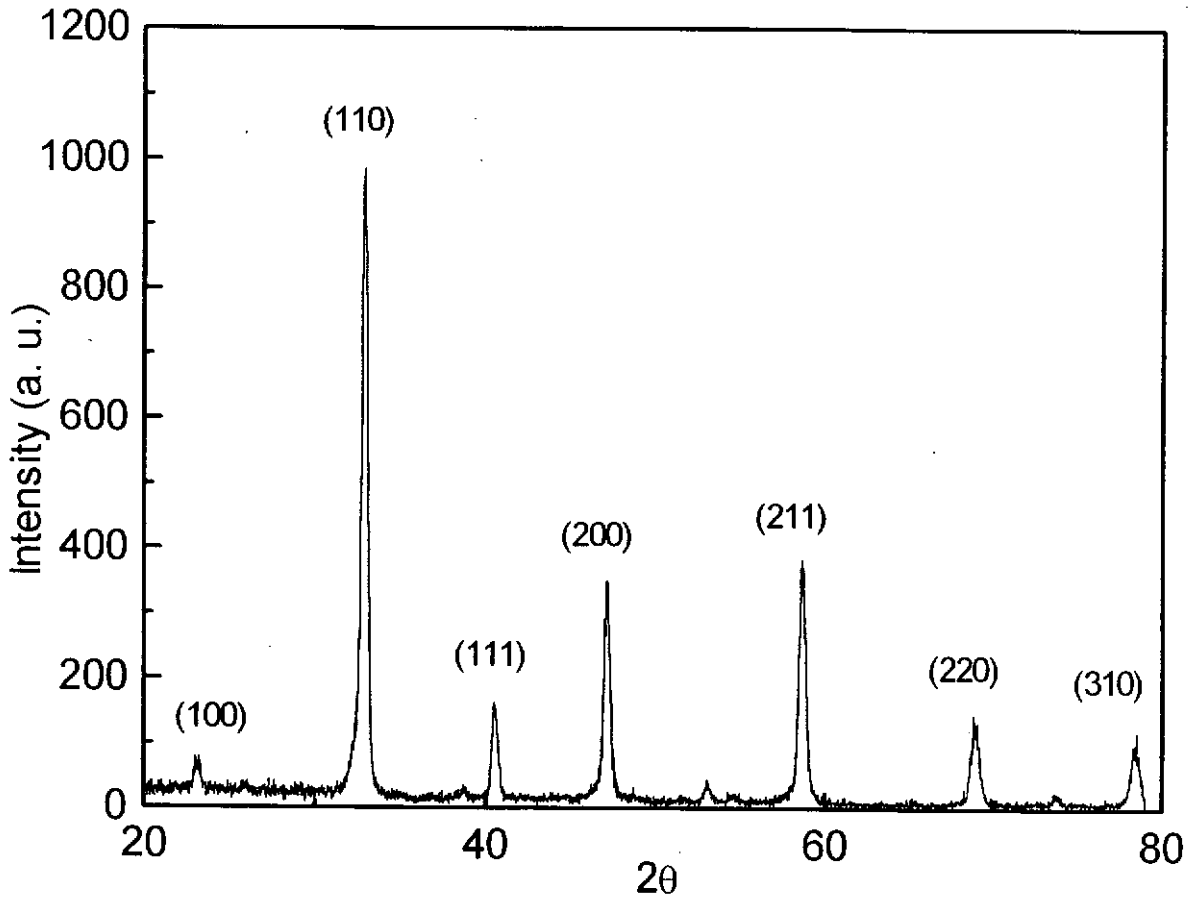

Figure 5.1 The XRD pattern of the LCMO perovskite oxide target.

5.2 Structural Analysis of $La_{0.7}Ca_{0.3}MnO_3$ Thin Films

5.2.1 Substrate Temperature Dependence

It is well known that the substrate temperatures during film growth has prominent effect on the crystal structures of the ceramic thin films [Gu, 1995]. The LCMO films thickness were ~200nm prepared under laser fluence of ~2J/cm^2 with repetition rate of 10Hz for 30 minutes throughout this chapter. The substrate temperature range used in the present study was 600°C - 750°C. Figure 5.2 shows the 2θ-θ scans of the films deposited at 600°C, 650°C and 750°C. Apart from films grown at 600°C, all as-deposited films were well crystallized. This is evident from the presence of the sharp and well defined diffraction peaks. Also from the figure, (*h*00) LCMO peaks can be seen clearly for films deposited at 650°C and 750°C. The diffraction peaks of (100)LCMO and (100)LAO overlap because the lattice mismatch between them is small (<3%). The diffraction peaks of (200)LCMO and (200)LAO are very close to each other but resolvable. The lattice constants of LCMO and LAO are 3.89Å and 3.79Å respectively. No trace of other LCMO reflections was observed. This suggest that highly oriented LCMO films can be obtained at temperature of 650°C or above. While films deposited at temperature of 600°C or below are largely amorphous as no sharp peaks are observed in the XRD pattern. The appearance of the small K_β peaks is the LAO substrates diffraction peaks due to the K_β line of the x-ray.

For the films deposited at 650°C or above, the good film crystalline orientation is also reflected from the rocking curve for the (200) LCMO reflections. Figure 5.3 is the rocking curve of (200) LCMO reflection for the as-deposited film

obtained at temperature of 650°C. The FWHM of the (200) diffraction peak profile is 1.2°. This again suggests that the crystal of the film is highly oriented. The FWHM values of the (200) diffraction peak profile of the films obtained at 700°C and 750°C are a little bit smaller than that of the 650°C at about 1.1°. These values suggest that the crystal orientation can be improved, though slightly, by increasing the substrate temperatures.

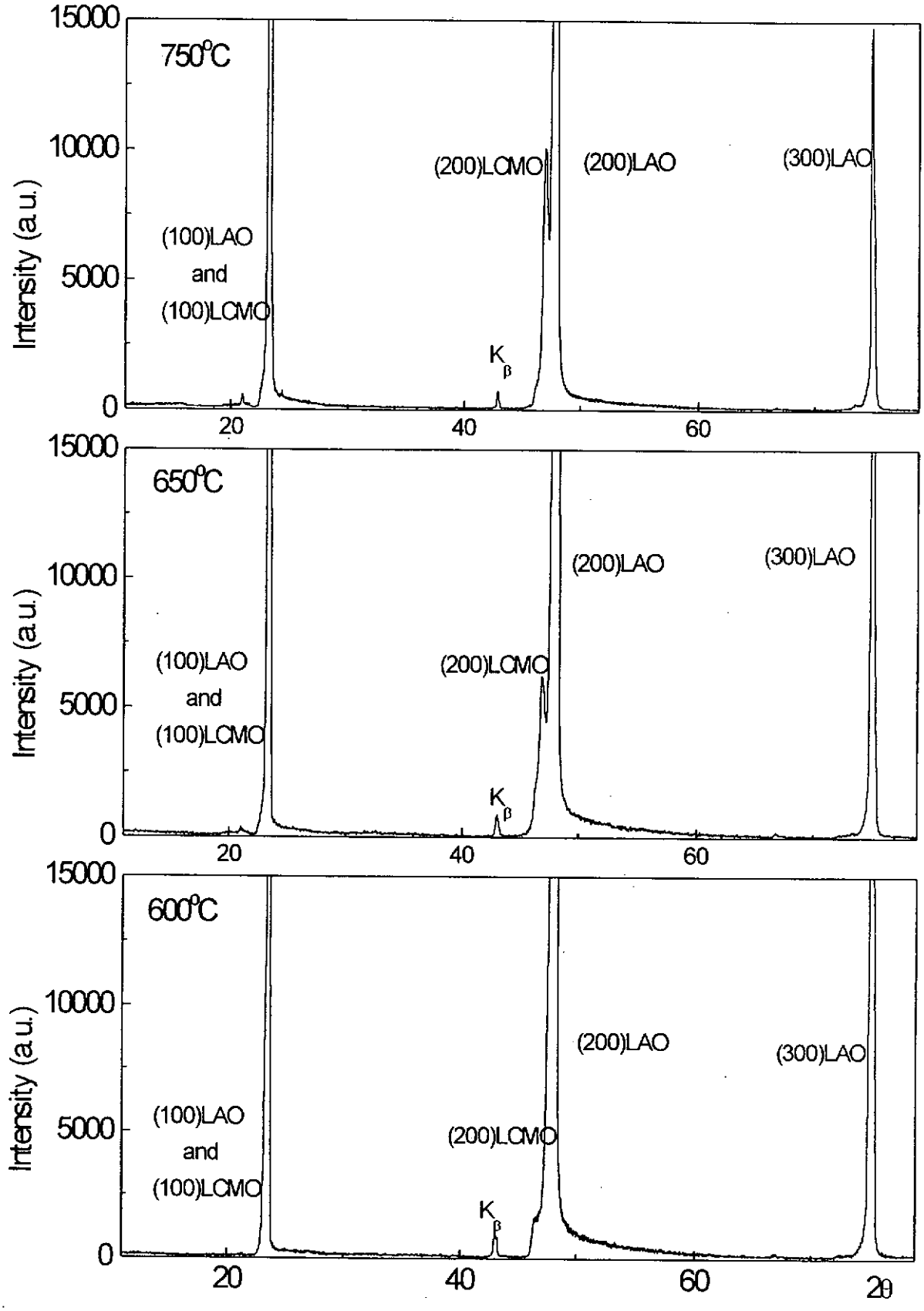

Figure 5.2 The X-ray diffraction pattern of the films deposited at 600°C, 650°C and 750°C respectively.

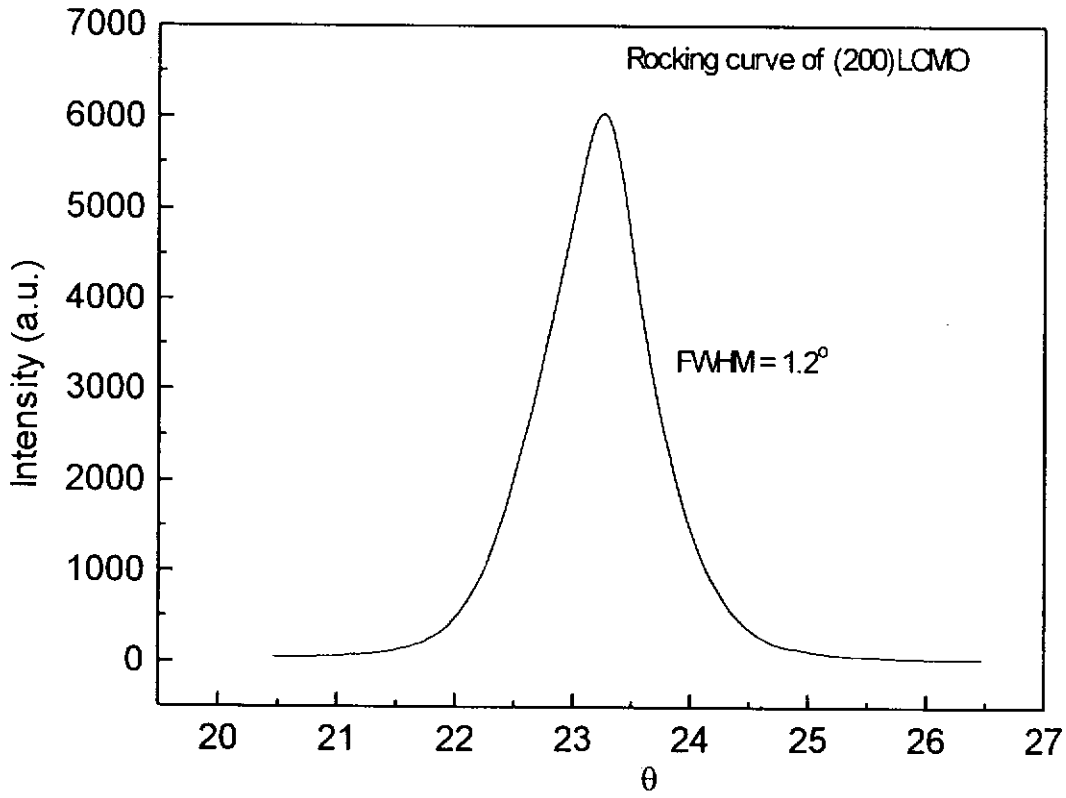

Figure 5.3 The rocking curve of (200)LCMO reflection of as-deposited LCMO film grown at 650°C. The FWHM is 1.2°.

The sharp and intense peaks in the normal θ-2θ scans and the value of FWHM in rocking curve give measures of the degree of orientation of the LCMO films crystals normal to the films surface only. In order to determine whether the films are epitaxially grown on the substrate, 360° ϕ-scans for the LCMO (220) and LAO (220) reflections were carried out. The ϕ-scans is used to confirm the in plane alignment of the films to the substrates. A film can be grown on a substrate in an excellent orientation to the normal of the surface, but poor in the in-plane orientation as twisting between planes can occurred.

Figure 5.4 shows the X-ray ϕ-scans of (220) LCMO and (220) LAO susbstrate reflections for the as-deposited thin films obtained at the temperature of 650°C. There are four sharp peaks for each of the scans. The four peaks are used to locate the orientation of the cubic lattice structures of the films and that of the substrates. From the figure, the four characteristics peaks of (220) LCMO reflections are very sharp and their ϕ angles match with those of the (220) LAO reflections. This clearly suggests that the LCMO films are epitaxially grown on the (100) LAO substrates. For films deposited at higher temperatures, similar results are obtained.

In short, our results indicate that the threshold temperature for obtaining highly oriented and epitaxial LCMO thin films on (100) LAO substrates by PLD method is only 650°C.

5.2.2 Post Deposition Annealing Effects

Results from our present study have also shown that the post deposition annealing can improve the crystallinity of the crystal structures of the LCMO thin films. When the as-deposited LCMO thin films obtained at 650°C were post annealed under 1 atm oxygen pressure at the same deposition temperature for one hour, the crystallinity of the thin films were improved. The FWHM of the (200) LCMO reflection reduced from 1.2° to 0.9°. The post deposition annealing process provides more energy to annealed out the defects and sufficient time to let the crystals re-orient in the proper positions. Hence, the post deposition annealing process is effective in improving the crystallinities of the LCMO thin films.

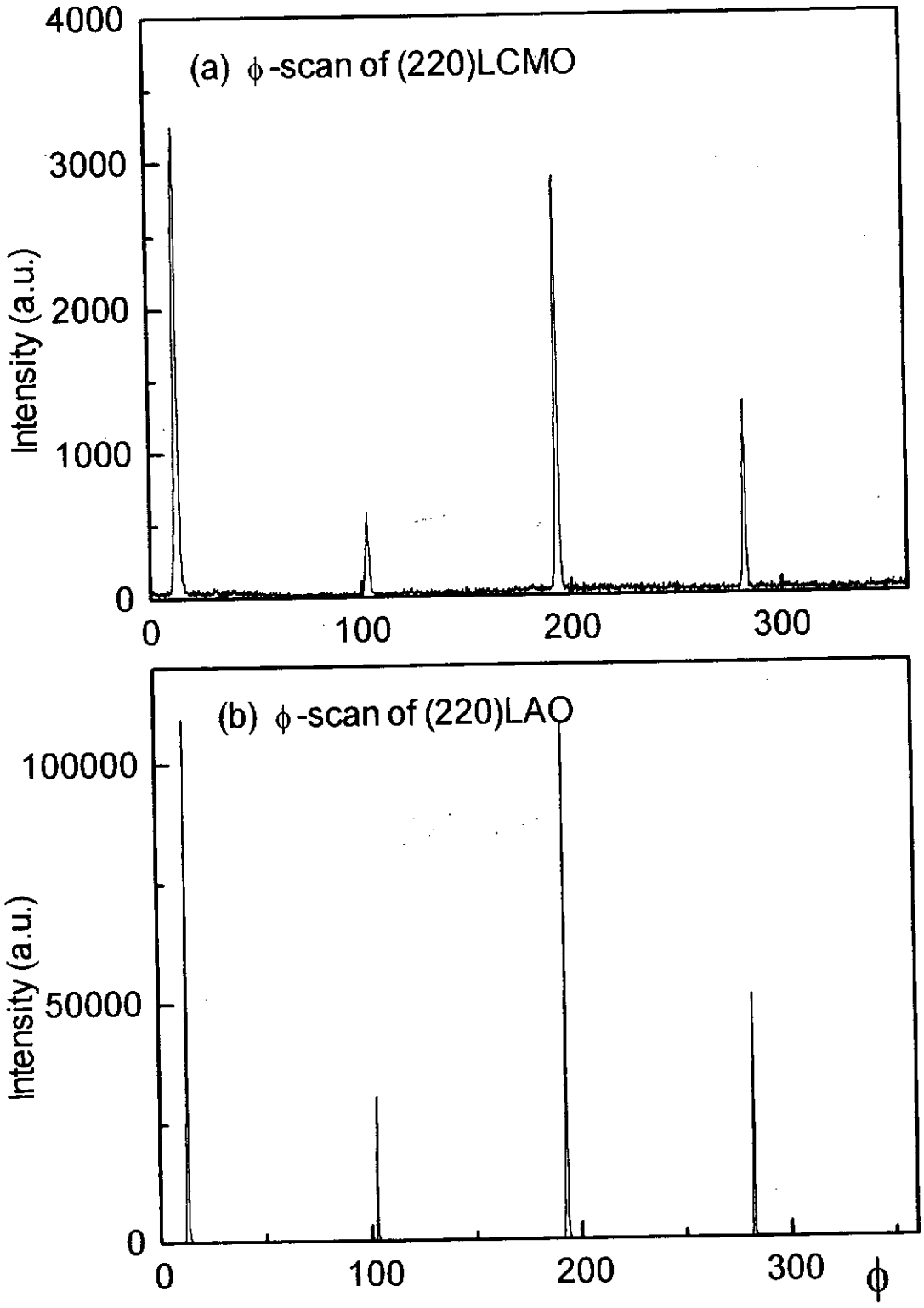

Figure 5.4 The X-ray ϕ-scan of the (220) reflections of (a) LCMO film and (b) LAO substrate.

5.3 Electrical Properties of $La_{0.7}Ca_{0.3}MnO_3$ Thin Films

5.3.1 Substrate Temperature Dependence

The deposition substrate temperature has distinct effect on the electrical properties of the LCMO thin films. Figure 5.5 shows the R-T curves of the as-deposited LCMO thin films at substrate temperatures of 600°C (curve A), 650°C (curve B), 700°C (curve D) and 750°C (curve C). The values of peak resistivity of the films are normalized for ease of comparison. The Curie temperature, T_c, for the films deposited at the substrate temperatures of 600°C, 650°C, 700°C and 750°C are 113K, 123K, 190K and 178K, respectively. In the substrate temperature range of 600°C - 700°C, the value of T_c increased with the increasing of the substrate temperatures. This trend is probably due to the improved crystallinity of the LCMO thin films at higher deposition temperatures. At substrate of 750°C, however the value of T_c is 178K, which is lower than that of the sample prepared at 700°C. This reversal of trend of T_c dependence is caused by oxygen deficiency of the films deposited at high substrate temperatures [Zhang and Boyd, 1996]. Indeed, oxygen deficient and lowering of T_c have been observed by Zhang and Boyd in LCMO films deposited at the temperature range of 700°C - 900°C. Our results thus suggest that the highest T_c of the $La_{0.7}Ca_{0.3}MnO_3$ films is obtained at about 700°C.

Apart from the T_c values, the resistivity of the LCMO thin films is also affected by the deposition temperatures. Figure 5.6 shows the dependence of the peak resistivity of the LCMO samples on the substrate temperature. It is seen that the peak resistivity of the LCMO thin films decrease initially with increasing deposition temperatures and become more or less a constant at about 700°C. These observation

is different from those reported by Zhang and Boyd [Zhang and Boyd, 1996], in which their LCMO films grown at a relatively higher substrate temperature of ~ 900°C showed the opposite trend. They attributed the effect being caused by oxygen deficiency in the LCMO films. Apparently oxygen depletion due to high deposition temperatures is not occurred in our samples prepared at 600°C - 700°C. A resistivity of ~ 1050mΩ.cm is obtained in the as-deposited $La_{0.7}Ca_{0.3}MnO_3$ films prepared at 700°C.

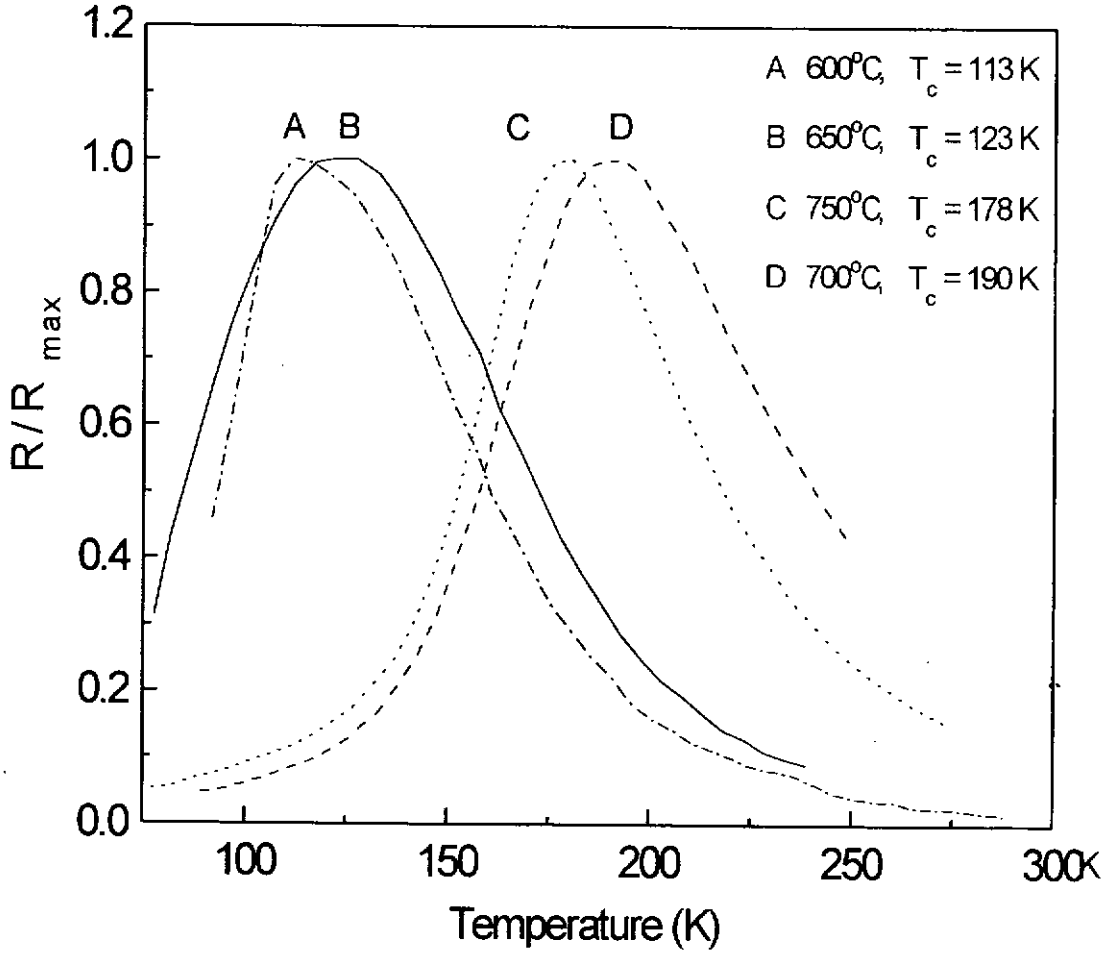

Figure 5.5 The normalized R-T curves of as-deposited LCMO films grown at 600°C (curve A), 650°C (curve B), 700°C (curve D) and 750°C (curve C).

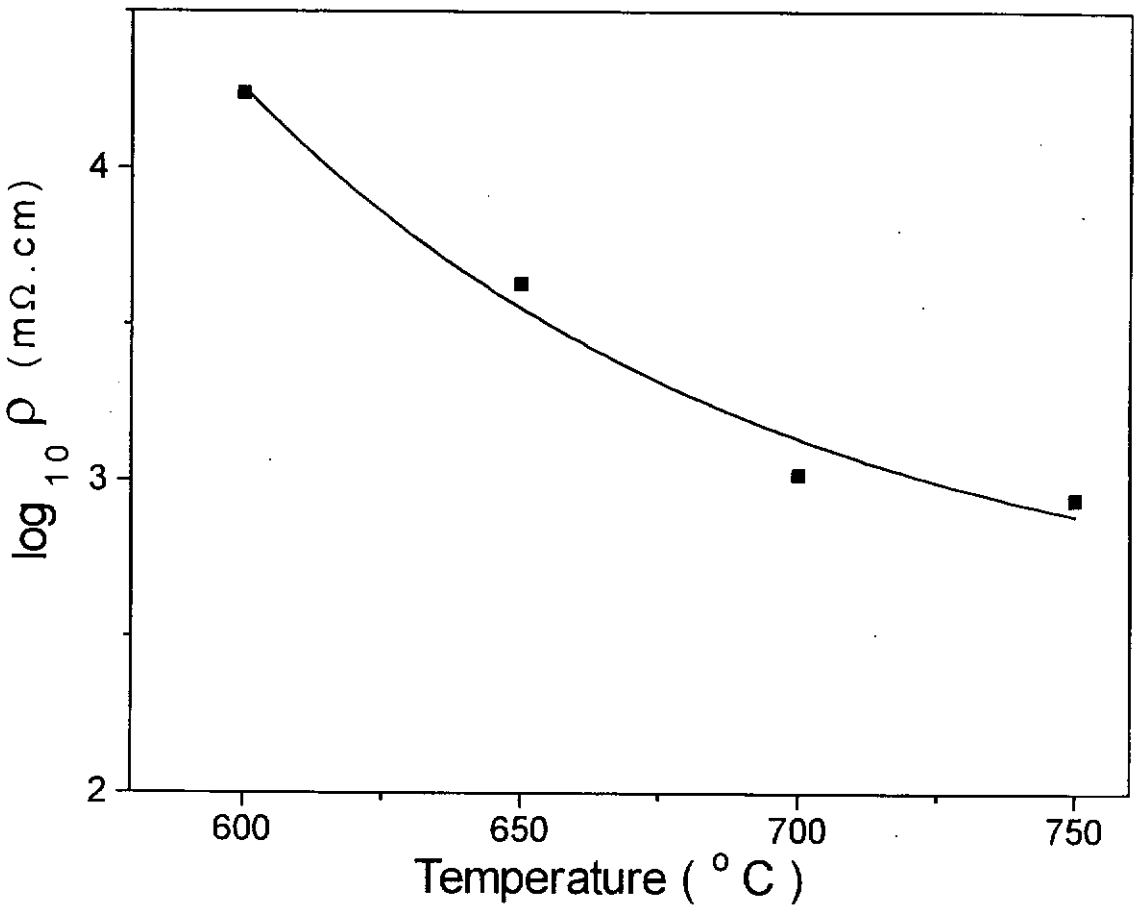

Figure 5.6 The peak resistivities of the LCMO films as a function of substrate temperatures; ■ are the data points of the as-deposited films. The solid curve is drawn for viewing purpose.

5.3.2 Post Deposition Annealing Effects

The process of post deposition annealing has marked effects on the conductivity and T_c of the LCMO thin fims. In this study, the post deposition annealing process was carried out in situ immediately after deposition and at the same substrate temperature under 1 atm oxygen pressure for one hour. Figure 5.7 shows R-T curves of the LCMO thin films fabricated at 650°C and 700°C at conditions with and without post-annealing. The values of resistivity of the films are normalized for ease of comparison. It is seen from this figure that the post deposition annealing process raises the T_c further by about 20K in both cases (143K and 214K for 650°C and 700°C, respectively). It is believed that the increase of the oxygen content and the improvement of crystallinity of the LCMO thin films during the post deposition annealing process are the major causes.

It is also noted that the post deposition annealing process can greatly improve the conductivity of the LCMO thin films. Figure 5.8 shows the R-T curves of the as-deposited and post-annealed LCMO thin films under the processing temperature of 650°C. From the figure, it can be seen clearly that the whole profile of the R-T curve is substantially lowered after the post annealing. The peak resistivities are marked in the figure and are 4230mΩ.cm and 330mΩ.cm for the as-deposited and the post-annealed films respectively.

Figure 5.9 shows the peak resistivities of the LCMO films as a function of processing temperatures. The squares (■) and the triangles (▲) represent data points of the as-deposited and post-annealed films. Post-annealing has, in general, the effect

of reducing the resistance of the films. The most noticeable change, however, occurs in films deposited at 650^0C, in which the films' resistance dropped by more than an order of magnitude from 4230 mΩ.cm to 330 mΩ.cm after annealing at 650^0C for one hour. It is important to note that for the annealed films, the resistance remained more or less the same at about 300 mΩ.cm for deposition temperatures of 650^0C, 700^0C and 750^0C. The marked change of resistance for films annealed at 650^0C may imply that the single phase perovskite LCMO formation starts at such temperature. Annealing can thus promote the growth of the highly conducting perovskite LCMO films and a sudden drop in the film's resistance results. Higher annealing temperature, however, only improves the crystallinity of the already conducting LCMO films and has a minor effect on lowering the film resistance.

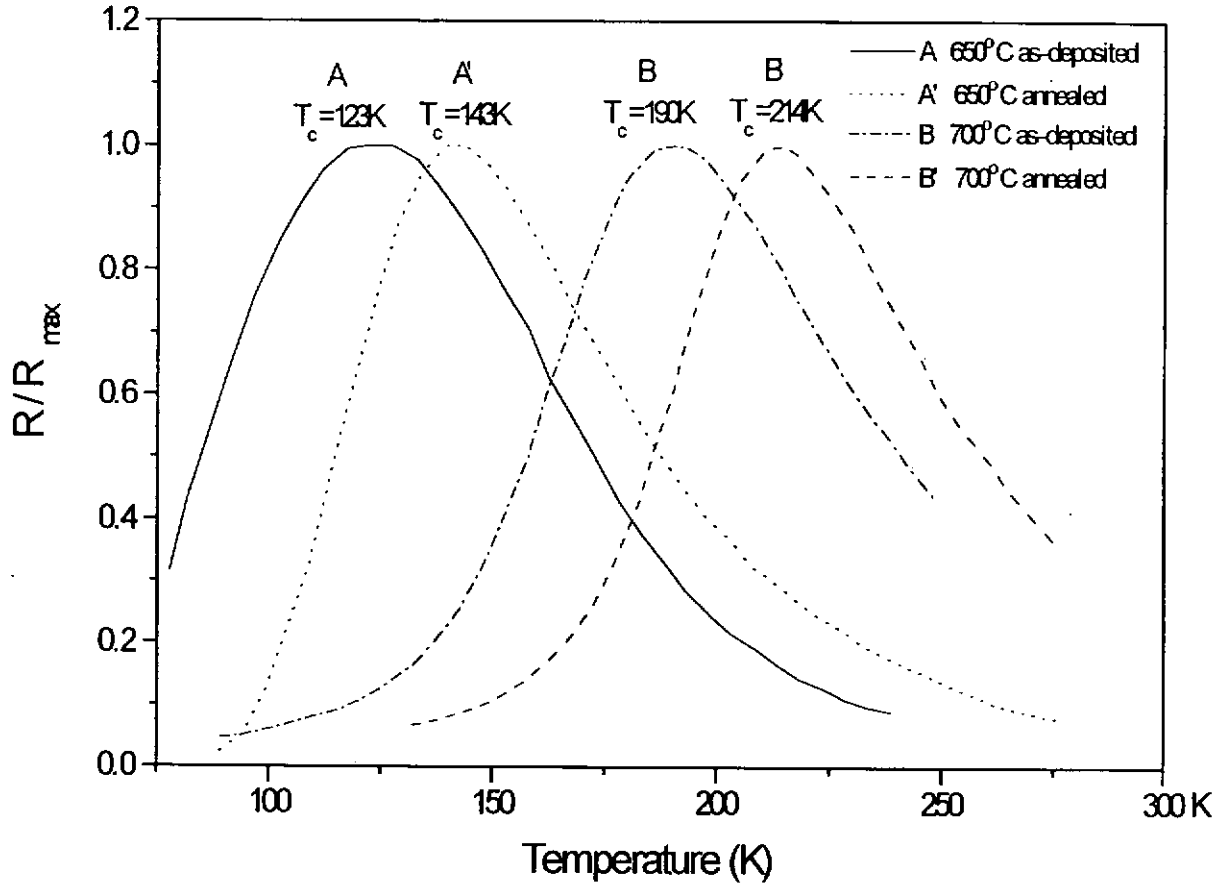

Figure 5.7 The normalized R-T curves of LCMO as-deposited films A(650°C), B(700°C) and post-annealed films A'(650°C), B'(700°C).

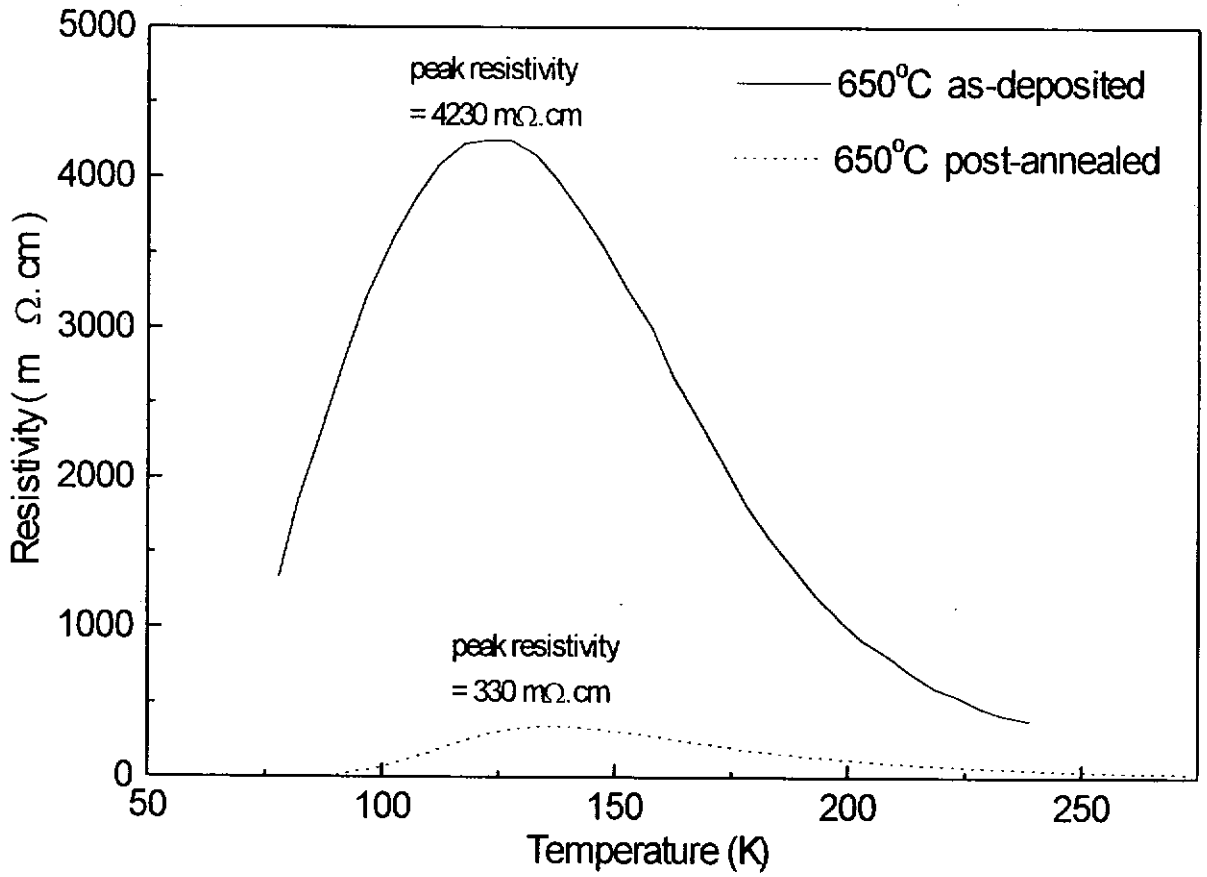

Figure 5.8 The R-T curves of as-deposited and post-annealed LCMO thin films grown at 650°C.

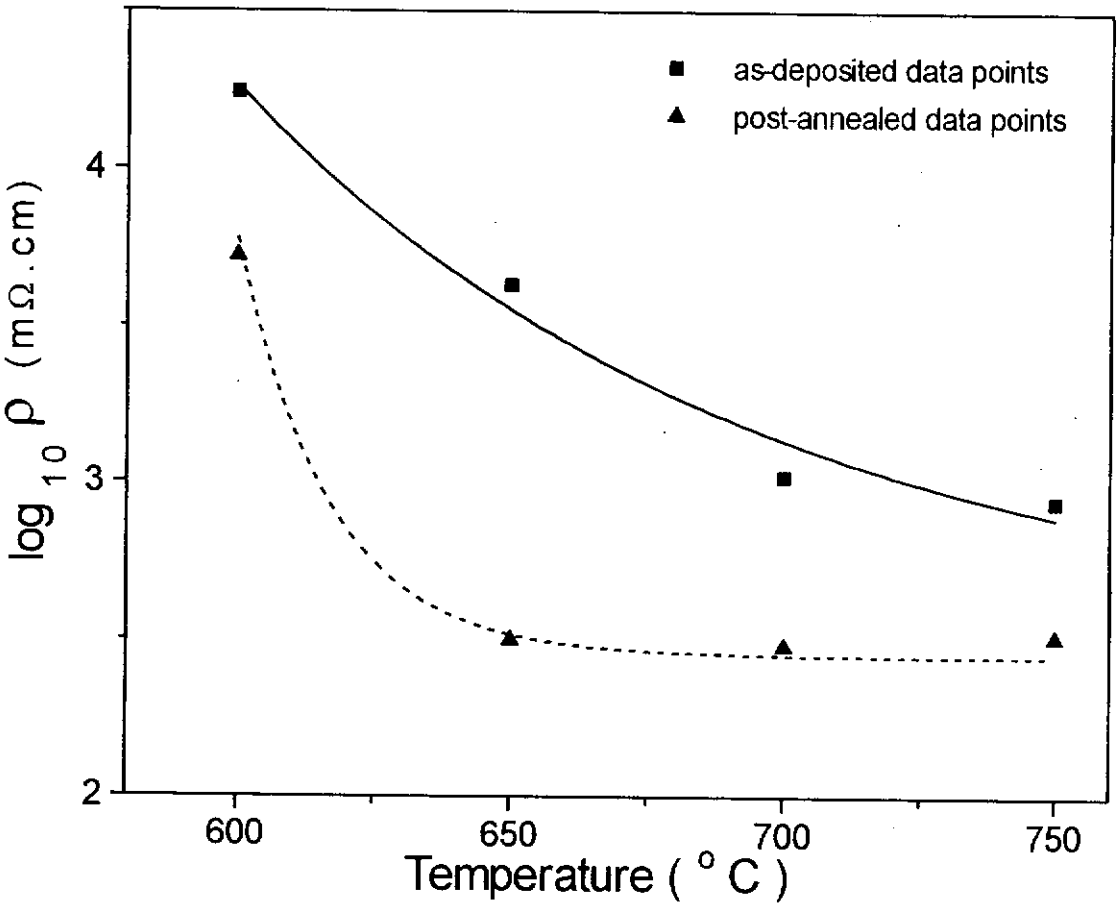

Figure 5.9 The peak resistivities of the LCMO films as a function of processing temperatures; ■ are the as-deposited films and ▲ are the post-annealed films. The solid and dash curves are drawn for viewing purpose.

5.4 Magnetic Properties of $La_{0.7}Ca_{0.3}MnO_3$ Thin Films

5.4.1 Magnetic Field Dependence

When the LCMO films are placed under an applied constant B-field parallel to the current direction and the film's surface, the resistance of the films is reduced. The amount of reduction depends on the magnitude of the B-field. Figure 5.10 and figure 5.11 show the B-field dependence of R-T curves for the LCMO films deposited and post-annealed at temperatures of 650°C and 700°C. From both figures, we can see that the film resistance is suppressed by the application of a B-field. There are some changes on the T_c values of the LCMO films under different values of B-field. For films fabricated at 650°C, the value of T_c is shifted from 143K at B=0T to 148K at B=1T. For films fabricated at 700°C, the value of T_c is shifted from 214K at B=0T to 224K at B=1T. These observations have clearly demonstrate that the absolute resistivity and the T_c strongly depend on the magnitude of the external applied magnetic field, and LCMO is a good magnetoresistive materials. By increasing the magnitude of the external applied B-field, the resistivities are lowered and the positions of T_c are are up shifted to higher temperatures. The resistance change can be well explained by the Zener's Double Exchange (DE) Interaction discussed in Chapter 3. The conduction process of the electrons in the perovskite oxides can be improved if the surrounding magnetic ions were aligned ferromagnetically. The shifting of the T_c is due to the restraint of the semiconductor to metal transition under high magnetic field.

The values of MR also varies with the applied B-field. Figure 5.12 and figure 5.13 show the field dependence of the MR% of the LCMO films deposited and post-

annealed at the temperature of 650°C and 700°C. For the LCMO films processed at temperature of 650°C (figure 5.12), the maximum MR% of the films under a B-field of 0.5T and 1T are 20% and 37% respectively. While for the LCMO films processed at temperature of 700°C (figure 5.13), the maximum MR% of the films is 22% at 0.5T and 39% at 1T. The negative signs come from the fact of decreased resistivity under an applied B-field.

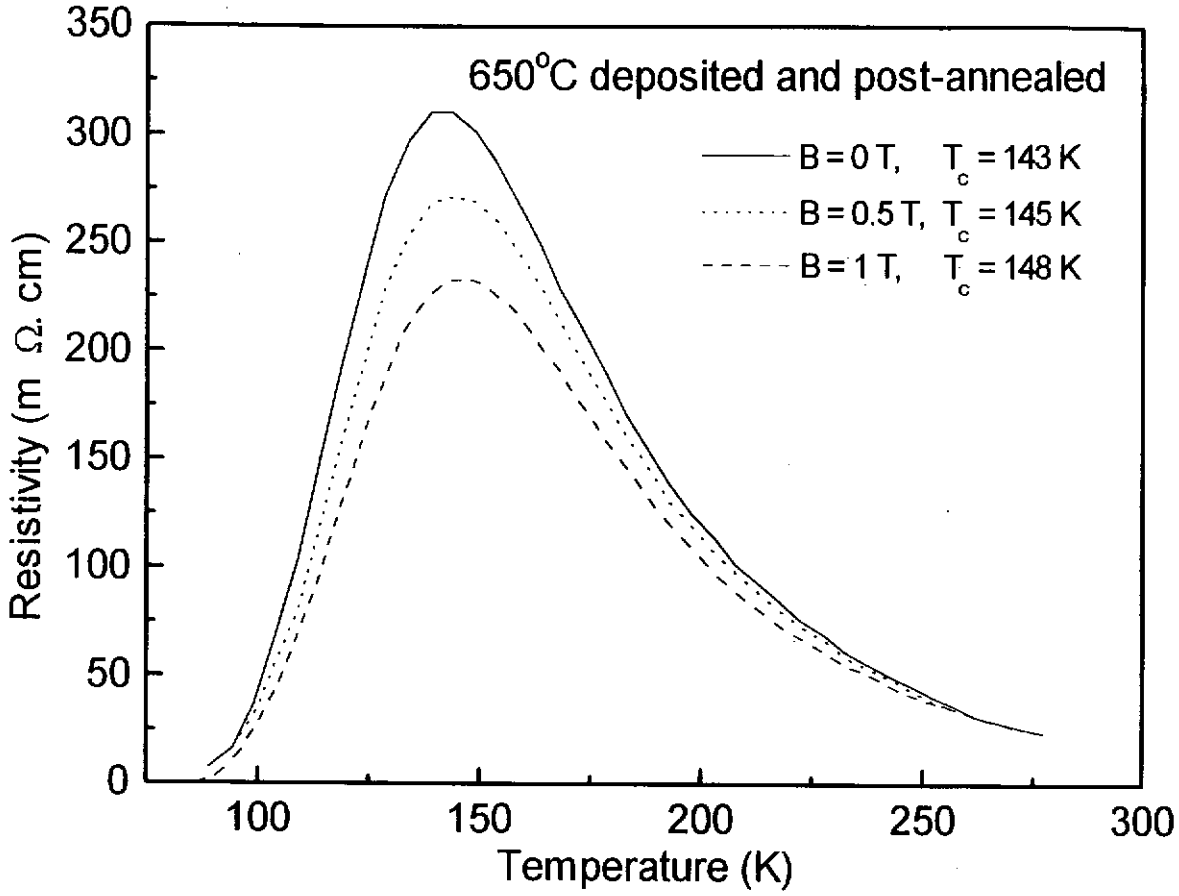

Figure 5.10 The B-field dependence of the R-T curves for LCMO film deposited and post-annealed at 650°C.

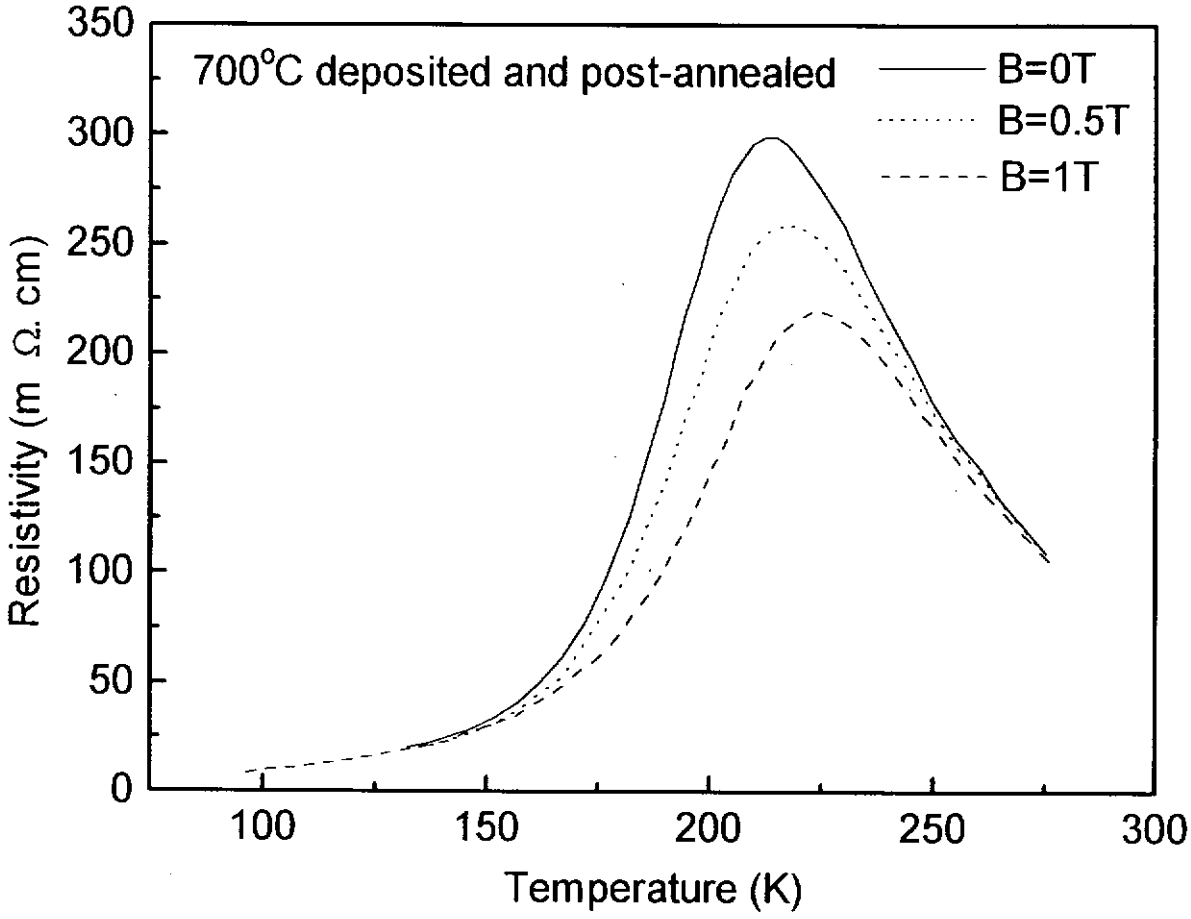

Figure 5.11 The B-field dependence of the R-T curves for LCMO film deposited and post-annealed at 700°C.

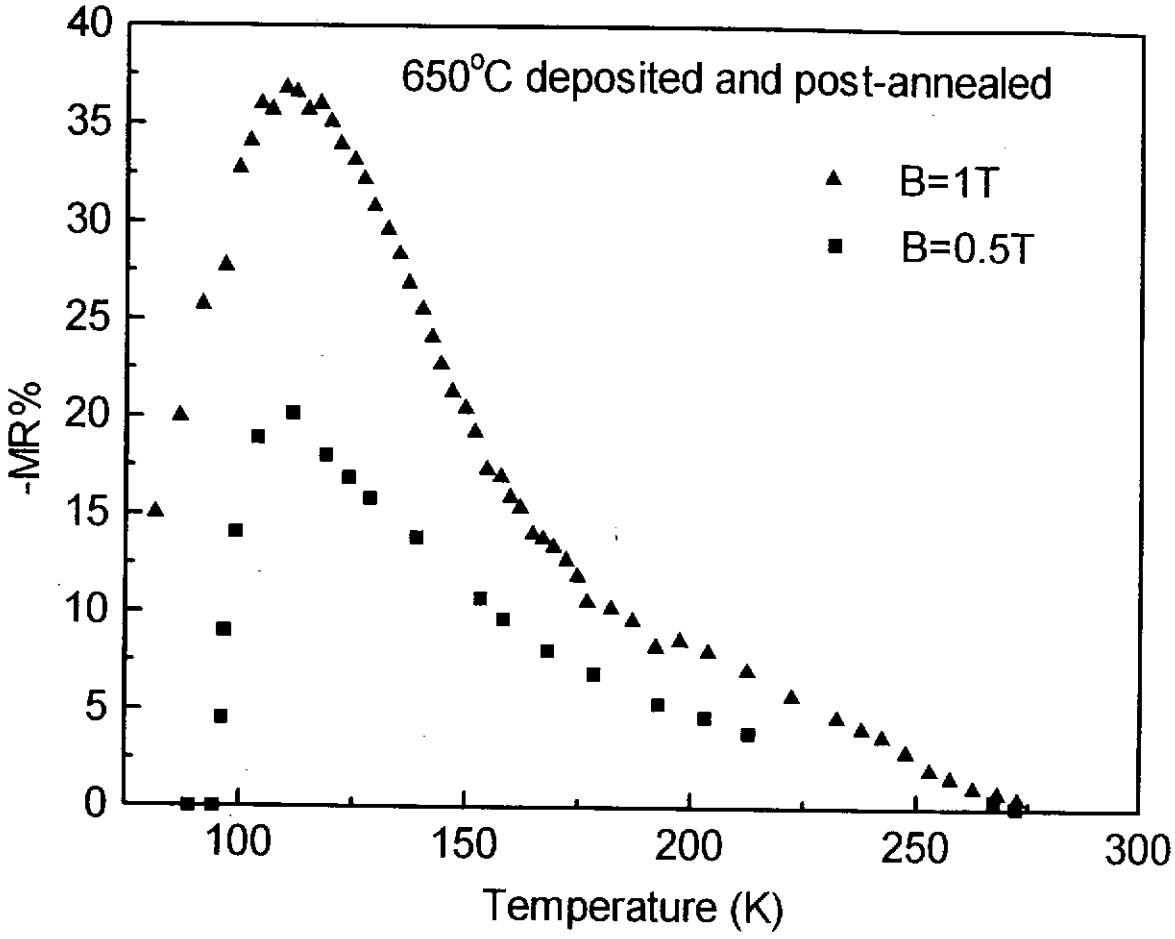

Figure 5.12 The field dependence of the MR% for the LCMO film deposited and post-annealed at temperature of 650°C.

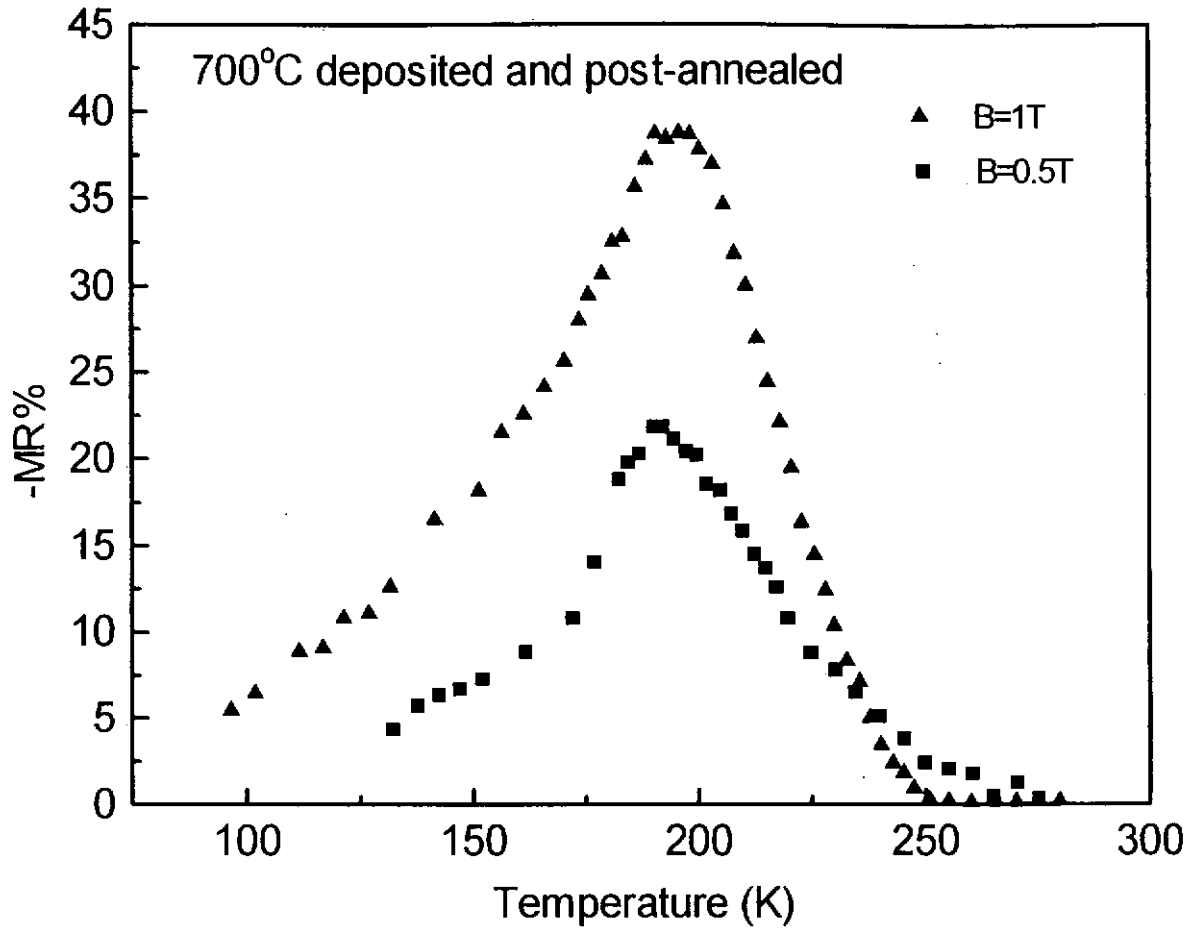

Figure 5.13 The field dependence of the MR% for the LCMO film deposited and post-annealed at temperature of 700°C.

5.4.2 Processing Temperatures Dependence

The processing temperatures strongly affect the magnetic properties of the LCMO thin films. Different processing temperatures result in different magnitude of MR and the peak MR temperature. Figure 5.14, figure 5.15 and figure 5.16 show the R-T curves and MR profile of the LCMO films prepared at the processing temperatures of 650°C, 700°C and 750°C, respectively. The films were all post annealed in conditions described previously. From the three figures, the highest value of MR is obtained near T_c, where an applied magnetic field induces the highest change of the magnetization, i.e. the effect of the magnetic field on the disordered electrons spins is highest.

Table 5.1 tabulated MR changes of the LCMO films under different processing temperatures.

Processing temperature	Maximum MR%	Peak MR% temperature
650°C	37%	110K
700°C	39%	195K
750°C	49%	135K

Table 5.1 Processing temperature dependence and the MR changes of the LCMO films.

From the table, the maximum MR% changes of the LCMO films are seen to increase with the processing temperatures. A maximum MR% of 49% (B=1T) is obtained at processing temperature of 750°C. The highest peak MR% change temperature of 195K is obtained for the films prepared at temperature of 700°C.

The three MR profiles for 650°C, 700°C and 750°C are plotted in figure 5.17. It can be seen that the shifting of the MR profile and the absolute MR% change depends strongly on the processing temperatures. The shifting of the MR profiles to lower temperature for the film deposited at 750°C is possibly due to the oxygen deficiency in the LCMO films.

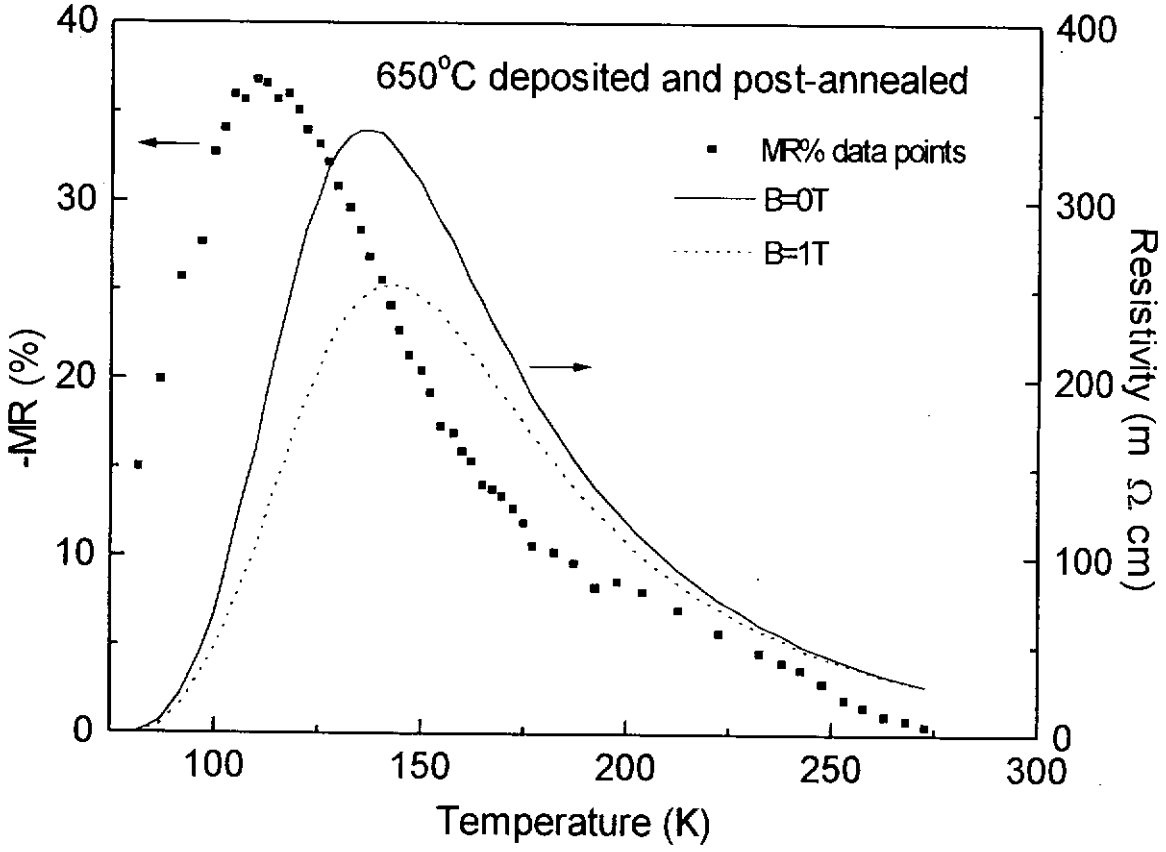

Figure 5.14 The R-T curves and MR profile of the LCMO film deposited and post-annealed at the temperature of 650°C.

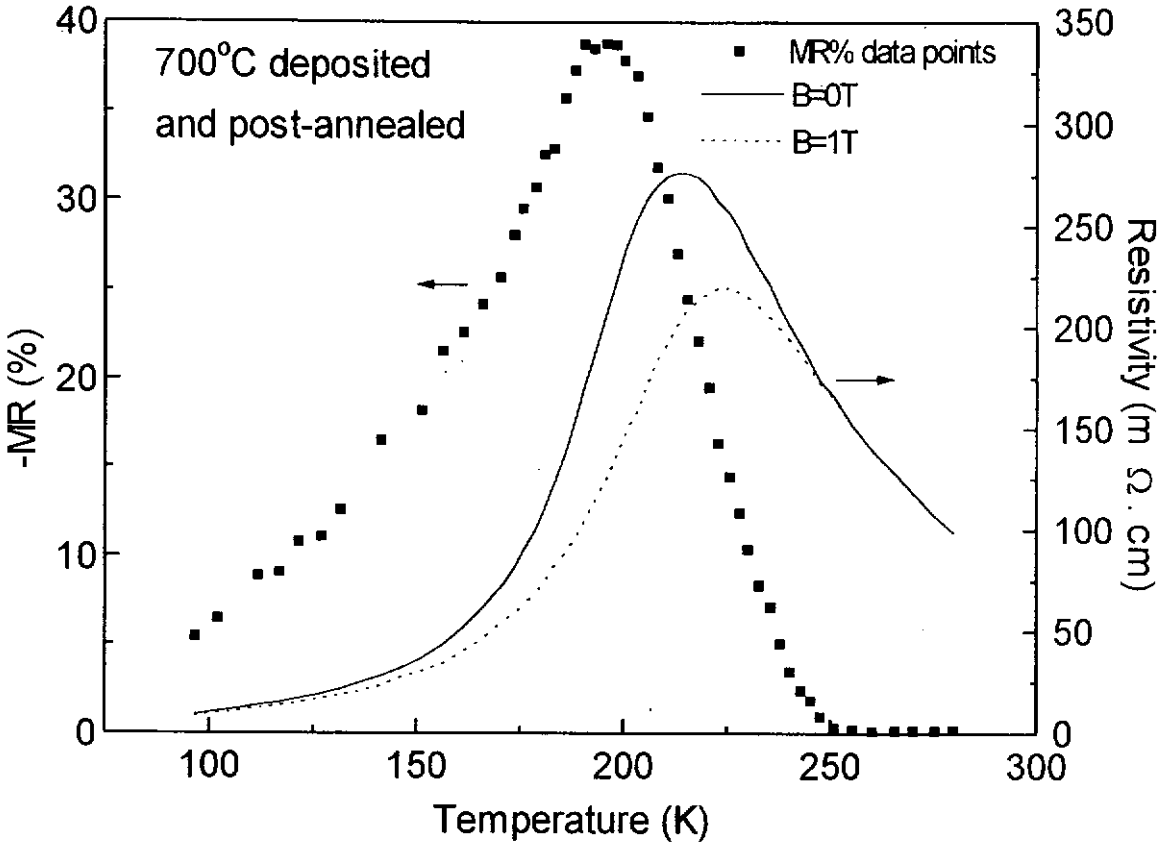

Figure 5.15 The R-T curves and MR profile of the LCMO film deposited and post-annealed at the temperature of 700°C.

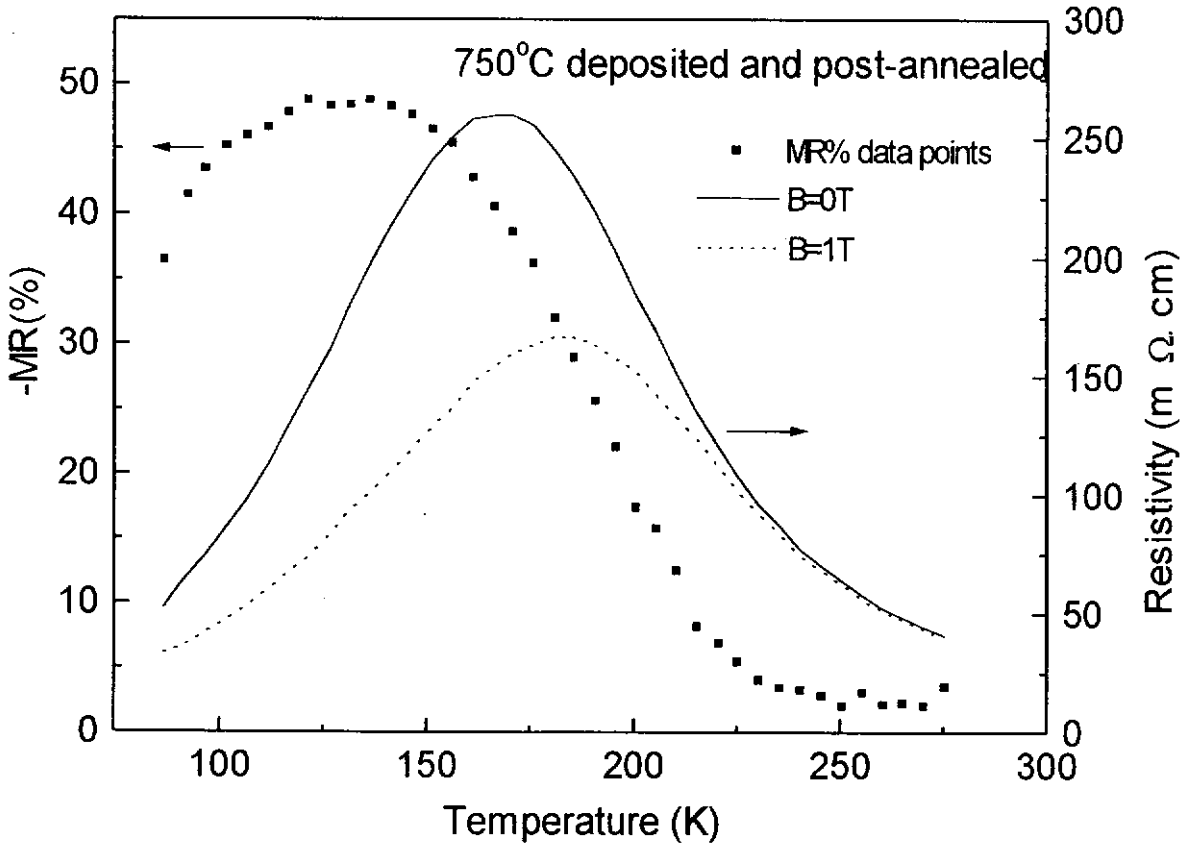

Figure 5.16 The R-T curves and MR profile of the LCMO film deposited and post-annealed at the temperature of 750°C.

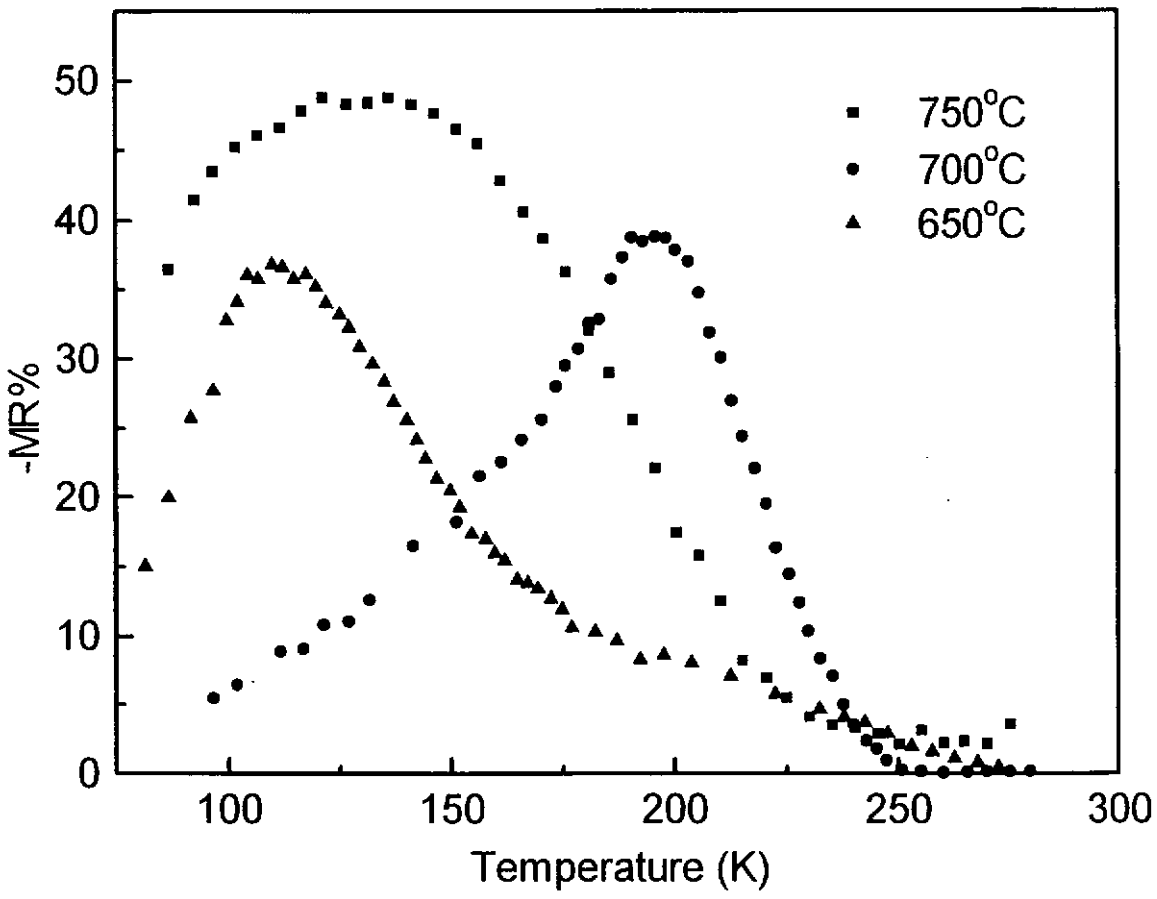

Figure 5.17 The MR profiles of the LCMO films deposited and post-annealed at temperatures of 650°C, 700°C and 750°C.

Chapter 6

Fabrication and Characterization of LCMO Heterostructures

6.1 Introduction

In chapter 5 we have discussed the structural, electrical and magnetic properties of a single layer LCMO thin film deposited on single crystal (100)LAO substrate. Excellent quality of giant magnetoresistive LCMO thin films have been prepared. In practice, however, it will be very useful if the oxide films can be grown on silicon substrates. The properties of the oxides can thus be combined with the present microelectronics technology to create new functional integrated devices. In this chapter we will discuss the fabrication of epitaxial LCMO thin films on Si substrates. The LCMO films were grown directly on Si substrates initially and indirectly through buffer layers of Titanium Nitride (TiN) and Strontium Titanium Oxide (STO) in subsequent experiments. Discussions and comparisons of the structural and transport properties of the heterostructures LCMO/Si, TiN/Si, LCMO/TiN/Si, STO/TiN/Si and LCMO/STO/TiN/Si will be presented. Figure 6.1 shows the flow chart of the sequence of the fabrication of LCMO based heterostructures.

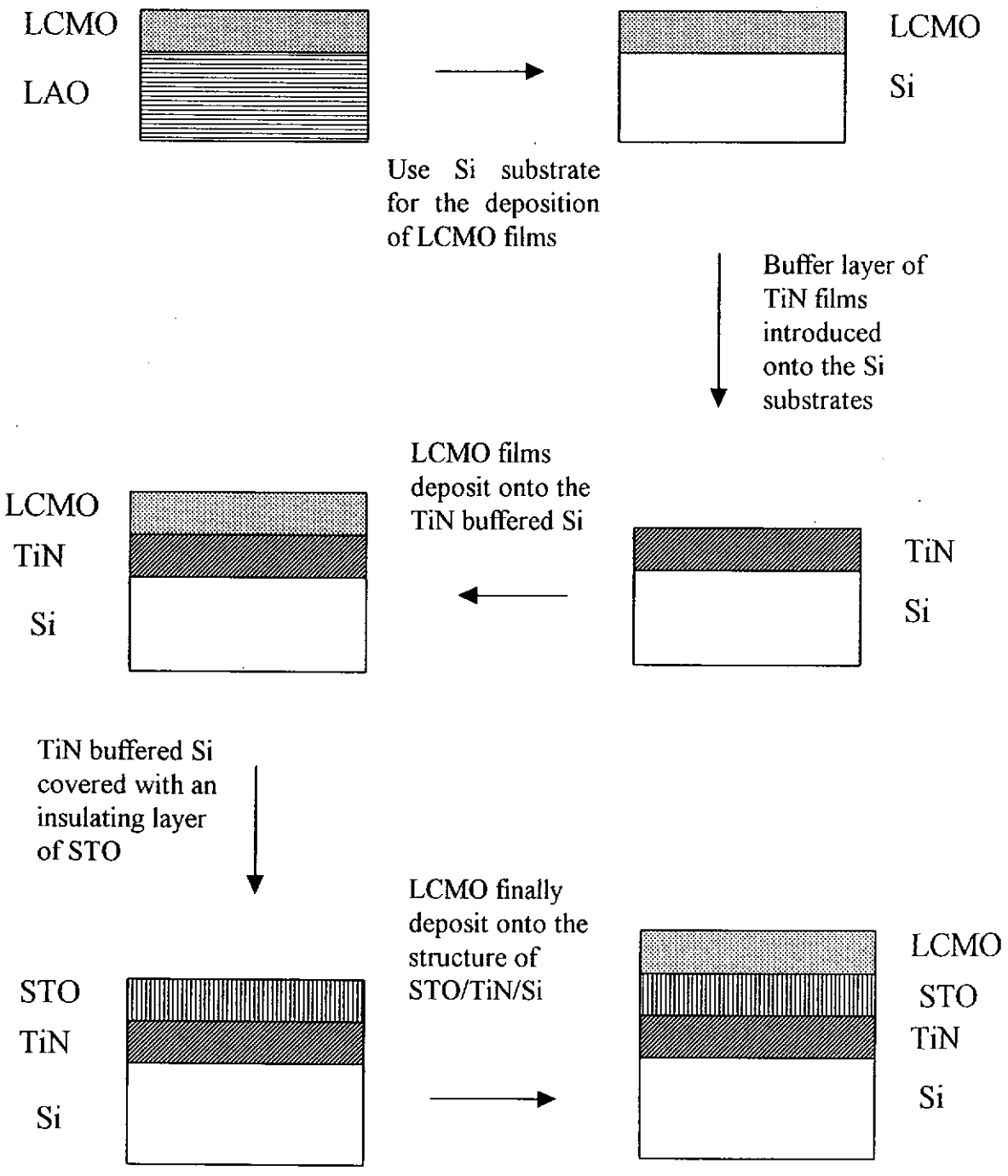

Figure 6.1 The flow chart of LCMO based heterostructures fabrication.

6.2 Characterization of LCMO/Si

LCMO films deposited directly on (100)Si substrates have been reported by Zhang and Boyd [Zhang and Boyd, 1996], in which the LCMO films were grown at 900°C by PLD method. Multiphase films with relatively low MR (32% at 5.7K with B=4.7T) were obtained. The obvious reasons for resulting such rather poor quality films are that the LCMO and Si have large lattice mismatch (a = 5.43Å for (100)Si and a = 3.89Å for (100)LCMO) and that elevated substrate temperature of 900°C may cause severe oxygen defieiency in the LCMO films as well as interfacial diffusion into the Si substrates. We therefore argue that for successful epitaxial LCMO films grown on Si substrate, a buffer layer sandwiched in between LCMO and Si is essential. The buffer layer needs to be chemically stable and resistive to thermal diffusion, epitaxial grown on Si and yet providing lattice matching environment for the subsequent LCMO epitaxial growth.

It has been established that TiN is an excellent material as buffer layer for Si substrates [Narayan, 1992; Meng, 1995; Chowdhury, 1993; Vispute, 1994; Tiwari, 1994; Lee, 1995]. It is widely used in semiconductor industry to provide good Ohmic contact and to protect the Si substrates from being oxidized. High quality epitaxial TiN films have been grown on Si substrates by various film growth techniques. In depositing LCMO it is believed that the use of a nonoxide buffer layer can protect the Si surface from being oxidized during the oxides films growth. Also the chemical stability and diffusion barrier properties [Toth, 1971] of TiN are well known and expected to prevent reaction and interdiffusion between the oxides and Si.

LCMO films with film thickness of ~200nm were prepared under laser fluence of 3J/cm^2 with repetition rate 10Hz for 30 minutes. This value of thickness applied to all of the LCMO films prepared later on. Figure 6.2 shows the XRD pattern of as-deposited LCMO films on Si substrates prepared under an ambient oxygen pressure of 200mTorr and at substrate temperature of 700°C. From the figure, it can be seen that the LCMO films are polycrystalline with multiple phases. The diffraction pattern is very much like the diffraction pattern of LCMO target as shown in figure 5.1. It is evident that the LCMO films cannot be grown epitaxially on Si substrates. Our results are thus in broad agreement with those reported by Zhang and Boyd.

Figure 6.3 shows the R-T curve of LCMO films deposited on (100) Si substrate. The resistance of the films is relatively large. The samples are semiconducting and exhibit no semiconductor-metal transition in the temperature range studied. T_c is possibly at well below 77K (liquid nitrogen temperature). No measurable MR% for LCMO prepared on Si substrates.

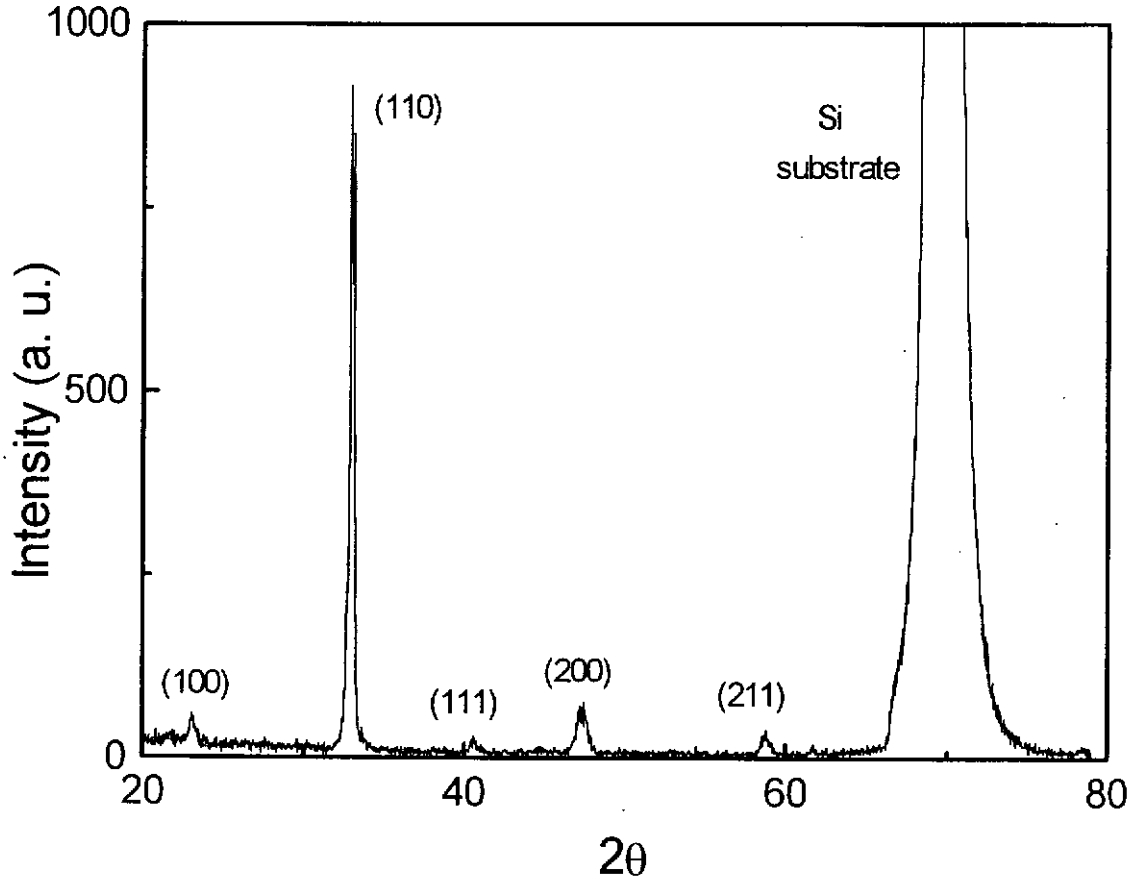

Figure 6.2 The XRD pattern of LCMO films deposited on (100) Si substrates.

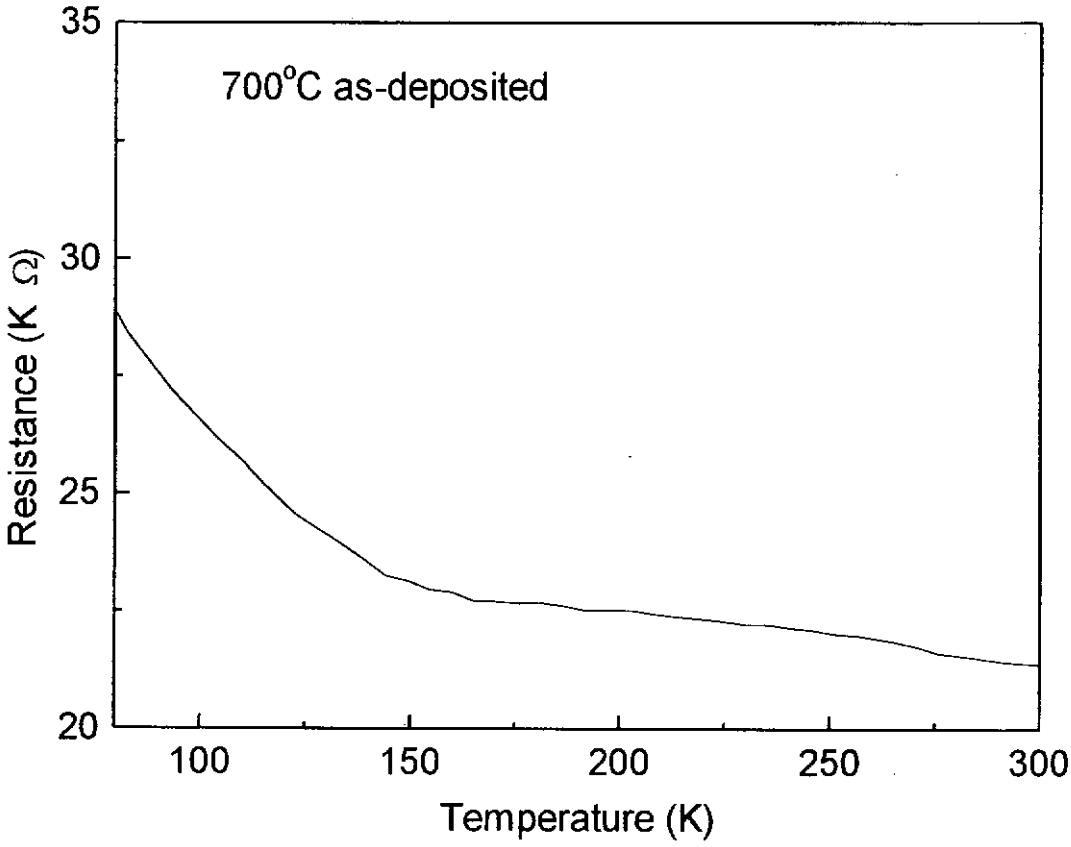

Figure 6.3 The R-T curve of the LCMO films deposited on (100)Si substrate.

6.3 Characterization of TiN/Si and LCMO/TiN/Si

6.3.1 TiN/Si

TiN films can be obtained by two different approaches. One is to ablate a Ti metal target under ambient nitrogen and the other is to ablate a TiN target directly. It has been found that high quality TiN films are difficult to obtained by the first method. This is probably due to the fact that N_2 is a relative stable molecule and it is not so ready to react to form nitride under the typical PLD conditions. As a result only a small proportion of TiN is obtained in the film. Furthermore the freshly deposited Ti metal can be easily oxidised by the impurities in the N_2 gas (purity 99.995%). If a more reactive gas such as ammonia was used, the yield of TiN and hence the quality of the TiN films, perharps could be improved. The other method of depositing TiN by ablating a TiN target directly is more successful and we adopted this approach in all our work on preparation of TiN films. The TiN targets were bought from Electronic Space Products International (ESPI) company (grade 2N5). Figure 6.4 shows the XRD pattern of TiN target. To deposit TiN films, high vacuum (~ 10^{-6} Torr) is an essential condition as oxidation of TiN layer occurred readily at 1 mTorr O_2 [Vispute, 1996]. TiN films with film thickness ~100nm were prepared under laser fluence of 4.5J/cm^2 with repetition rate 10Hz for 30 minutes. This value of thickness applied to all of the TiN films prepared later on. Epitaxial TiN films were obtained in a wide range of substrate temperatures from 500°C to 700°C. Table 6.1 tabulates the deposition conditions and the quality of the corresponding TiN films. The FWHM was measured from the rocking curves of the (200)TiN reflection. From the table, we can see that the crystallinity of the TiN films increases with the substrate

temperature. The resisivities of the TiN films were more or less equal to 70μΩ.cm. This value suggest that the TiN films are highly conductive. The typical resistivity and crystallinity (reflected by the FWHM in rocking curve) is ~40μΩ.cm and ~1° respectively [Lee et al., 1994]. Our results show that the resistivity and crystallinity is ~70μΩ.cm and ~1.4° and it is comparable to those reported.

Substrate temperature (°C)	Pressure (Torr)	FWHM of (200) TiN
500	6×10^{-6}	2.16°
600	6×10^{-6}	1.81°
700	6×10^{-6}	1.42°

Table 6.1 The substrate temperature dependence of the crystallinity of TiN.

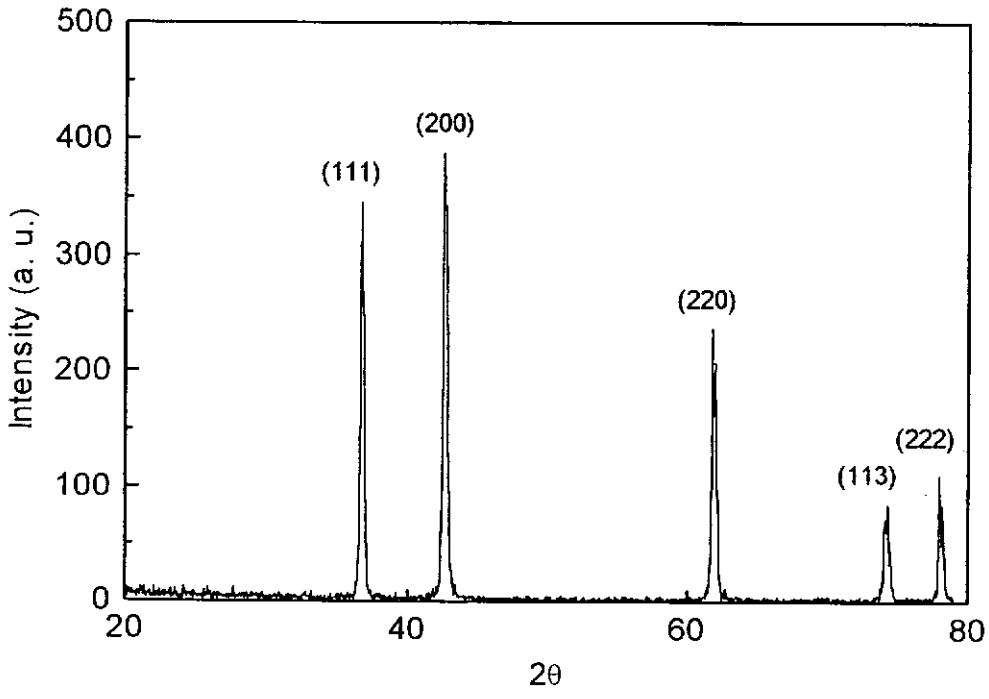

Figure 6.4 The XRD pattern of the TiN target.

Figure 6.5 shows the normal θ-2θ scan of the as-deposited TiN films on (100)Si substrates grown at 700°C. A single sharp peak of (200)TiN is observed suggesting a single phase TiN film. Figure 6.6 shows the rocking curve of the (200)TiN peak. The FWHM of the profile is 1.42°. This suggest that the crystal of the film is highly oriented. In order to determine whether the TiN films were epitaxially grown on the Si substrates, 360° ϕ-scans of the (220)TiN and (220)Si reflections were made. Figure 6.7 shows the ϕ-scans of (220)TiN and (220)Si reflection peaks. Four sharp peaks for each of the scans are obtained. The peaks are separated by 90°, confirming the fact that both the film and the substrate are of cubic structure. The four characteristics peaks of (220)TiN reflections are very sharp and their ϕ angles match that of the (220)Si reflections. This is a clear indication that the TiN films were epitaxially grown on the Si substrates. For other TiN films deposited at temperatures of 500°C and 600°C, similar results were also obtained. Figure 6.8(a) and 6.8(b) shows the rocking curves of (200)TiN reflection prepared at substrate temperatures of 600°C and 500°C respectively. Apparently the crystallinity of the TiN film, deteriorates at lower deposition temperatures.

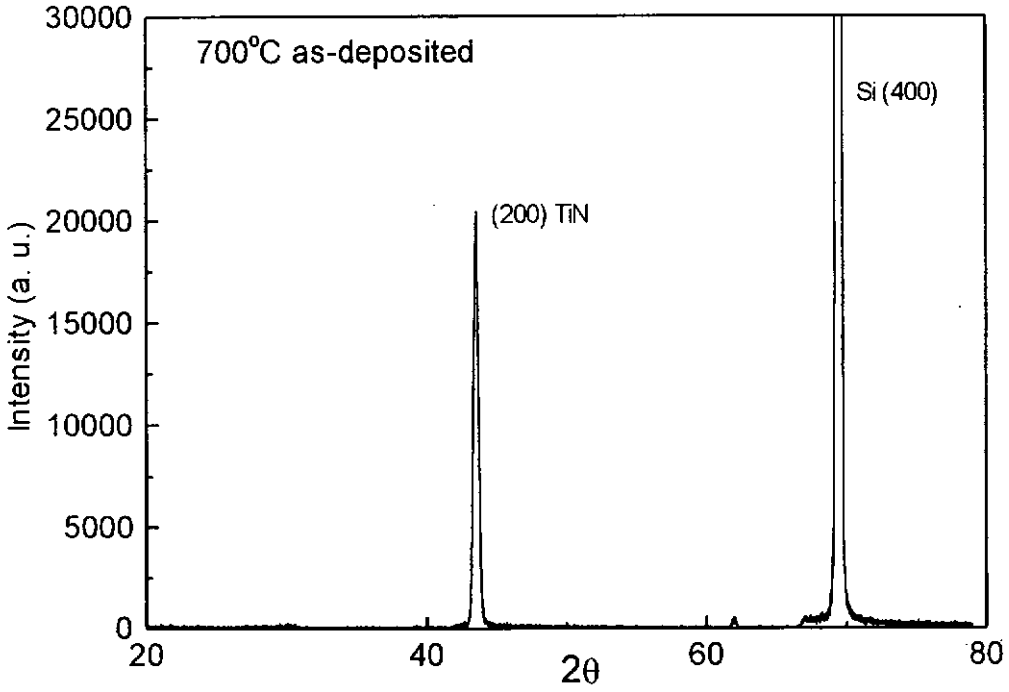

Figure 6.5 The XRD pattern of TiN film deposited on (100)Si substrate at substrate temperature of 700°C.

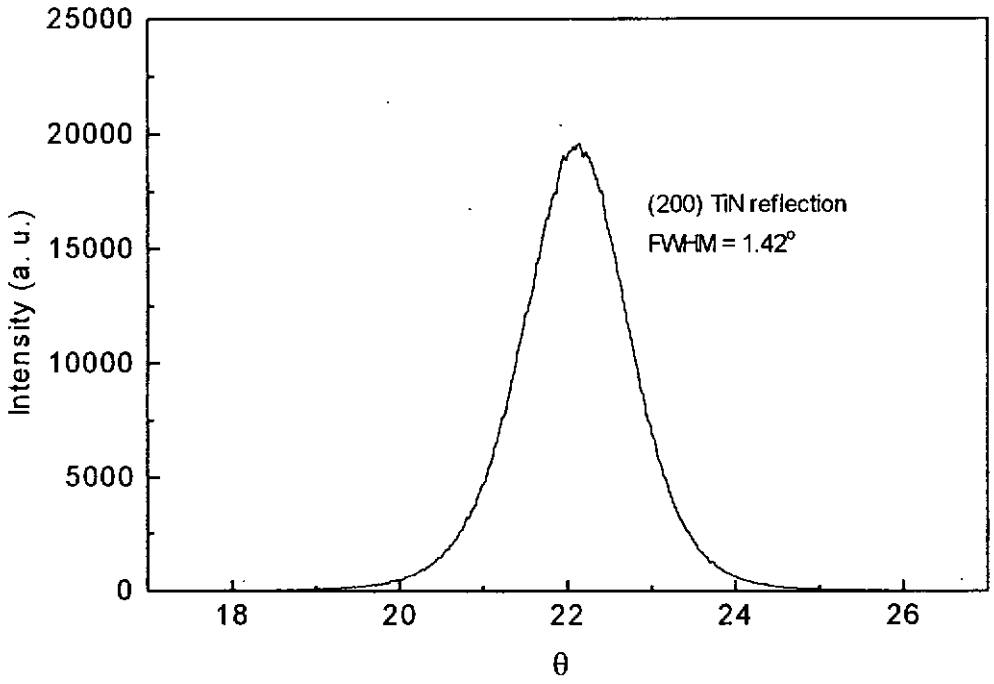

Figure 6.6 Rocking curve of (200)TiN reflection. The TiN film was as-deposited at 700°C.

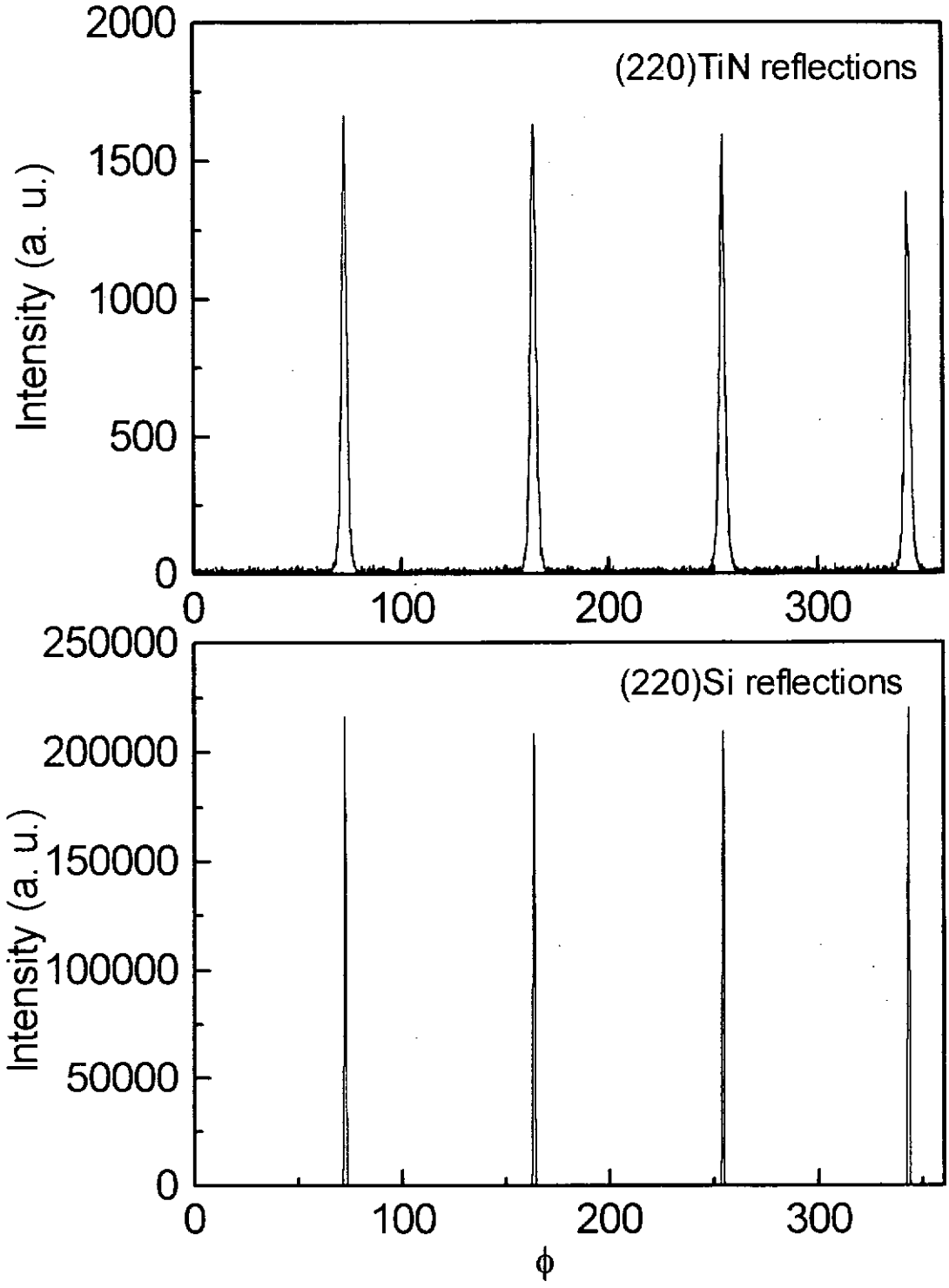

Figure 6.7 The X-ray ϕ-scan of the (220) reflections of TiN film and Si substrate.

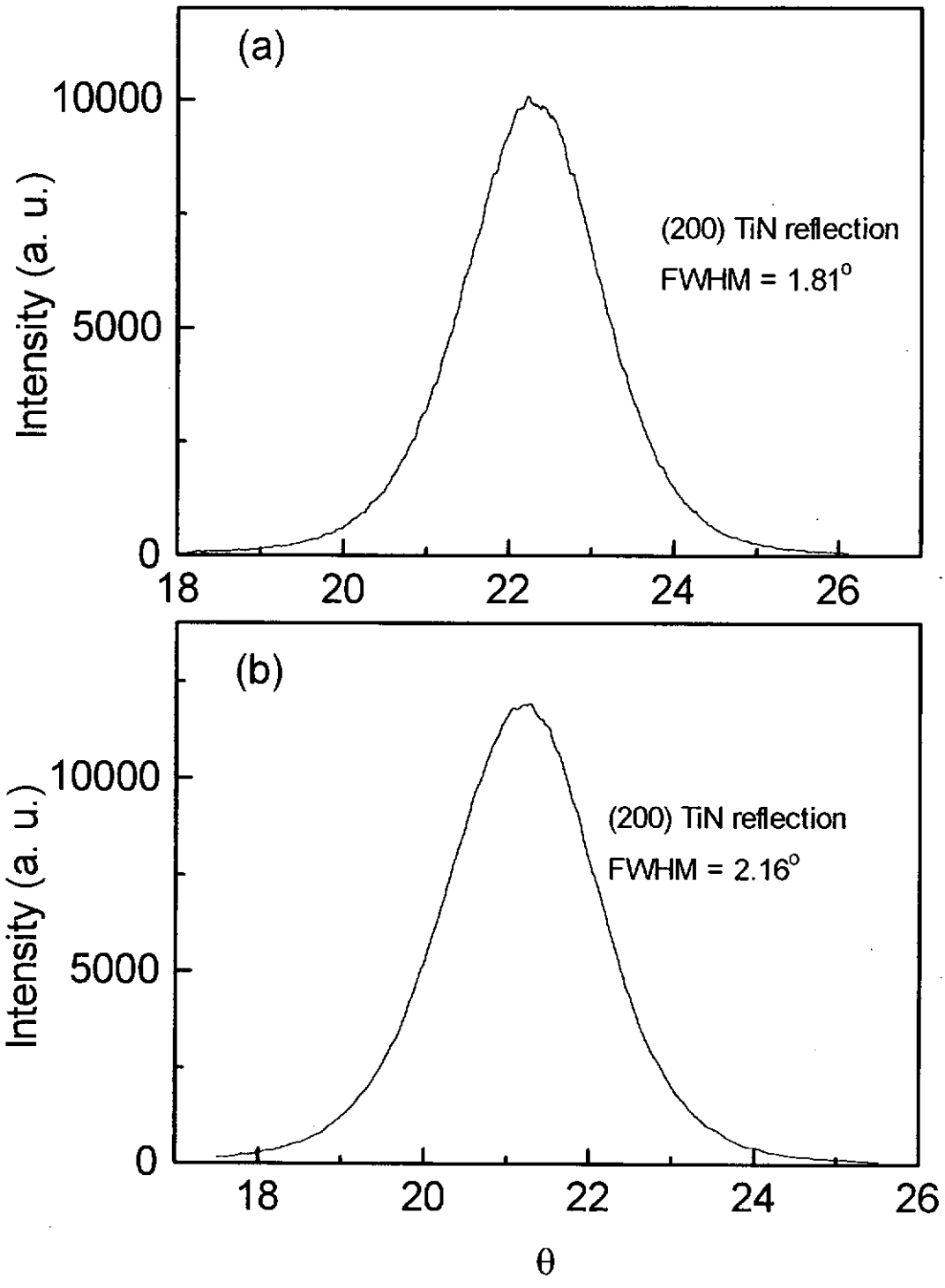

Figure 6.8 Rocking curves of (200)TiN prepared at substrate temperatures of (a) 600°C and (b) 500°C.

6.3.2 LCMO/TiN/Si

After the epitaxial growth of TiN film on Si had been confirmed, in-situ deposition of LCMO/TiN/Si heterostructures was attempted. Technically this is perhaps not the best structure for obtaining GMR effect from LCMO films on Si. Being a good electric conductor, the TiN layer in the LCMO/TiN/Si heterostructure will essentially short circuit the LCMO film. This will render the GMR effect, if there is any, of the LCMO films to be rather difficult to detect and to be utilized. Nevertheless it will be worthwhile and interesting to see the structural quality of LCMO/TiN/Si heterostructure and to study the effect of the oxide films on the nitride buffer layer.

All the TiN films were prepared at 600°C on (100)Si substrates under a base pressure of 6×10^{-6} Torr. LCMO films were then deposited onto the TiN buffer layers with various deposition conditions. Figure 6.9(a) shows the normal θ-2θ scans of TiN films prepared at substrate temperature of 600°C on (100)Si. A sharp and intense (200)TiN peak is observed and the FWHM of rocking curve is 1.81° (shown in figure 6.8(a)). The epitaxy of the TiN films are confirmed by ϕ-scans of (220)TiN and (220)Si. Figure 6.9(b) shows the XRD pattern of LCMO films deposited on the TiN buffered Si substrate at high vacuum (6×10^{-6}Torr), same as that for depositing TiN films. The deposition temperature for TiN film is 600°C and the LCMO film is 700°C. Strong (200)TiN and (*h*00)LCMO peaks are obtained. In addition a weak (110)LCMO peak is also observed. The FWHM of (200)TiN and (200)LCMO reflections are 2.8° and 3.5° respectively. These values suggest that the crystallinity of

the LCMO is not very good. It is multiphase and has poor orientation. Furthermore the deposition of LCMO films appears to degrade the crystallinity of the TiN layer. The FWHM of the rocking curve of the (200)TiN has been broadened significantly from 1.81° to 2.8°. It is believed that the oxygen from LCMO may diffuse to the structure of TiN. Consequently oxidation of TiN may occur and poor crystallinity of TiN is resulted.

It has been shown in chapter 4 that the best quality of LCMO films are obtained if they are deposited at 700°C under 200mTorr ambient oxygen and post annealed. In the present study, however, we found that the LCMO deposited under ambient oxygen and the post deposition annealing process destroyed the TiN buffered layers. Figure 6.10(a) shows the XRD pattern of the LCMO/TiN/Si film where the LCMO film was deposited under ambient oxygen of 200mTorr at 700°C on TiN/Si. It is seen that the sharp peak of (200)TiN shown in Figure 6.10(a) is disappeared completely. A mixed phases of (100)LCMO, (110)LCMO and (200)LCMO are observed. The other small peaks are probably due to the titanium oxides. This figure clearly shows that the TiN films are spoiled by the ambient oxygen deposition process. Figure 6.10(b), on the other hand, shows the XRD pattern of the LCMO/TiN/Si structure, in which both the TiN and LCMO were deposited under high vacuum. In stiu post annealing under 1atm O_2 at 700°C for half an hour was carried out immediately after the LCMO deposition. It can be seen that the (200)TiN peak is again conspicuously absent while the phases of (100)LCMO, (110)LCMO and (200)LCMO are observed.

We therefore conclude that the oxygen plays an important role in the deposition of heterostructures involving TiN buffer layers. The oxygen can easily oxidize the TiN films during deposition. To obtained high quality of LCMO films on TiN-buffered Si substrates, high vacuum should be maintained in the deposition process.

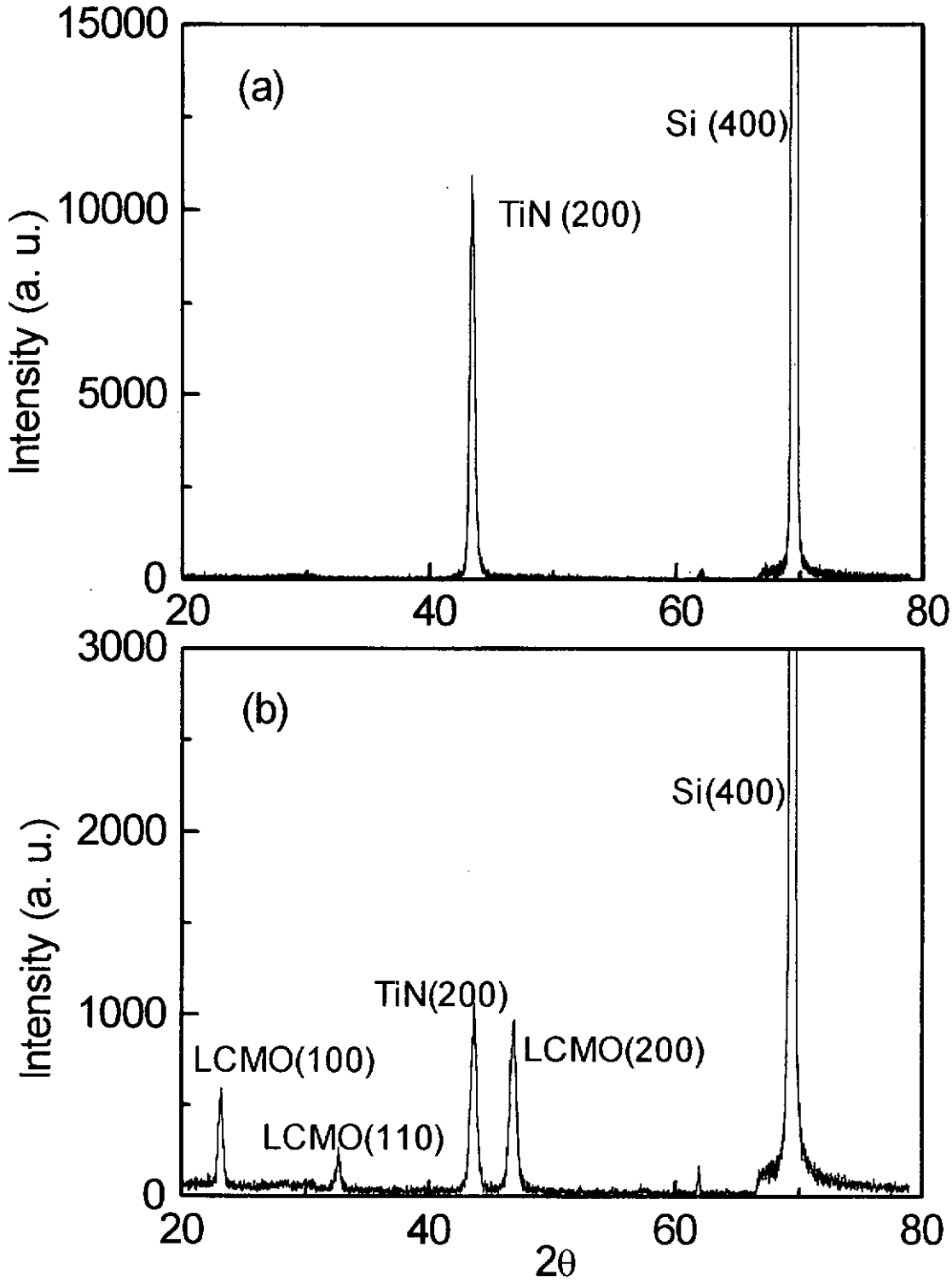

Figure 6.9 XRD pattern of (a) high vacuum (6×10^{-6}Torr) deposited TiN films on Si substrate at substrate temperature of 600°C and (b) LCMO films deposited on TiN-buffered Si substrate at 700°C and base pressure of 6×10^{-6}Torr.

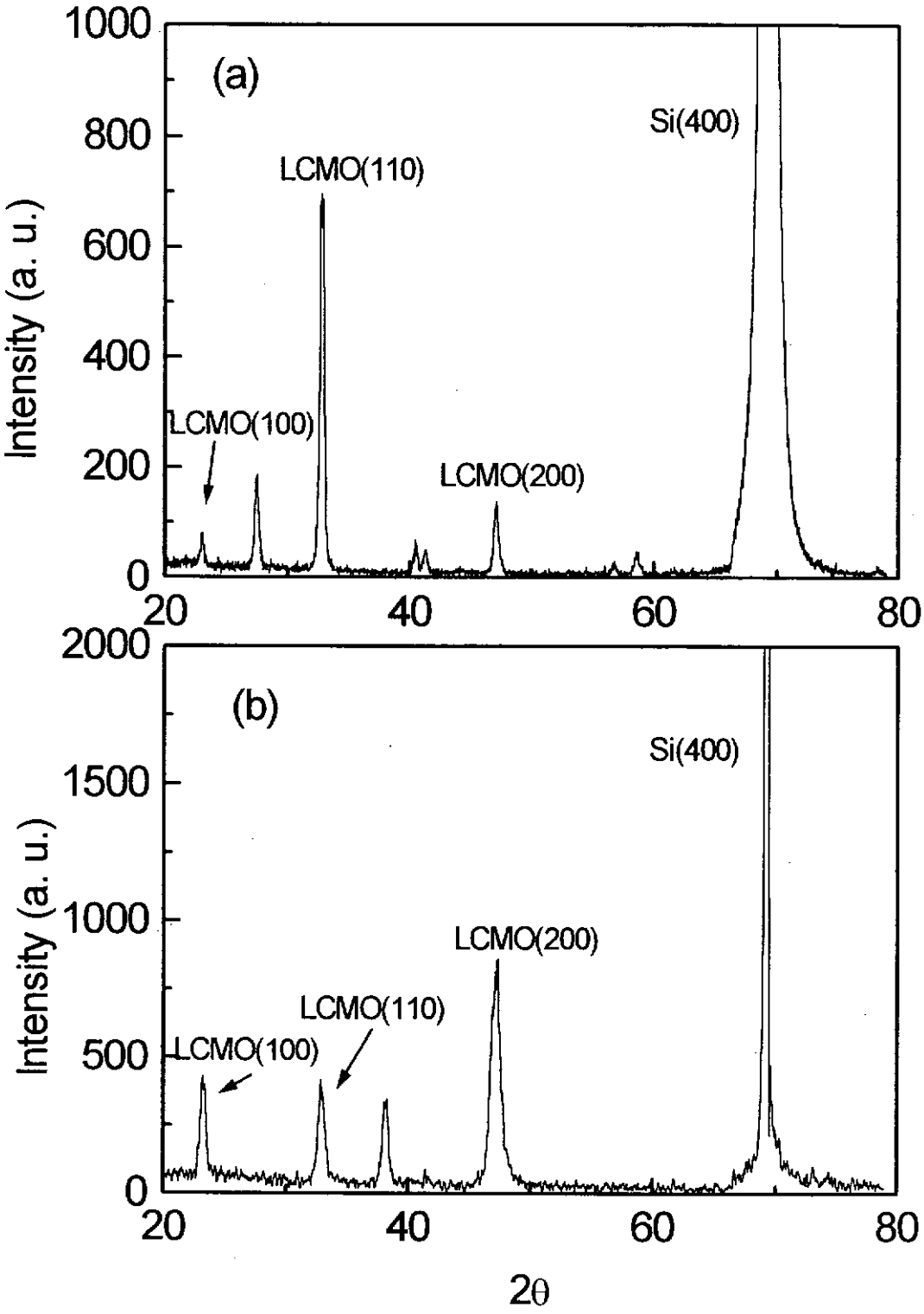

Figure 6.10 The XRD patterns of LCMO films deposited on TiN-buffered Si substrate at 700°C (a) under 200mTorr ambient oxygen and (b) in vacuum but with post deposition annealing (1atm O_2 at 700°C for half an hour).

6.4 Characterization of STO/TiN/Si and LCMO/STO/TiN/Si Heterostructures

The typical resistivity of TiN and LCMO are ~70μΩ.cm and ~1000mΩ.cm respectively. Therefore for LCMO/TiN heterostructure the MR of LCMO films cannot be easily measured and used. To overcome this problem, an insulating layer should be additionally deposited on top of the TiN layer. STO is the one that can epitaxially grown on TiN films [Vispute, 1996; Lee, 1997]. We therefore fabricated and finally deposited LCMO films on the heterostructures of STO/TiN/Si. Epitaxial LCMO films were obtained in LCMO/STO/TiN/Si heterostructure. Excellent MR ratio was recorded.

6.4.1 STO/TiN/Si

STO is an excellent insulating perovskite oxide. It has been extensively used as substrate for growing other perovskite oxide films. It has a lattice constant of 3.905Å and is therefore well lattice matched with both TiN (4.24Å) and LCMO (3.89Å). However, in the deposition of STO films on TiN, as was in the case of growing LCMO/TiN heterostructure, a high vacuum condition is needed to avoid undesirable oxidation of the TiN buffer layer. It has been shown previously that STO can be grown successfully and epitaxially in high vacuum by PLD method [Vispute, 1996; Lee, 1997]. We therefore attempted to fabricate the STO/TiN/Si heterostructure in high vacuum. STO films with film thickness ~100nm were prepared later on under laser fluence of $3J/cm^2$ with repetition rate 10Hz for 30 minutes. Figure 6.11 shows the XRD pattern of the STO perovskite oxide target. Figure 6.12 shows

the XRD 2θ-θ scan pattern of STO/TiN/Si. Both the STO and TiN films were deposited at 600°C under a base pressure of 6×10^{-6}Torr. Single phase of TiN and STO films were observed. Figure 6.13 shows the rocking curves of STO and TiN films. The FWHM of the (200)TiN and (200)STO reflections are 2.13° and 2.5° respectively. In order to improve the crystallinity of TiN and STO films, higher substrate temperatures of 700°C were used in all later STO/TiN deposition. The FWHM of rocking curve of (200)TiN and (200)STO reflections are narrowed to 1.83° and 1.3° respectively. They are depicted in figure 6.14. ϕ-scans of (220)STO and (220)TiN are shown in figure 6.15. They suggest good and clear interface and epitaxial STO/TiN heterostructure. From these results we can conclude that high quality of STO films are obtainable on the TiN-buffered Si substrates. STO/TiN/Si heterostructures can therefore be used for the deposition of LCMO films.

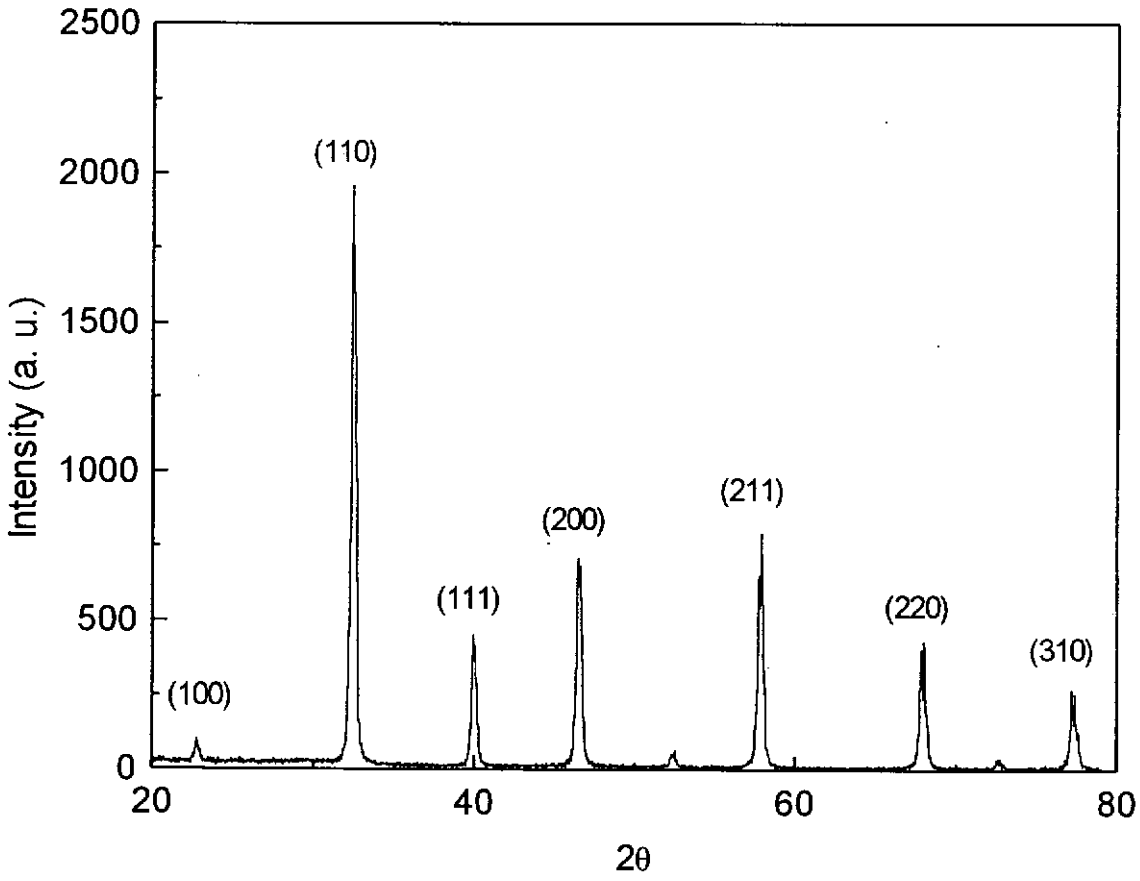

Figure 6.11 The XRD pattern of STO perovskite oxide target.

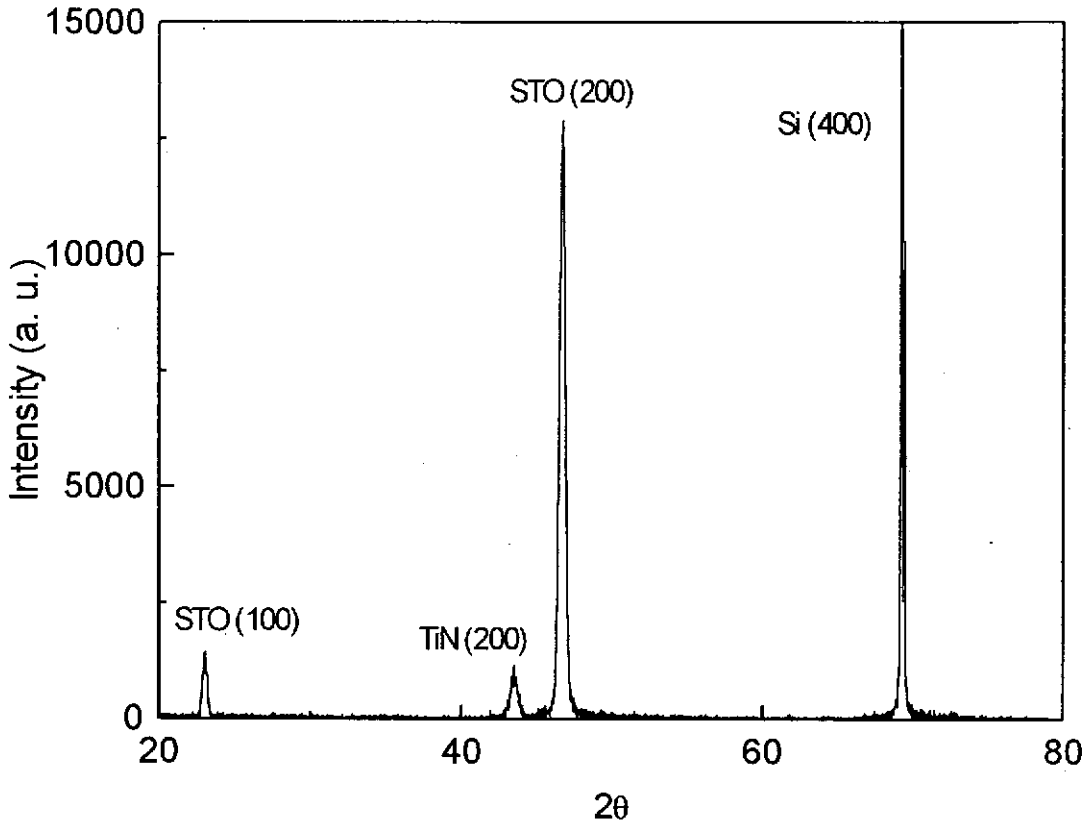

Figure 6.12 XRD pattern of the STO/TiN/Si heterostructure prepared at 600°C and base pressure of 6×10^{-6}Torr.

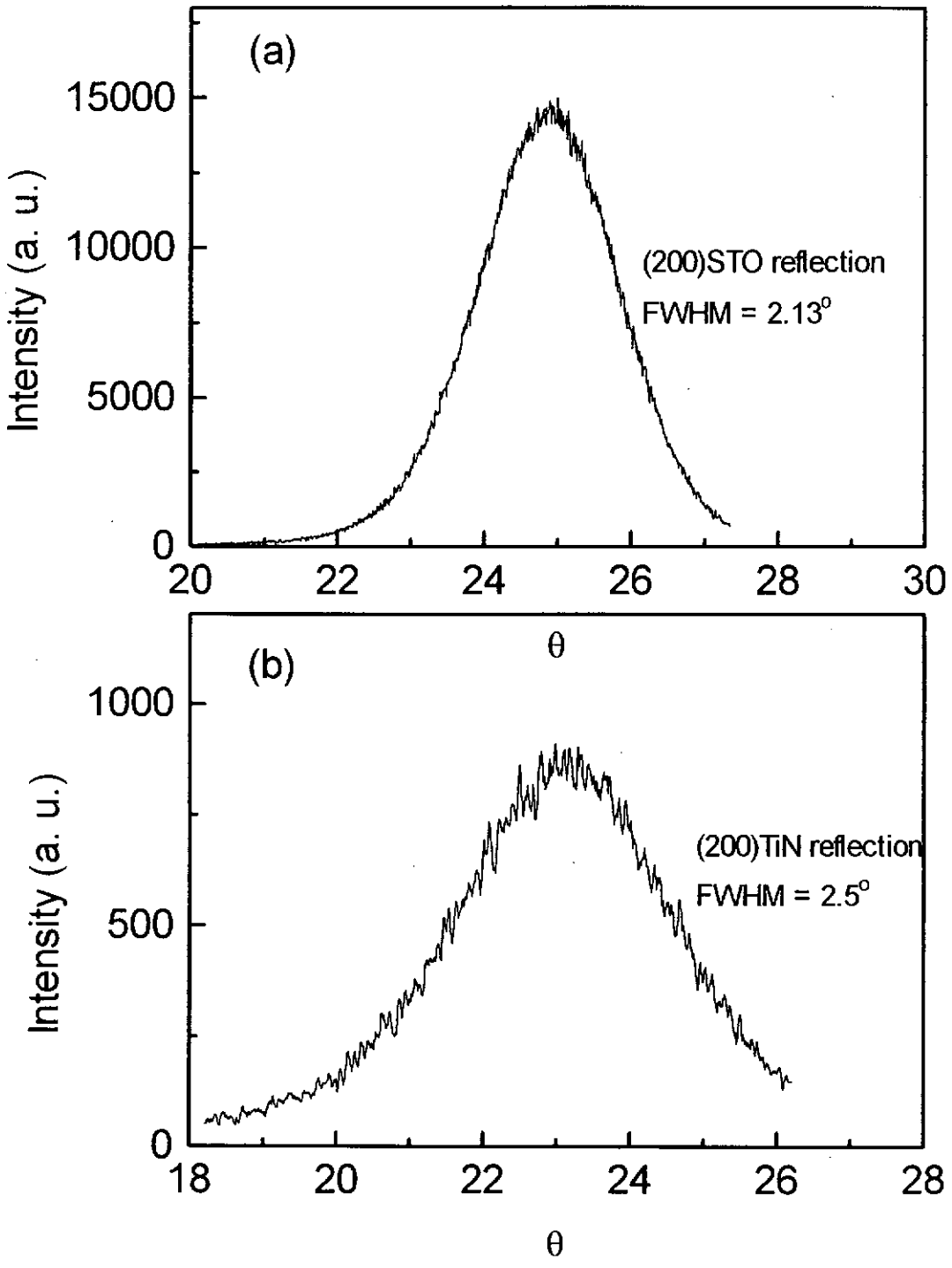

Figure 6.13 Rocking curves of (a) (200)STO and (b) (200)TiN. Both films deposited at 600°C under base pressure of 6×10^{-6} Torr.

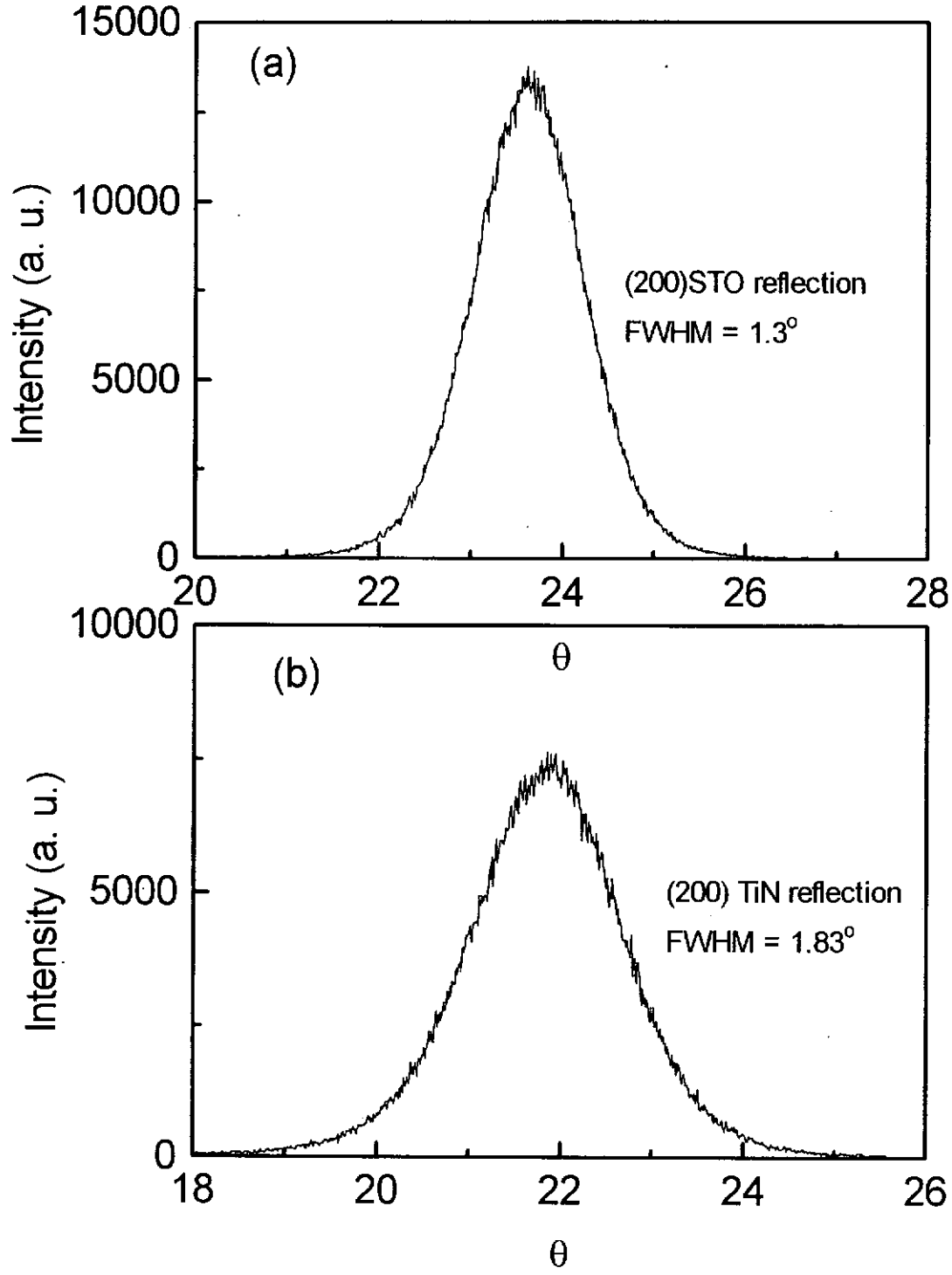

Figure 6.14 Rocking curves of (a) (200)STO and (b) (200)TiN. Both films were deposited at 700°C under a base pressure of 6×10^{-6} Torr.

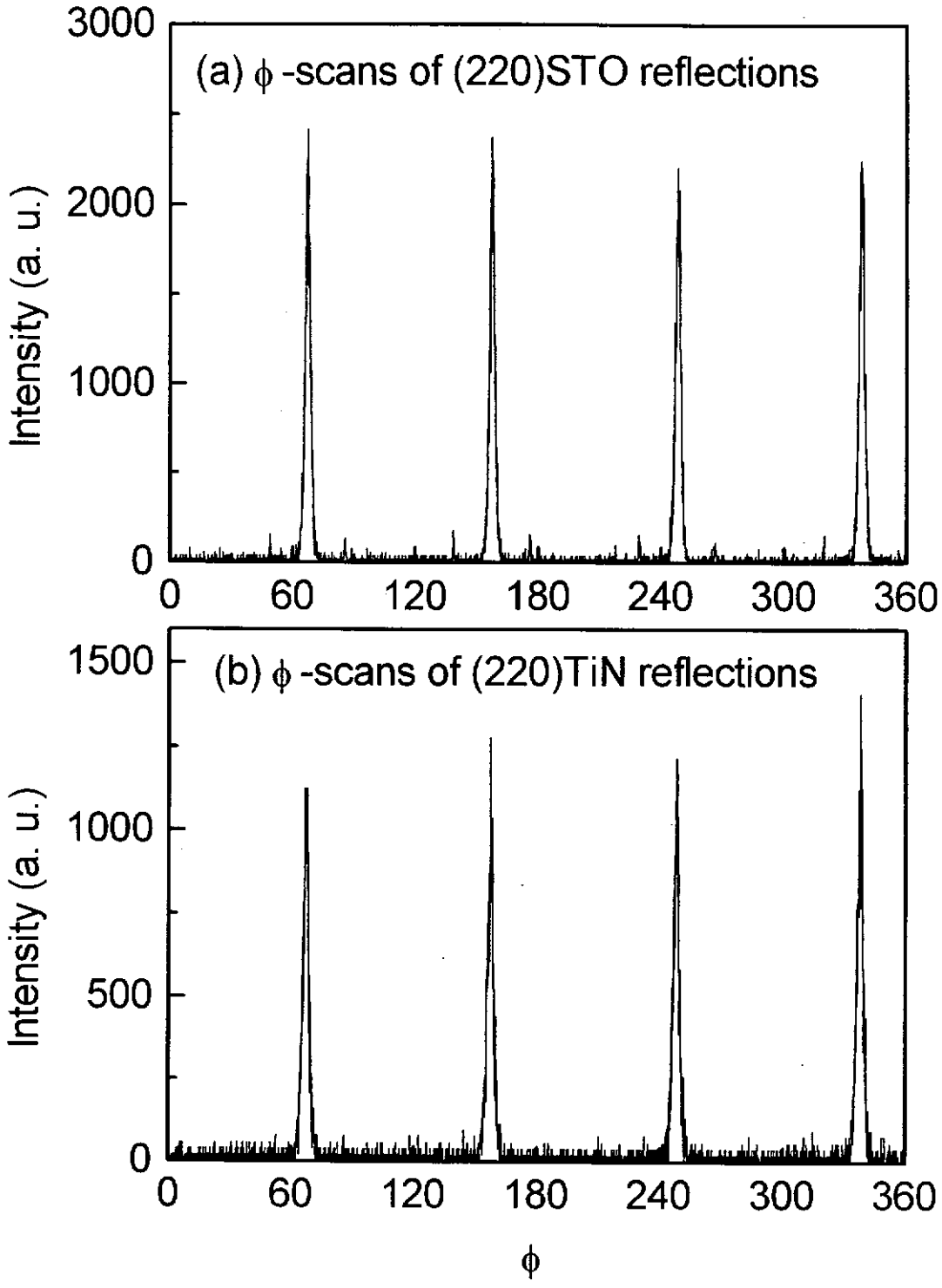

Figure 6.15 ϕ-scans of (a) (220)STO and (b) (220)TiN reflections. Both films were deposited at 700°C under a base pressure of 6×10^{-6} Torr.

6.4.2 LCMO/STO/TiN/Si

The whole of the multilayered LCMO/STO/TiN/Si heterostructure was fabricated in situ within one single vacuum cycle by making use of our unique multi-target holder. After the STO film had been successfully grown on TiN-buffered Si substrates, LCMO film was immediately deposited on top. The deposition condition for this final LCMO layer was therefore set at substrate temperature of 700°C and ambient oxygen pressure of 200mTorr. Figure 6.16 shows the XRD θ-2θ scans of the heterostructures of LCMO/STO/TiN/Si. From the figure, sharp and intense peaks corresponding to single phase of the TiN, STO and LCMO films are observed. It is interesting to observe that the (200)LCMO and (200)STO reflections can be resolved. In fact the lattice constants of LCMO and STO are very close, 3.89Å for LCMO and 3.905Å for STO. Their (200) reflections should be overlaped. Apparently (200)LCMO peak has shifted to a larger angle suggesting a lattice contraction. The change of lattice constant due to strain layer and oxygen deficiency is not uncommon in perovskit oxides [Ju, 1995]. However, the detail mechanism responsible for our observation is not known and can form a good topic for further studies. Figure 6.17 shows the rocking curves of (200)LCMO, (200)STO and (200)TiN reflections. The FWHM values of the rocking curves of LCMO(200), STO(200) and TiN(200) reflections are 1.59°, 1.46° and 1.8°, respectively. These values suggest that the three layers are good oriented crystalline films. The STO layer helps to maintain the structural quality of TiN from oxidation during the growth of LCMO in ambient oxygen. The epitaxy of the films are confirmed by ϕ-scans of the (220)LCMO, (220)STO, (220)TiN and (220)Si reflections shown in figures 6.18 and 6.19. In all

these ϕ-scans, four characteristics peaks of a cubic structure are observed. The positions of the four peaks from the films are in good match with the (220)Si reflections. This strongly suggest that all these films are epitaxially cube-on-cube grown on top of the underlying layer or Si substrate.

Figure 6.20 shows the R-T curves and MR profile of LCMO films deposited on the STO/TiN/Si heterostructure. From the figure, the T_c at B=0T is 120K and it is shifted to 140K under a B-field of 1.2T. The maximum MR% ($MR = (R_H - R_0)/R_0$) is about -50% at temperature of 116K. Figure 6.21 shows the MR profiles for LCMO films prepared on (100)LAO substrates and on STO/TiN/Si heterostructure. Both the LCMO films deposited on LAO and on STO/TiN/Si have excellent and comparable MR quality. The maximum MR% for LCMO deposited on LAO substrates and on STO/TiN/Si are both close to 50% (B=1.2T) at 116K and 170K respectively. For LCMO films deposited on Si substrates directly, their structure is poor and the T_c is much lower than 77K. The measured MR ratio is negligible.

In conclusion, good quality LCMO films cannot be prepared on Si substrates directly due to lattice mismatch, oxidation and chemical diffusion into the Si substrate. Our work, however, demonstrates that high quality LCMO with good MR can be grown epitaxially on STO/TiN/Si heterostructure. Thus we have verified that fabrication of integrated devices based on the MR effect of LCMO films and Si microelectronic technology is possible. In fact our work has a wider implication that the integration of all other functional perovskite oxide films to Si can be implemented in the similar way.

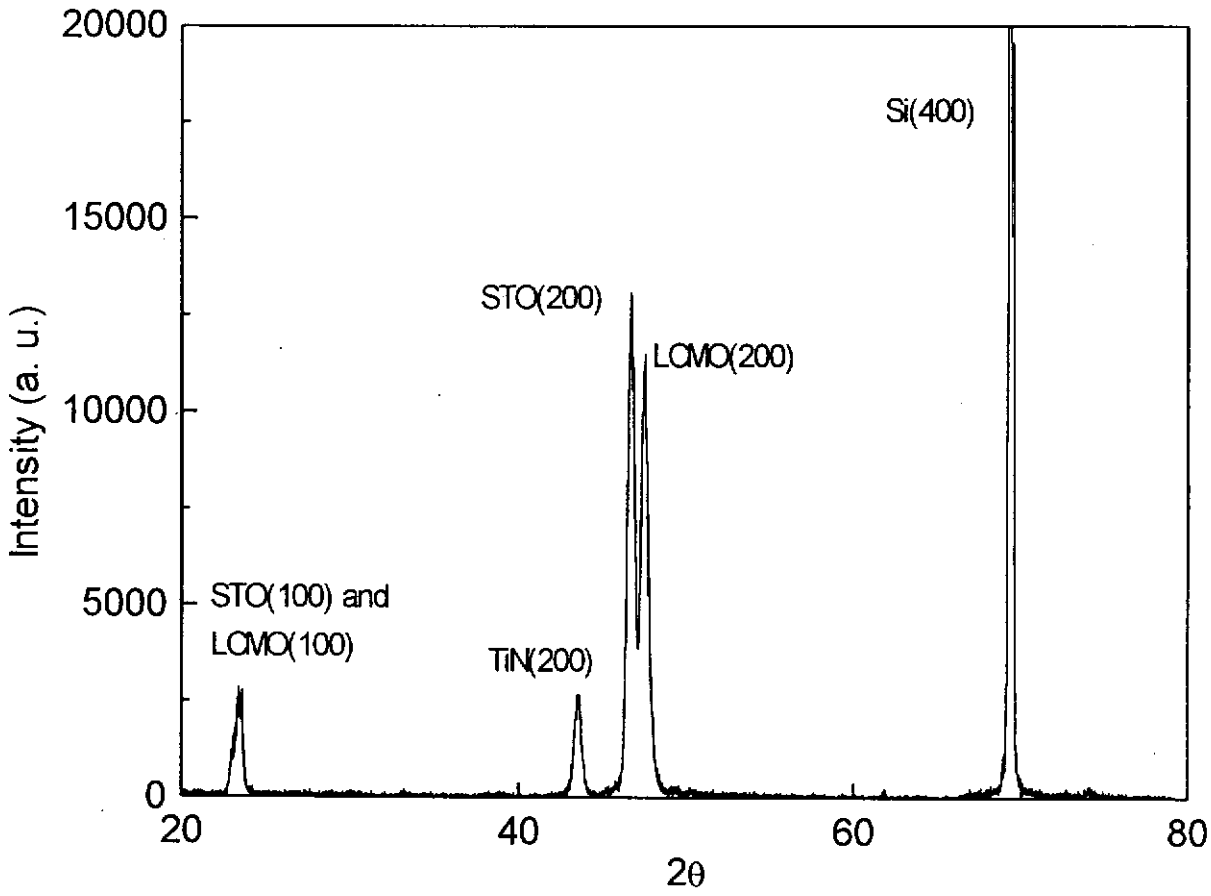

Figure 6.16 XRD pattern of LCMO/STO/TiN/Si heterostructure.

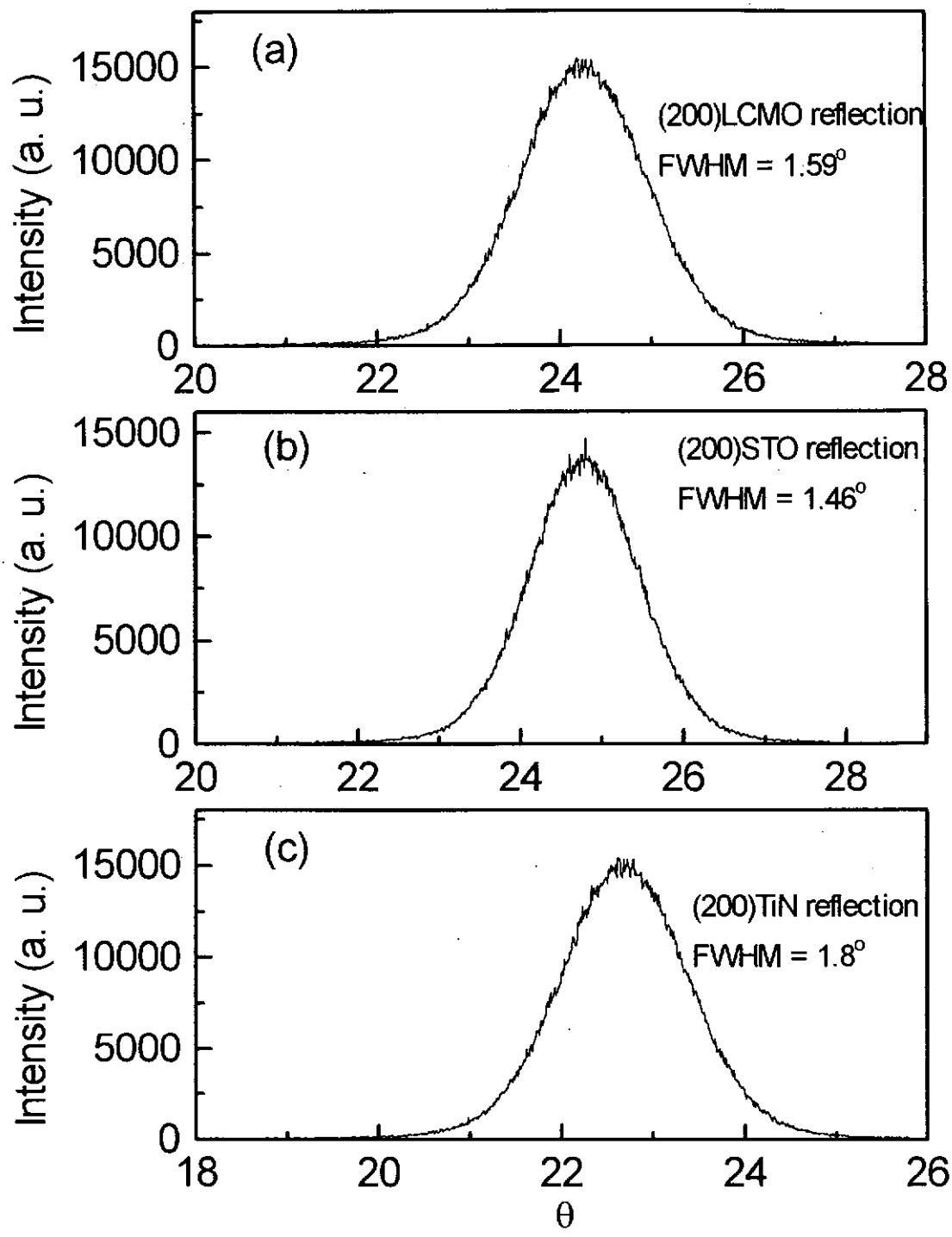

Figure 6.17 Rocking curves of (a) (200)LCMO, (b) (200)STO and (c) (200)TiN reflections. The LCMO film was deposited at 700°C under ambient oxygen pressure of 200mTorr while the STO and TiN films were deposited at 700°C under a base pressure of 6×10^{-6} Torr.

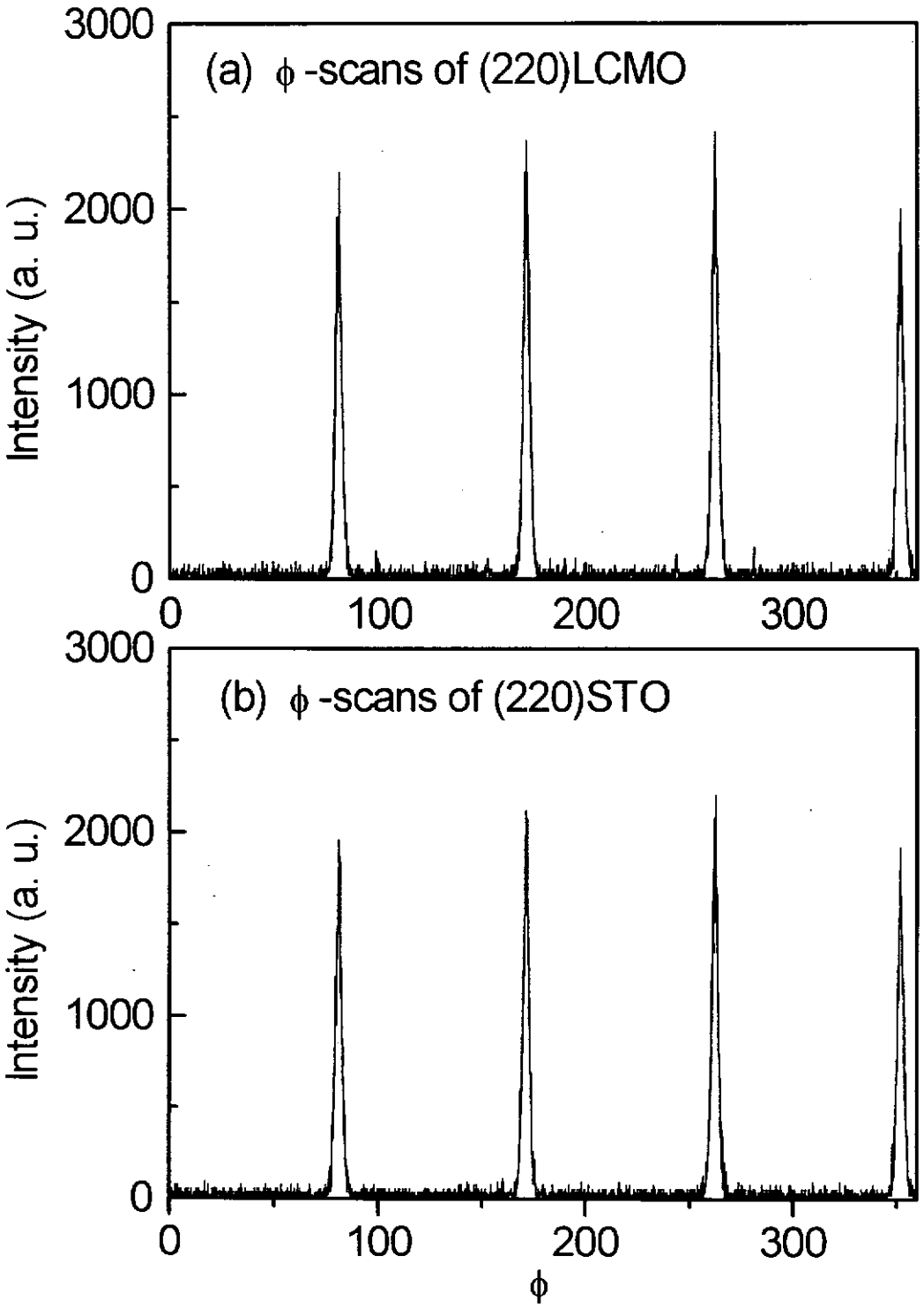

Figure 6.18 The ϕ-scans of (a) (220)LCMO reflections and (b) (220)STO reflections

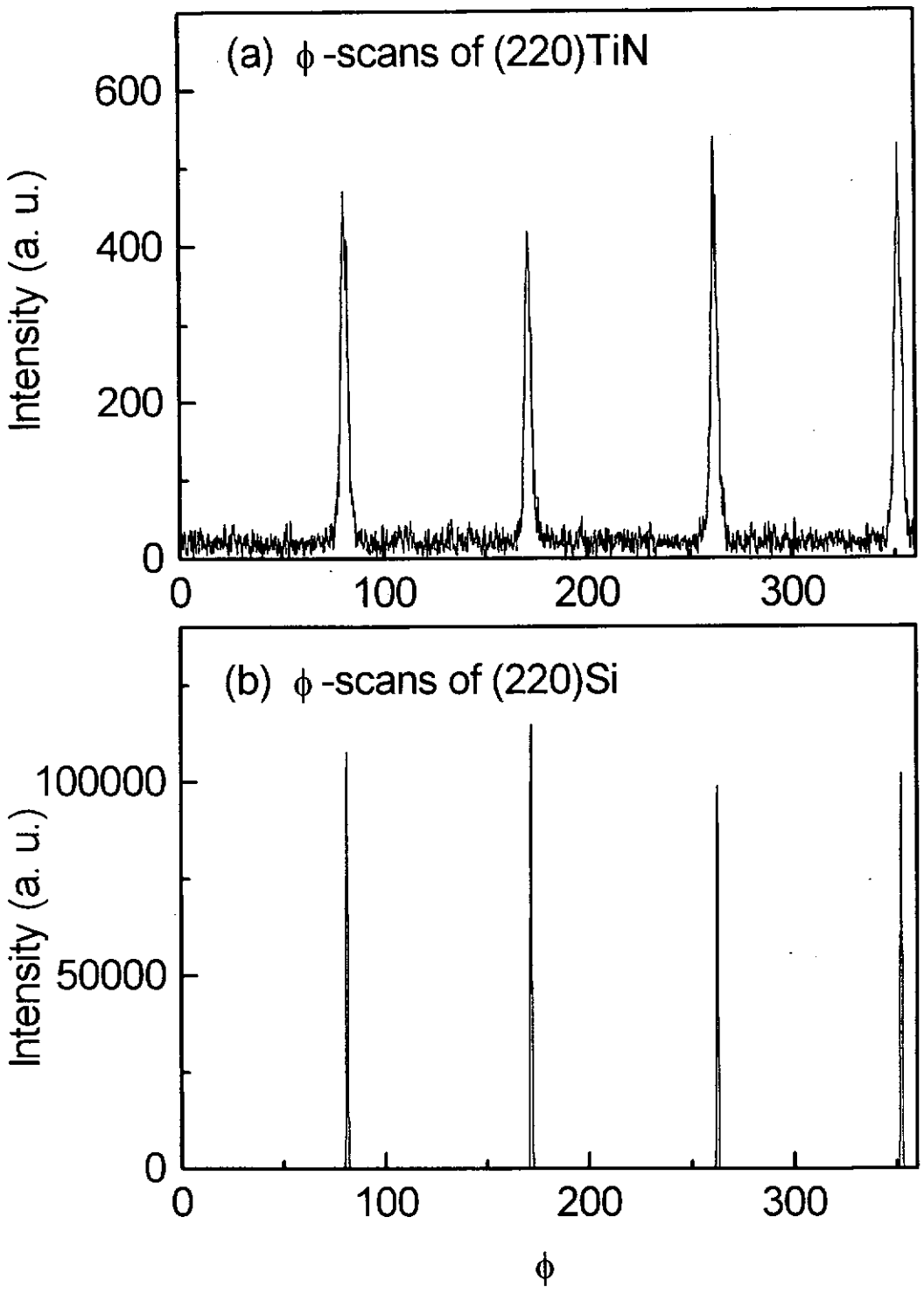

Figure 6.19 The ϕ-scans of (a) (220)TiN reflections and (b) (220)Si reflections.

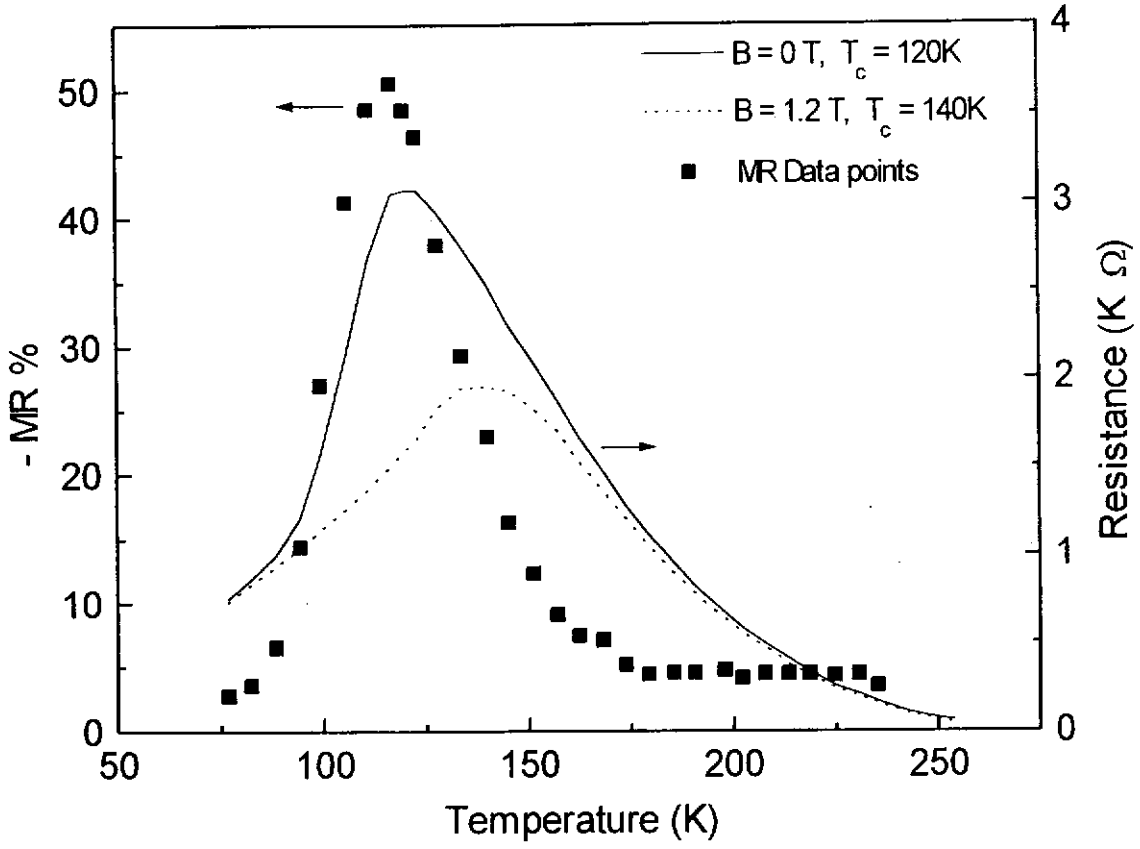

Figure 6.20 The R-T curves and MR profile of as-deposited LCMO film in LCMO/STO/TiN/Si heterostructure. The LCMO film was deposited at 700°C under 200mTorr ambient oxygen pressure.

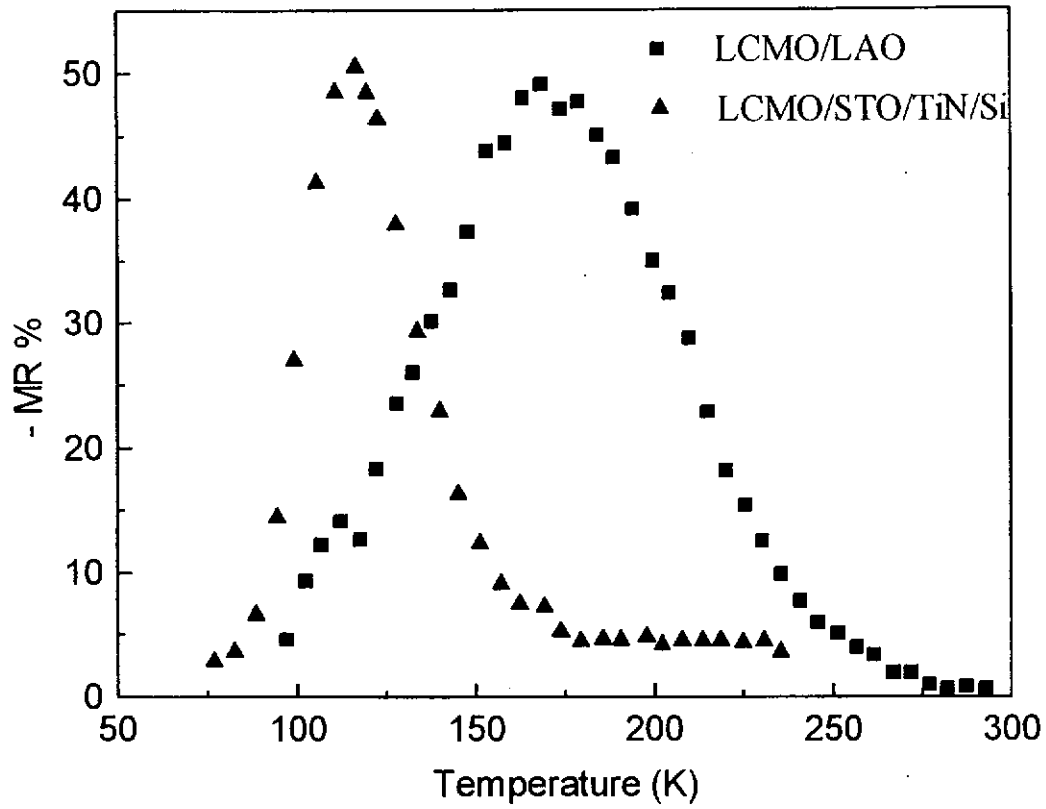

Figure 6.21 The MR profiles for LCMO films deposited on single crystal LAO substrates (■) and on STO/TiN/Si heterostructure (▲) under an applied B-field of 1.2T.

Conclusion

In the present experimental investigation excellent quality epitaxial giant magnetoresistive perovskite LCMO thin films have been successfully obtained by the PLD method. The LCMO films were prepared on (100)LAO single crystal substrate and on (100)Si substrate either directly or indirectly through buffer layers of TiN and STO. The structural, electrical and magnetic properties of the LCMO films were characterized in details.

For LCMO films fabricated on (100)LAO substrates, the threshold deposition temperature to obtain epitaxial LCMO films is only 650°C. In the temperature range of 600°C - 750°C, the film's resistivity decreases with increasing temperature. The semiconductor-metal transition temperature (T_c) is, however, up-shifted. The highest value of T_c is obtained for films prepared at 700°C. Oxygen deficient appears not to occur in LCMO films at this temperature range. At higher deposition temperature, however, T_c starts to drop. It is believed that oxygen depletion begins to set in at temperatures higher than 700°C. The post deposition annealing carried out under high pressure of oxygen (1 atm O_2) and at high temperatures (600°C - 750°C) for about one hour has markedly improved the crystallinity and conductivity of the films. It also raises the T_c by ~20K. The giant magnetoresistance properties of the LCMO films were determined by measuring their magnetoresistance ratio (MR). The values of MR% are found to depend on the processing temperature and the applied field strength. It has been found that the MR% increases with increasing processing temperature. A maximum MR% of 49% at 135K and 37% at 110K were obtained

under an applied B-field of 1T for films deposited and post-annealed at 750°C and 650°C respectively.

From our results, the T_c and the crystallinity appear to increase with the deposition temperature up to about 700°C. At still higher temperature, T_c starts to drop whereas the crystallinity continues to improve. It is believed that oxygen depletion begins to set in here resulting a lower T_c. It is in good agreement with the results reported by Zhang et al. where they stated that oxygen deficient occurred at high temperature (~700°C - 900°C) [Zhang et al., 1996]. The MR% of the LCMO films, however, increases with the processing temperature and the maximum value is obtained under our highest processing temperature of 750°C. The post-annealing process on the other hand, improves the crystallinity and increases the oxygen content of the LCMO films. The results of which lead to a much higher T_c and larger MR%. However, the relative important of the film's crystallinity and oxygen content, on the MR% and T_c remain not clear. In order to better understand their effect in the film grown process more detailed investigations are needed. For example, improves the film's crystallinity but not the oxygen content. This will help us to yield a more definitive result on how the MR properties affected by crystallinity.

For LCMO deposited directly on (100)Si substrates, multi-phase crystalline films were formed. The samples were semiconducting like and showed no semiconductor-metal transition in the whole temperature range studied. Their T_c were apparently at well below 77K (liquid nitrogen temperature). No measurable MR effect was observed.

TiN buffer layers have been grown epitaxially on Si substrate in a wide range of substrate temperature of 500°C - 700°C. Improved crystallinity has been obtained by using higher deposition temperatures. LCMO films have been subsequently deposited on TiN-buffered Si substrates. Our results show that the process of depositing LCMO has degraded the TiN buffer layer and at the same time produced a relatively poor quality LCMO films. Deposition of LCMO under ambient oxygen pressure and post deposition annealing of the LCMO films have completely destroyed the TiN buffer layer due to oxidation. The resulted LCMO films are multi-phase and have poor MR properties. Insulating STO buffer layers have been shown to grown epitaxially on TiN-buffered Si substrates. The STO/TiN/Si heterostructure thus provide a perfect platform for depositing LCMO. Indeed epitaxial LCMO/STO/TiN/Si heterostructures have been fabricated. The MR% obtained is 50% at 116K under a B-field of 1.2T. This value is comparable to that of the LCMO films prepared on (100)LAO single crystal substrates under similar deposition conditions. A MR% of 50% (B=1.2T) is indeed very good in comparison with values reported in the literature (e.g. 80% at B≥6T).

In conclusion, we have therefore demonstrated that excellent LCMO films can be grown on Si through appropriate buffer layers. Our work has clearly demonstrated that integrated devices based on functional ceramic and Si technology can be fabricated. The PLD method, although simple, has been shown to offers a very versatile and convenient technique for processing high quality multi-layer heterostructures.

From the present studies, some further work of interest are summarized as follows:

(1) To study oxidation phenomenon of TiN in the heterostructure. Unchecked oxidation of TiN may render it from being a good buffer layer for epitaxial film growth on Si. The oxidation phenomenon of TiN in heterostructure therefore needs to be closely scrutinized.

(2) To improve the structural quality of TiN/Si and STO/TiN/Si heterostructures as they can act as excellent platform for deposition of many kinds of thin films.

(3) To grow other useful perovskite oxides, such as YBCO, PZT, BTO....etc., on Si as these will generate many potential devices applications.

(4) To study the phenomenon of lattice distortion of perovskite oxides thin films in the heterostructure as this may yield important informations and controllable parameters on strained layers and superlattices..

References

Askar'yan, G.A.,. Pokhorov, A.M., Chantutiya, G.F., and Shipulo, G.P.
Sov. Phys. JETP, Vol,. 17, p.6. (1963)

Bae, S.Y., and Wang, S.X.
"Sol-gel epitaxial growth of $La_{1-x}Ca_xMnO_3$ with colossal magnetoresistance effect"
Appl. Phys. Lett., Vol. 69, p.121 (1996)

Baibich, M.N., Broto, J.M., Fert, A., Nguyen, F. van Dau, Petroff, F., Etienne, P., Creuzet, G., Friederich, A., and Chazelas, J.
"Giant magnetoresistance of (001)Fe/(001)Cr magnetic superlattices"
Phys. Rev. Letters, Vol. 61, p.2472 (1988)

Belov, K.P., Svirina, E.P., Patugal, O.E., Lukina, M.M., and Sotnikova, V.
Sov. Phys. Sol. St., Vol. 20, p.2021 (1978)

Bokov, V.A., Grigoryan, N.A., Bryzhina, M.F., and Tikhonov, V.V.
Phys. Status Solid., Vol. 28, p.835. (1968)

Brown, W.L., Jarrold, M.F., McEachern, R.L., Sosnowski, M., Takoaka, G., Usui, H., and Yamada, I.
Nucl. Instrum. Meth. Phys. Res., Vol. B59/60, p.182. (1991)

Bunshah, R.F.
"Deposition Technologies for Films and Coatings"
Noyes Publisher - Park Ridge (1982)

Caignaert, V., Maignan, A., and Raveau, B.
Sol. St. Comm., Vol. 95(6), p.357. (1995)

Chahara, K.I., Ohno, T., Kasai, M., and Kozono, Y.
"Magnetoresistance in magnetic manganese oxide with intrinsic antiferromagnetic spin structure"
Appl. Phys. Lett., Vol. 63, p.1990 (1993)

Chan, P.W., Wu, W.B., Wong, K.H., Tong, K.Y., and Cheung, T.
"Preparation and characterization of epitaxial $La_{0.5}Sr_{0.5}CoO_3$ films and of an all a-axis oriented $YBa_2Cu_3O_{7-y}$ / $La_{0.5}Sr_{0.5}CoO_3$ / $YBa_2Cu_3O_{7-y}$ heterostructures on (001)$LaAlO_3$ by pulsed laser deposition"
J. Phys. D: Appl. Phys., Vol. 30, p.957 (1997)

Chang, L.D., Tseng, M.Z., Hu, E.L., and Fork D.K.
"Epitaxial MgO buffer layers for $YBa_2Cu_3O_{7-x}$ thin films on GaAs"
Appl. Phys. Lett., Vol. 60(14), p.1753 (1992)

Cheung, J.T., Gergis, I.M., James, J., and DeWames, R.E.
"Reproducible growth of high quality $YBa_2Cu_3O_{7-x}$ film on (100)MgO with a $SrTiO_3$ buffer layer by pulsed laser deposition"
Appl. Phys. Lett., Vol. 60(25), p.3180 (1992)

Chowdhury, R., Chen, X., Jagannadham, K., and Narayan, J.
"Laser processing, characterization, and modeling of epitaxial Si/TiN/Si (100) heterostructures"
Mat. Res. Soc. Symp. Proc., Vol. 285, p.501 (1993)

Chrzanowski, J., Burany, S.M., Curzon, A.E., Irwin, J.C., Heinrich, B., Cragg, R.A., Backhouse, C., Angus, V., Habib, F., Zhou, H., and Fife, A.A.
"Epitaxial bilayer and trilayer heterostructures grown on $LaAlO_3$ and $SrTiO_3$(001) single crystals by laser ablation"
Superconductivity Science Technology, Vol. 8, p.455 (1995)

Coey, J.M.D., Viret, M., and Ranno, L.
"Electron localization in mixed-valence manganites"
Phys. Rev. Lett., Vol. 75, p3910 (1995)

Crandles, A, Timusk, T., and Greendan, J.E.
"Reflectance and resistivity of barely metallic $LaTiO_3$"
Phys. Rev., Vol. B44, p.13250. (1991)

Dijkkamp, D., et al.
"Preparation of Y-Ba-Cu oxide superconductor thin films using pulsed laser evaporation from high T_c bulk material"
Appl. Phys. Lett., Vol. 51, p.619 (1987)

Doll, G.L., Sell, J.A., Taylor, C.A., and Clarke, R.
"Growth and characterization of epitaxial cubic boron nitride films on silicon"
Phys. Rev., Vol. B43, p.6816 (1991)

Fork, D.K., Fenner, D.B., Connell, G.A.N., Phillips, J.M., and Geballe, T.H.
"Epitaxial yttria-stabilized zirconia on hydrogen-terminated Si by pulsed laser deposition"
Appl. Phys. Lett., Vol. 57, p.1137 (1990)

Fork, D.K., Nashmoto, K.,and Geballe, T. H.
"Epitaxial $YBa_2Cu_3O_{7-\delta}$ on GaAs(001) using buffer layers"
Appl. Phys. Lett., Vol. 60, p.1621 (1992)

Friedmann, T.A., et al.
"Cubic boron nitride formation on Si(100) substrates at room temperature by pulsed laser deposition"
Appl. Phys. Lett., Vol. 61, p.2406 (1992)

Gennes, P. G. DE.
"Effects of Double Exchange in Magnetic Crystals"
Phys. Rev., Vol. 118, p.141 (1960)

Geusic, J.E., Marcos, H.M., and Uitert, L.G. Van
Appl. Phys. Lett., Vol. 4, p.182 (1964)

Gong, G. Q., Canedy, C. L., and Gang Xiao
"Colossal magnetoresistance in the antiferromagnetic $La_{0.5}Ca_{0.5}MnO_3$ system"
J. Appl. Phys., Vol. 79, p.4538 (1996)

Goodenough, J.B., and Lango, J.M.
"Magnetic and other properties of oxides and related compounds"
Springer-New York (1970)

Greer, J.A.
"Superconductivity and Applications"
Plenum-New York, pp.117-126 (1989)

Greer, J.A., and Hook, H.J. Van
Mat. Res. Soc. Symp. Proc., Vol. 191, p.171 (1990)

Greer, J.A.
"High quality YBCO films grown over large area by pulsed laser deposition"
J. Vac. Sci. Technol., Vol. A10, p.1821 (1992)

Gu, J.Y., Kim, K.H., Noh, T.W., and Suh, K. -S.
"Epitaxial growth and magnetoresistance of $La_{1-x}Ca_xMnO_{3-\delta}$ thin films on MgO(001) substrates"
J. Appl. Phys., Vol. 78, p.6151 (1995)

Hau, S.K., Wong, K.H., Chan, P.W., and Choy, C.L.
"Intrinsic resputtering in pulsed-laser deposition of lead-zirconate-titanate thin films"
Appl. Phys. Lett., Vol. 66, p.245 (1995)

Helmolt, R. Von, Haupt, L., Barner, K., and Sondermann, U.
Sol. St. Comm., Vol 82, p.693 (1992)

Helmolt, R.Von, Wecker, J., Holzapfel, B., Schultz, L., and Samwer, K.
"Giant negative magnetoresistance in perovskitelike $La_{2/3}Ba_{1/3}MnO_x$ ferromagnetic films"
Phys. Rev. Lett., Vol. 71, p.2331 (1993)

Horwitz, J.S., Grabowski, K.S., Chrisey, D.B., and Leuchtner, R.E.
"In situ deposition of epitaxial $PbZr_xTi_{(1-x)}O_3$ thin films by pulsed laser deposition"
Appl. Phys. Lett., Vol. 59, p.1565 (1991)

Huang, C.S., Lin, I.N., Lee, Y.M., and Tseng, T.Y.
"Growth behavior of $Y_1Ba_2Cu_3O_{7-x}$ superconducting thin films using laser ablation technique"
Jpn. J. Appl. Phys., Vol. 33, p.4058 (1994)

Iwabuchi, M., Kinoshita, K., Ishibashi, H., and Kobayashi, T.
"Reduction of pinhole leakage current of $SrTiO_3$ films by ArF excimer laser deposition with shadow mask ("Eclipse method")"
Jpn. J. Appl. Phys., Vol. 33, p.L610 (1994)

Jin, S., Tiefel, T.H., McCormac, M., Fastnacht, R.A., Ramesh, R., and Chen, L.H.
"Thousandfold change in resistivity in magnetoresistive La-Ca-Mn-O films"
Science, Vol. 264, p.413 (1994)[a]

Jin, S., McCormack, M., Tiefel, T.H., and Ramesh, R.
"Colossal magnetoresistance in La-Ca-Mn-O ferromagnetic thin films"
J. Appl. Phys., Vol. 76, p.6929 (1994)[b]

Jonker, G.H., and Santen, J.H.Van
Physica, Vol. 16, p.337 (1950)

Joosse, K., Boguslavskij, Y.M., Gerritsma, G.J., and Rogalla, H.
"Electric-field effect devices made of $YBa_2Cu_3O_{7-x}/SrTiO_3$ epitaxial multilayers"
Physica C, Vol. 224, p.179 (1994)

Ju, H.L., Kwon, C., Li, Q., Greene, R.L., and Venkatesan, T.
"Giant magnetoresistance in $La_{1-x}Sr_xMnO_z$ films near room temperature"
Appl. Phys. Lett., Vol. 65, p.2108 (1994)

Ju, H.L., Gopalakrishnan, J., Peng, J.L., Li, Q., Xiong, G.C., Venkatesan, T., and Grecne, R.L.
"Dependence of giant magnetoresistance on oxygen stoichiometry and magnetization in polycrystalline $La_{0.67}Ba_{0.33}MnO_z$"
Phys. Rev., Vol. 51, p.6143 (1995)

Kung, Pang-Jen, and Fenner, D. B.
"Growth and characterization of magnetoresistive La-Ca-Mn-O films on Si(100) and Si(111) substrates"
Appl. Phys. Lett, Vol. 69, p.427 (1996)

Lee, M.B., Kawasaki, M., Yoshimoto, M., Kumagai, M., and Koinuma, H.
"Epitaxial growth of highly crystalline and conductive nitride films by pulsed laser deposition"
Jpn. J. Appl. Phys., Vol. 33, p.6308 (1994)

Lee, M.B., Kawasaki, M., Yoshimoto, M., and Koinuma, H.
"Heteroepitaxial growth of $BaTiO_3$ films on Si by pulsed deposition"
Appl. Phys. Lett., Vol. 66, p.1331 (1995)

Lee, M.B., and Koinuma, H.
"Structural and dielectric properties of epitaxial $SrTiO_3$ films grown on Si(100) substrate with TiN buffer layer"
J. Appl. Phys., Vol. 81, p.2358 (1997)

Lewis, B., and Anderson, J.C.
"Nucleation and Growth of Thin Films"
Academic Press - New York (1978)

Liu, J.Z., Chang, I.C., Irons, S., Kalvins, P., and Shelton, R.N.
"Giant magnetoresistance at 300K in single crystals of $La_{0.65}(PbCa)_{0.35}MnO_3$"
Appl. Phys. Lett., Vol. 66, p.3218 (1995)

Maimon, T.H.
Nature, Vol. 187, p.493 (1960)

Manoharan, S.S., Vasanthacharya, N.Y., Hegde, M.S., Satyalakshmi, K.M., Prasad, V., and Subramanyam, S.V.
"Ferromagnetic $La_{0.6}Pb_{0.4}MnO_3$ thin films with giant magnetoresistance at 300K"
J. Appl. Phys., Vol. 76, p.3923 (1994)

McCormack, M., Jin, S., Tiefel, T.H., Fleming, R.M., Philips, J.M., and Ramesh, R.
"Very large magnetoresistance in perovskite-like La-Ca-Mn-O thin films"
Appl. Phys. Lett., Vol. 64, p.3045 (1994)

McGuire, T.R., and Potter, R.I.
IEEE Trans. Mag., MAG-11, p.1018 (1975)

Meng, W.J., and Eesley, G.L.
"Growth and mechanical anisotropy of TiN thin films"
Thin Solid Films, Vol. 271, pp.108-116 (1995)

Meyerand, R.G., and Haught, A.F.
Phys. Rev. Lett., Vol. 9, p.403 (1963)

Narayan, J., Tiwari, P., Chen, X., Singh, J., Chowdhury, R., and Zheleva, T.
"Epitaxial growth of TiN films on (100) silicon substrates by laser physical vapor deposition"
Appl. Phys. Lett., Vol. 61, p.1290 (1992)

Norton, G.M., Kotula, P.G., and Carter, C.B.
"Oriented aluminum nitride thin films deposited by pulsed-laser ablation"
J. Appl. Phys., Vol. 70, p.2871 (1991)

Parker, E.H.C.
"The Technology and Physics of Molecular Beam Epitaxy"
Plenum - New York (1986)

Patel, C.K.N.
"Interpretation of CO_2 optical maser experiments"
Phys. Rev. Lett., Vol. 12, p.588 (1964)

Prouteau, C., Hamet, J.F., Mercey, B., Hervieu, M., Raveau, B., Robbes, D., Coudrier, L., and Ben, G.
"Significant improvement of superconductivity of laser ablated $YBa_2Cu_3O_7$/MgO thin films: introduction of a $SrTiO_3$ buffer layer"
Physica C, Vol. 248, p.108 (1995)

Prusseit, W., et al.
"Epitaxial growth of $YBa_2Cu_3O_7$ films on GaAs with MgO buffer layers"
Appl. Phys. Lett., Vol. 61, p.1841 (1992)

Ramesh, R., et al.
"Epitaxial growth of ferroelectric bismuth titanate thin films by pulsed laser deposition"
Appl. Phys. Lett., Vol. 57, p.1505 (1990)

Rengen, A., and Narayan, J.
"Laser Ablation of Electronic Materials"
Elsevier - The Netherlands, pp363-376 (1992)

Ready, J.F.
Appl. Phys. Lett., Vol. 3, p.11 (1963)

Sanchez, R.D., and Rivas, J.
"Giant magnetoresistance in fine particle of $La_{0.67}Ca_{0.33}MnO_3$ synthesized at low temperatures"
Appl. Phys. Lett., Vol. 68, p134 (1996)

Smith, H.M., and Turner, AF.
"Vacuum deposited thin films using a Ruby laser"
Applied Optics, Vol. 4, p.147-148 (1965)

Stringfellow, G.B.
"Non hydride Group V sources for OMVPE"
Journal of Electronic Materials, Vol. 17, p.327 (1988)

Thornton, C., Tofield, B.C.,and Williams, D.E.
Sol. St. Comm., Vol. 44, p.1213 (1982)

Tiwari, P., Wu, X.D., Foltyn, S.R., Jia, Q.X., Campbell, I.H., Arendt, P.A., Muenchausen, R.E., and Peterson, D.E.
"Synthesis of epitaxial Pt on (100)Si using TiN buffer layer by pulsed laser deposition"
Appl. Phys. Lett., Vol. 65, p.2693 (1994)

Trajanovic, Z., Kwon, C., Robson, M.C., Kim, K.-C., Rajeswari, M., Ramesh, R., and Venkatesan, T.
"Growth of colossal magnetoresistance thin films on silicon"
Appl. Phys. Lett., Vol. 69, p.1005 (1996)

Treece, R.E., Dorsey, P., Rubinstein, M., Byers, J. M., Horwitz, J. S., Donovan, E., and Chrisey, D.B.
"Colossal magnetoresistance in thick $La_{0.7}Ca_{0.3}MnO_3$ films"
Mat. Res. Soc. Symp. Proc., Vol. 384, p.427-432 (1995)

Troyanchuk, I.O.
JETP, Vol. 75, p.132 (1992)

Toth, L.E.
"Transition Metal Carbides and Nitrides"
Academic - New York (1971)

Uhlir, A.
Bell Systems Tech. J., p.105 (1955)

Venables, J.A., Spiller, G.D.T., and Hanbucken, M.
Rep. Prog. Phys., Vol. 47, p.399 (1984)

Venkatesan, T., Wu, X.D., Inam, A., and Wachtman, J.B.
"Observation of two distinct components during pulsed laser deposition of high T_c superconducting films"
Appl. Phys. Lett., Vol. 52, p.1193 (1988)

Vispute, R.D., Chowdhury, R., Tiwari, P., and Narayan, J.
"Pulsed laser deposition and characterization of epitaxial Cu/TiN/Si(100) heterostructures"
Appl. Phys. Lett., Vol. 65, p.2565 (1994)

Vispute, R.D., Narayan, J., Dovidenko, K., and Jagannadham, K.
"Heteroepitaxial structures of $SrTiO_3$/TiN on Si(100) by in situ pulsed laser deposition"
J. Appl. Phys., Vol. 80, p.6720 (1996)

Wollan, E.O., and Koehler, W.C.
Phys. Rev., Vol. 100, p.545 (1955)

Wu, X. D., et al.
Mat. Res. Soc. Symp. Proc., Vol. 191, p.129 (1990)

Xiong, G.C., Li, Q., Ju, H.L., Mao, S.N., Senapati, L., Xi, X.X., and Greene, R.L.
"Giant magnetoresistance in epitaxial $Nd_{0.7}Sr_{0.3}MnO_{3-\delta}$ thin films"
Appl. Phys. Lett., Vol. 66, p.1427 (1995)

Yeh, M.H., and Liu, K.S.
"The growth behaviour of $Pb_{0.95}La_{0.05}(Zr_{0.7}Ti_{0.3})_{0.9875}O_3$ films on silicon substrates synthesized by pulsed laser deposition"
J. Appl. Phys., Vol. 77, p.5335 (1995)

Zener, C.
"Interaction between the d-shells in the Transition Metals"
Phys. Rev., Vol. 82, p.403 (1951)

Zhang, W., Boyd, W., Elliot, M, and Harkerand, W.H.
"The effects of oxygen content on the magnetoresistive behavior in La-Ca-Mn-O films grown on Si"
Appl. Phys. Lett., Vol. 69, p.3929 (1996)

Zhang, J, Chen, Z., Cui, D., Lu, H., Zhou, Y., Li, L., and Yang, G.
"Heteroepitaxial growth of a c-axis-oriented $BaTiO_3/YBa_2Cu_3O_{7-\delta}$ bilayer structure by pulsed laser ablation"
Appl. Phys. Lett., Vol. 66, p.2069 (1995)

Zheleva, T., Jagannadham, K., and Narayan, J.
"Epitaxial growth in large-lattice-mismatch systems"
J. Appl. Phys., Vol. 75, p.860 (1994)